

Deformation and Stresses generated on the Bolted Flange
Joint Assembly and the Grayloc[®] Clamp Connector at
Elevated Temperatures

by

Mustafa Mogri

A thesis submitted to the Faculty of Graduate and Postdoctoral
Affairs in partial fulfillment of the requirements for the degree of

Master of Applied Sciences

in

Mechanical Engineering

Carleton University

Ottawa, Ontario

© 2013, Mustafa Mogri

Abstract

Finite element analyses were performed to investigate the leakage and structural integrity of the bolted flange joint assembly (BFJA) and Grayloc[®] clamp connector (GCC), when each assembly was subjected to the external loads of bolt preload, internal pressure and thermal loadings. The thermal loadings were of both spatially-uniform and spatially-nonuniform temperatures on the assemblies. The initial bolt preload applied on the BFJA and the GCC was 60,000 N and 6,000 N, respectively. The internal pressure for both assemblies was 27 MPa. The BFJA was found to have satisfactory leakage and structural performance for the thermal loadings expected on the low-temperature (260°C) side of the Carleton Supercritical Water (CSCW) loop. The GCC was found to have satisfactory leakage and structural performance for the thermal loadings expected on the high-temperature (600°C) side of the CSCW loop. The leakage integrity of the GCC was found to remain intact for a temperature difference of 15°C between the inner and outer surfaces of the flange. This was not the case for a temperature difference of 100°C.

Acknowledgements

The effort in putting together this research work has been shared by many people. Foremost, I am grateful of Allah for blessing me with the intellect and knowledge to pursue this research work. I would like to thank Carleton University for providing me with the platform for undertaking this research work and providing me with the latest facilities to assist me in my research work.

I would like to thank Professor Metin I. Yaras for selecting me as a Research Assistant and making me part of his amazing research group. I am grateful to him for his thorough involvement in my work, for enhancing my knowledge every step of the way. I am proud to have worked with him and have enjoyed his mentorship immensely.

I would like to thank my parents for providing the love and financial support to make my dream of undertaking research at the Master's level in Canada a reality. I would thank my wife for unflinching support through the tough phases that is part and parcel of such challenging research work. I am grateful of all the people who have supported me, encouraged me and helped me on this journey.

Table of Contents

Abstract.....	ii
Acknowledgements	iii
Table of Contents	iv
List of Tables	vii
List of Figures.....	ix
Nomenclature	xiii
Chapter 1: Introduction	1
1.1 Motivation	1
1.2 Objective	5
1.3 Approach	5
Chapter 2: Literature Review.....	7
2.1 Bolted Flange Joint Assembly (BFJA)	7
2.2 Grayloc [®] Clamp Connector (GCC).....	24
Chapter 3: Computational Setup of Finite Element Analysis	29
3.1 Model Geometry	30
3.2 Mesh Generation	35
3.3 Computational Models of the BFJA and the GCC.....	44
3.4 Material and Mechanical Properties.....	49

3.5	Finite Element Formulation	52
3.6	Boundary Conditions.....	53
3.7	Heat Transfer Analysis for the BFJA.....	62
3.8	Heat Transfer Analysis for the GCC	67
3.9	Solution of the Finite Element Equations	71
Chapter 4: Results and Discussion—Bolted Flange Joint Assembly (BFJA)		74
4.1	Validation of the BFJA Computational Model	74
4.2	Simulation Test Matrix.....	76
4.3	Optimum Bolt Preload	77
4.4	Deformation Terminology of the BFJA.....	78
4.5	Flange Rotation	81
4.6	Leakage Integrity of the BFJA.....	86
4.7	Structural Integrity of the BFJA.....	89
Chapter 5: Results and Discussion—Grayloc® Clamp Connector (GCC)		96
5.1	Simulation Test Matrix.....	96
5.2	Deformation Behaviour of the Clamp.....	98
5.3	Structural and Leakage Integrity of the GCC.....	101
5.4	Thermal Modelling of the GCC	112
5.5	Friction Sensitivity Analysis	115
Chapter 6: Conclusions		118

References	120
Appendix A: Fluid Properties for Water and Air.....	125
Appendix B: Fundamentals of Stress Analysis	127
B.1 Spiral-Wound Gasket	127
B.2 Stress Categories	128
B.3 Structural Discontinuities	132

List of Tables

Table 3-1: The average element size and count for the BFJA and GCC models	48
Table 3-2: The type and count of elements used for the BFJA and the GCC computational models..	48
Table 3-3: Material and mechanical properties of the components of the BFJA and GCC at room temperature of 25°C (ASME, 2010c).	50
Table 3-4: Material and mechanical properties of the components of the BFJA at the design temperature of 260°C (ASME, 2010c).	50
Table 3-5: Material and mechanical properties of the components of the GCC at the design temperature of 600°C (ASME, 2010c).	51
Table 3-6: Contact-surface pairs for the BFJA and GCC computational models with their associated coefficients of friction.	57
Table 4-1: Test Matrix for the BFJA.....	76
Table 4-2: Allowable stresses for the flange and the bolt at room temperature and elevated temperature of 260°C (ASME, 2010c).	90
Table 5-1: Test-Matrix for the GCC.....	97
Table 5-2: Allowable stresses for the hub, clamp, seal-ring and the bolt at room temperature and elevated temperature of 600°C.	102
Table A-1: Property data for water at subcritical temperature of 260°C and pressure of 27 MPa (Lemmon, McLinden and Friend, 2013).	125
Table A-2: Property data for water at supercritical temperature of 430°C and pressure of 27 MPa (Lemmon <i>et al.</i>, 2013).	125
Table A-3: Property data for air at mean film temperature $[(125+15)/2]$ of 70°C under atmospheric pressure (Cengel, 2004).	125
Table A-4: Property data for air at mean film temperature $[(245+15)/2]$ of 130°C under atmospheric pressure (Cengel, 2004).	126
Table A-5: Property data for air at mean film temperature $[(885+15)/2]$ of 450°C under atmospheric pressure (Cengel, 2004).	126

Table A-6: Property data for air at Mean Film Temperature $[(845+15)/2]$ of 430°C under atmospheric pressure (Cengel, 2004).126

List of Figures

Figure 1-1: Schematic of the Carleton Supercritical Water Loop (Adapted from Balouch, 2011).....	1
Figure 1-2: Exploded view of a bolted flange joint assembly (BFJA).....	3
Figure 1-3: Exploded view of a Grayloc® clamp connector (Reproduced from Grayloc, 2010a).....	4
Figure 1-4: Sealing mechanism of a pipe clamp connector (Reproduced from Vector, 2012).....	4
Figure 2-1: Experimental loading and unloading of a spiral-wound gasket (Adapted from Mathan and Prasad, 2009).....	8
Figure 2-2: Bi-linear stress-strain curve (Reproduced from Abid <i>et al.</i> , 2008).....	10
Figure 2-3: Pressure-closure curve for a graphite-filler spiral-wound gasket (Adapted from Krishna, 2007).....	12
Figure 2-4: Schematic of an analytical model of the spiral-wound gasket (Adapted from Bouzid <i>et al.</i> , 2002).....	13
Figure 2-5: Schematic of a typical p-c curve for a gasket illustrating a loading curve-segment (0-9); and three unloading curve-segments (3-1), (12-10), (15-13) (Reproduced from AutoDesk, 2012).	14
Figure 2-6: Radial gasket contact stress distribution for several pressures (Reproduced from Krishna, 2007).....	16
Figure 2-7: Radial contact distribution a) bolting-up stage; b) pressurizing stage (Reproduced from Mathan and Prasad, 2009).	17
Figure 2-8: Influence of internal pressure on bolt preloading (Adapted from Krishna <i>et al.</i> , 2007). ..	20
Figure 2-9: Gasket separation due to high preload (Reproduced from Jenco, 2000).....	23
Figure 2-10: Compactness comparison of the GCC with the BFJA (Reproduced from Grayloc, 2012).	24
Figure 2-11: Geometry of the hub of the GCC a) true; b) T-section (Reproduced from Dekker, 2004).	26
Figure 2-12: Force distribution diagram for a pipe clamp connector (Adapted from Dekker, 2004). 26	
Figure 3-1: Geometric models of the a) BFJA and the b) GCC (Adapted from Grayloc, 2010b).....	30

Figure 3-2: Several dimensions of components of the BFJA. All dimensions are in mm. Drawing is not to scale.	31
Figure 3-3: Several dimensions of components of the GCC. All dimensions are in mm. Drawing is not to scale.....	31
Figure 3-4: Planes of geometric and loading symmetry of the a) BFJA and the; b) GCC.....	33
Figure 3-5: Simplified geometric models of the a) BFJA and; b) GCC.....	34
Figure 3-6: Mesh quality of the a) BFJA and; b) GCC.....	36
Figure 3-7: Geometric shapes of the (a) SOLID186 element and; (b) SOLID187 element (Reproduced from ANSYS Inc., 2010).	38
Figure 3-8: Interface element INTER194 (Reproduced from ANSYS Inc., 2010).....	39
Figure 3-9: CONTA174 and TARGE170 elements overlaid on the contact body. (Reproduced from ANSYS, 2010).....	40
Figure 3-10: Schematic of PRETS179 element (Reproduced from ANSYS, 2010).....	42
Figure 3-11: Location of cutting surfaces and the nodes of PRETS179 on the bolt (ANSYS Inc., 2010).	43
Figure 3-12: Final mesh of the BFJA.....	45
Figure 3-13: Final mesh of the GCC.....	46
Figure 3-14: The pressure-closure curve for the semi-metallic gasket used on the BFJA (ANSYS Inc., 2010).....	52
Figure 3-15: Fixed support applied on the computational models of the a) BFJA; b) GCC.	54
Figure 3-16: Symmetry condition applied on the section-faces of the computational model of the a) BFJA; b) GCC.....	54
Figure 3-17: Contact-surface pairs of the BFJA computational model: a) bolt/flange; b) gasket/flange; c) end-cap extension/flange.....	55
Figure 3-18: Contact-surface pairs of the GCC computational model: a) hub/clamp; b) clamp/bolt; and; c) flange/end-cap extension.....	56
Figure 3-19: Bolt preloading.	58

Figure 3-20: Internal pressure applied on the inside surfaces of the a) BFJA and b) GCC. Only one-half of the inside surfaces are shown for effective illustration.	59
Figure 3-21: Constraints of symmetry bolt preload and internal pressure imposed on the a) BFJA; b) GCC.	60
Figure 3-22: Simplified BFJA geometry for heat transfer analysis a) superimposed on the geometric model; b) shown with the thermal resistance network.	63
Figure 3-23: Simplified GCC geometry for heat transfer analysis a) superimposed on the geometric model; b) shown with the thermal resistance network.	68
Figure 4-1: Stress distribution in the gasket.	75
Figure 4-2: Deformation of the flange-ring a) rotational axial displacement, <i>Drot</i> ; b) pure axial displacement, <i>Daxi</i> . The amount of deformation is exaggerated for illustration.	79
Figure 4-3: Computed deformation of the flange under the combined effects of initial bolt preload, internal pressure and spatially-nonuniform elevated temperature. The amount of expansion has been amplified by 500 times for the purpose of effective illustration.	80
Figure 4-4: Circumferential deformation of the “unfolded” flange-ring of the BFJA. The amount of deformation is exaggerated for effective illustration.	81
Figure 4-5: High-stress and low-stress radial planes on the gasket.	82
Figure 4-6: Radial flange rotation at the low-stress gasket plane for Cases 1 to 4. Note: The y-axis ranges for <i>Drot</i> and <i>Daxi</i> are the not the same to allow for effective visualization of the trends in these two parameters.	84
Figure 4-7: Gasket stresses across the radial-width of the gasket.	88
Figure 4-8: Von Mises stresses for the flange a) Case 2—room temperature; b) Case 3—uniform elevated temperature; c) Case 4—temperature gradients across the BFJA at elevated temperature.	91
Figure 4-9: a) Bolt section stress; b) bolt periphery stress for spatially-nonuniform elevated temperatures across the BFJA, as per Case 4.	94

Figure 5-1: Schematic of the clamp and the bolt in the a) non-deformed position; b) deformed position under external loads at room temperature. The amount of deformation is exaggerated for clarity.	98
Figure 5-2: Clamp rotation when the GCC is subjected to a) Case 2--uniform elevated temperature; b) Case 3—temperature gradients across the GCC at elevated temperature. The amount of expansion has been amplified by 40 times for the purpose of clarity.....	100
Figure 5-3: Von Mises stresses for the hub a) Case 1—room temperature; b) Case 2—uniform elevated temperature; and c) Case 3—temperature gradients across the GCC at elevated temperature.	103
Figure 5-4: Von Mises stresses for the clamp a) Case 1—room temperature; b) Case 2—uniform elevated temperature; and c) Case 3—temperature gradients across the GCC at elevated temperature.	106
Figure 5-5: Von Mises stresses for the seal-ring a) Case 1—room temperature; b) Case 2—uniform elevated temperature; and c) Case 3—temperature gradients across the GCC at elevated temperature.	109
Figure 5-6: Deformation of the seal-ring cross-section for a) Case 1-room temperature; b) Case 2-spatially-uniform elevated temperature. The amount of deformation has been exaggerated 1000 times for clarity.	111
Figure 5-7: Von Mises stresses for the hub for temperature gradients a) Case 3—temperature gradients across the GCC at elevated temperature; b) Case 4—higher temperature gradients.	113
Figure 5-8: Von Mises stresses generated on the a) contact surface; b) surface adjacent to the contact surface.....	116
Figure B-1: Spiral-wound gasket a) full view; b) section view (Reproduced from ISG, 2012).....	128
Figure B-2: Load-controlled vs. Strain-controlled behaviour (Reproduced from Becht, 2002).....	130
Figure B-3: Stress-strain plot illustrating elastic shakedown behaviour (Reproduced from Becht, 2002).....	131
Figure B-4: Structural discontinuities a) local; b) gross (Reproduced from Wood, 2012).	133

Nomenclature

A_c	Cross-sectional area of the flange/hub (m^2)
A_o	Original cross-sectional area of test-specimen (m^2)
A_s	Exposed surface area of test-specimen (m^2)
c_p	Isobaric specific heat (J/kgK)
$[D]$	Stress-strain matrix (MPa)
D_{axi}	Pure axial displacement (mm)
D_{rot}	Rotational axial displacement (mm)
E	Young's Modulus of Elasticity (MPa)
e	Energy error vector (mJ)
f	Secondary stress factor
F	Residual bolt preload per bolt (N)
$F_{a(hub)}$	Axial force exerted by clamp on hub (N)
$F_{a(seal)}$	Axial force exerted by hub on seal-ring (N)
$[F_E]$	Force matrix (N)
F_p	Initial bolt preload per bolt (N)
$F_{r(hub)}$	Radial force exerted by clamp on hub (N)

$F_{r(seal)}$	Radial force exerted by hub on seal-ring (N)
F_u	Uni-axial force applied on test-specimen (tension or compression) (N)
g	Gravity (m/s^2)
h	Convective heat transfer coefficient (W/m^2K)
$[K_E]$	Element stiffness matrix (N/m)
k	Thermal conductivity (W/mK)
L_{ch}	Characteristic length to evaluate Reynolds number (m)
L_o	Original length of test-specimen (m)
m	Gasket maintenance factor
\dot{m}	Mass flow rate (kg/s)
Nu	Nusselt number
P	Internal pressure (MPa)
Pr	Prandtl number
Q	Heat energy (J)
r	Radial length along the width of the component (m); $0 \leq r \leq R_f, 0 \leq r \leq R_g$
$r_{c,i}$	Characteristic radii of the GCC (m); $i = 1,2,3 \dots$

$r_{f,i}$	Characteristic radii of the BFJA (m); $i = 1,2,3 \dots$
R_f	Radial width of flange-ring (m)
$r_{g,i}$	Radii of gasket of the BFJA (m); $i = 1,2$
R_g	Radial width of gasket (mm)
R_{cond}	Conductive thermal resistance (K/W)
R_{conv}	Convective thermal resistance (K/W)
Ra	Rayleigh number
Re	Reynolds number
S_Y	Yield stress of a component (MPa)
S_C	Allowable stress of a component at room temperature (MPa)
S_H	Allowable stress of a component at design temperature (MPa)
T	Temperature ($^{\circ}\text{C}$ or K)
$T_{f,i}$	Surface temperatures on the BFJA ($^{\circ}\text{C}$ or K); $i = 1,2,3 \dots$
$[u]$	Displacement field matrix (m)
vol	Volume of a finite element (m^3)
V	Mean velocity of the fluid (m/s)

Superscripts

<i>a</i>	Average stress error
<i>i</i>	i^{th} element of the mesh
<i>nd</i>	Nodal force matrix
<i>pr</i>	Pressure force matrix
<i>th</i>	Thermal force matrix

Subscripts

<i>a</i>	Ambient air
<i>c, i</i>	Associated with the GCC; $i = 1, 2, 3 \dots$
<i>e</i>	Exit
<i>exp</i>	Experimental
<i>f, i</i>	Associated with the BFJA; $i = 1, 2, 3 \dots$
<i>g, o</i>	Operating stresses on the gasket
<i>i</i>	Inlet
<i>loss</i>	Loss of energy from the BFJA or the GCC to the ambient surroundings
<i>MAX</i>	Maximum stress at any location
<i>mic</i>	Micromechanical

n	n^{th} node of a particular finite element
p, a	Allowable primary stress limit for a component
tot	Total
s, a	Allowable secondary stress limit for a component
w	Working fluid
VM	Von Mises stress

Greek Letters

α	Thermal diffusivity (m^2/s)
β	Coefficient of volume expansion ($1/\text{K}$)
ρ	Density of the fluid (kg/m^3)
δ_L	Change in length of test-specimen (m)
ε	Strain (m/m)
σ	Stress (MPa)
$\Delta\sigma$	Stress error vector (MPa)
μ	Dynamic viscosity of the fluid (kg/ms)
ν	Kinematic viscosity of the fluid (m^2/s)

Acronyms

BFJA	Bolted Flange Joint Assembly
CSCW	Carleton Supercritical Water
GCC	Grayloc [®] Clamp Connector
LCMT	Load Compression Mechanical Test

Chapter 1: Introduction

1.1 Motivation

Convection heat transfer in supercritical water is a field of research for the development of Supercritical Water-Cooled Reactors (SCWR) as part of the Generation IV International Forum (OECD, 2010). Carleton University is participating in such research and is developing a Carleton Supercritical Water (CSCW) loop experimental facility on campus (Figure 1-1). The CSCW loop is a high-pressure (27 MPa) and high-temperature

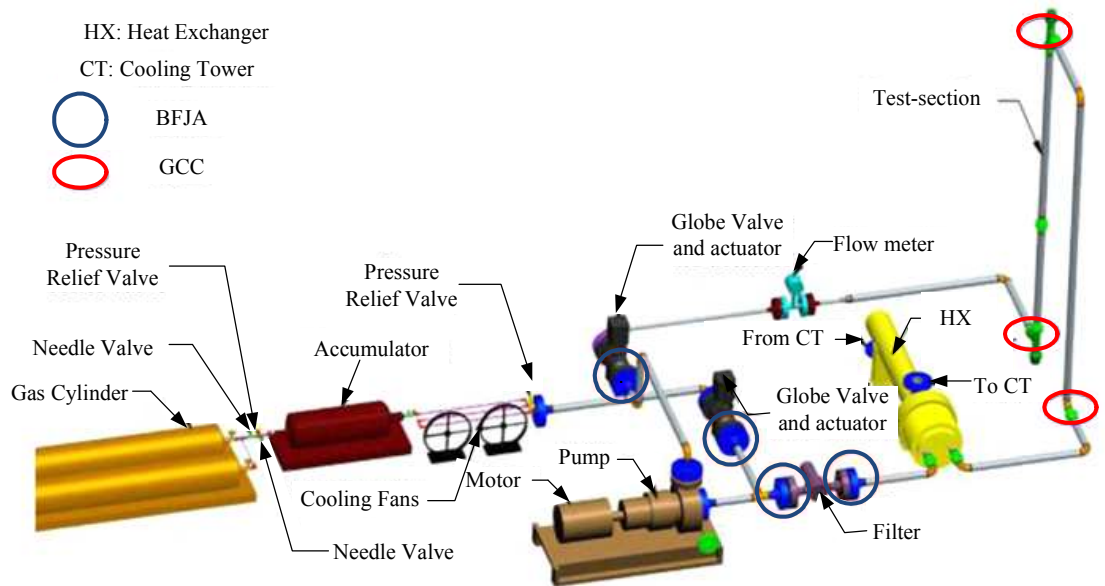


Figure 1-1: Schematic of the Carleton Supercritical Water Loop (Adapted from Balouch, 2011).

(260-600°C) piping network made up of a pump, heat exchanger, globe valves, filter, accumulator, flow meter and a modular test section. These components are joined using bolted flange joint assemblies (BFJA) and Grayloc[®] clamp connectors (GCC), as shown in Figure 1-1. The modular test section on the CSCW loop (Figure 1-1) is electrically

heated to produce a bulk-fluid temperature of 600°C at 27 MPa to achieve the desired supercritical thermodynamic state for water. This hot working fluid discharging from the test section is then cooled down inside the heat exchanger to a subcritical bulk-fluid temperature of 260°C, and after going through the pump is returned to the inlet of the test section. The BFJA is installed on the inlet side of the test section, while the GCC is installed at the exit of the test section. While it is practical to employ a BFJA on the inlet side of the test section, a GCC is employed at the exit of the test section to circumvent the use of a large BFJA elevated from the floor on the CSCW loop (Balouch, 2011).

Design requirements for a BFJA are regulated by the design rules stated in ASME (American Society of Mechanical Engineers) Section VIII-1 (ASME, 2010a). However, the design rules are guidelines outlining the minimum requirements; adherence to these rules does not guarantee a leak-proof design (Krishna, Shunmugam and Prasad, 2007). The ASME design rules are based on material properties at a spatially-uniform temperature. They do not account for the temperature gradients that will develop across the BFJA and the GCC during operation on the CSCW loop due to the difference in the temperatures of the working fluid and the ambient air (Brown, Derenne and Bouzid, 2001). Temperature gradients generate stresses in the BFJA and the GCC and may cause leakage and/or structural failure. Furthermore, the design and selection of the GCC is restricted to the design temperature and pressure expected on the piping loop. The design rules do not accommodate the thermal influence of external heat sources that may be part of the rest of the piping loop (e.g. electrical heating of the test section). The present study investigates if both the BFJA and the GCC can withstand the effects of thermal loadings

and perform their intended function for the temperatures (including spatial nonuniformities) and pressure expected on the CSCW loop.

The mechanisms of operation of the BFJA and the GCC are briefly explained here. Figure 1-2 illustrates that a BFJA suitable for use on the CSCW loop is made up of two flanges, four bolts, and a semi-metallic gasket. The flanges are held together with the bolts and the gasket provides a conformable medium between the flanges to seal the

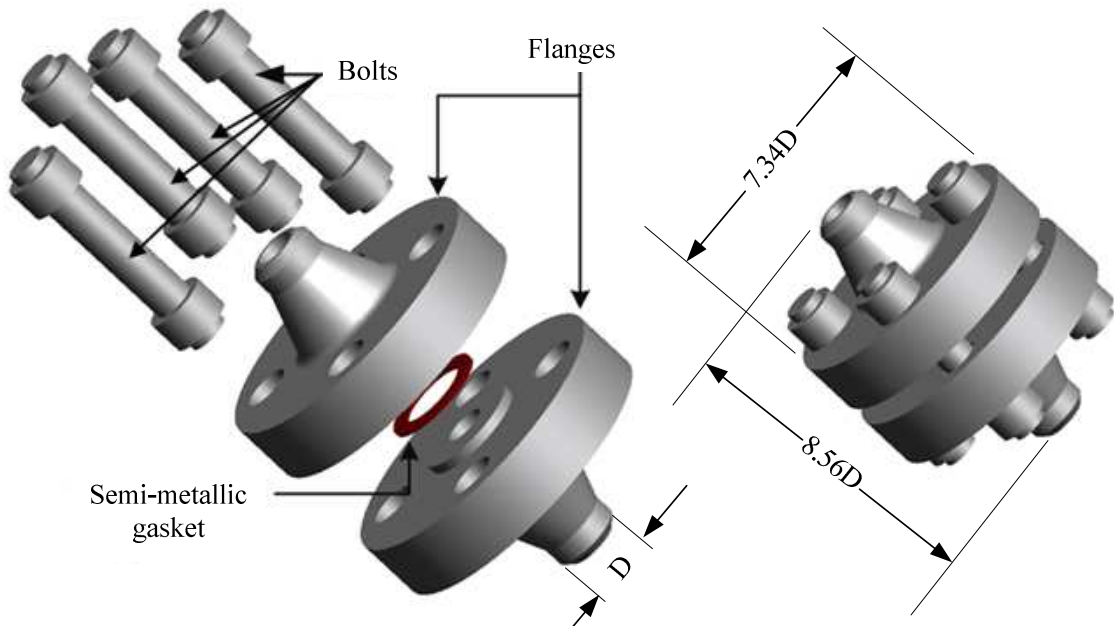


Figure 1-2: Exploded view of a bolted flange joint assembly (BFJA).

assembly. A BFJA provides structural integrity and leak-proof service, and of the two functions, providing leak-proof service has proven to be more difficult (Jenco and Hunt, 2000). The gasket plays the most important role in assuring leak-proof operation of a BFJA. The GCC is made up of two clamps, two hubs, four bolts and a metal seal-ring, as shown in Figure 1-3. The seal-ring provides an effective seal by conforming against the hub-recesses as the hubs are pressed together by the force of the bolted clamps (Grayloc, 2010a).

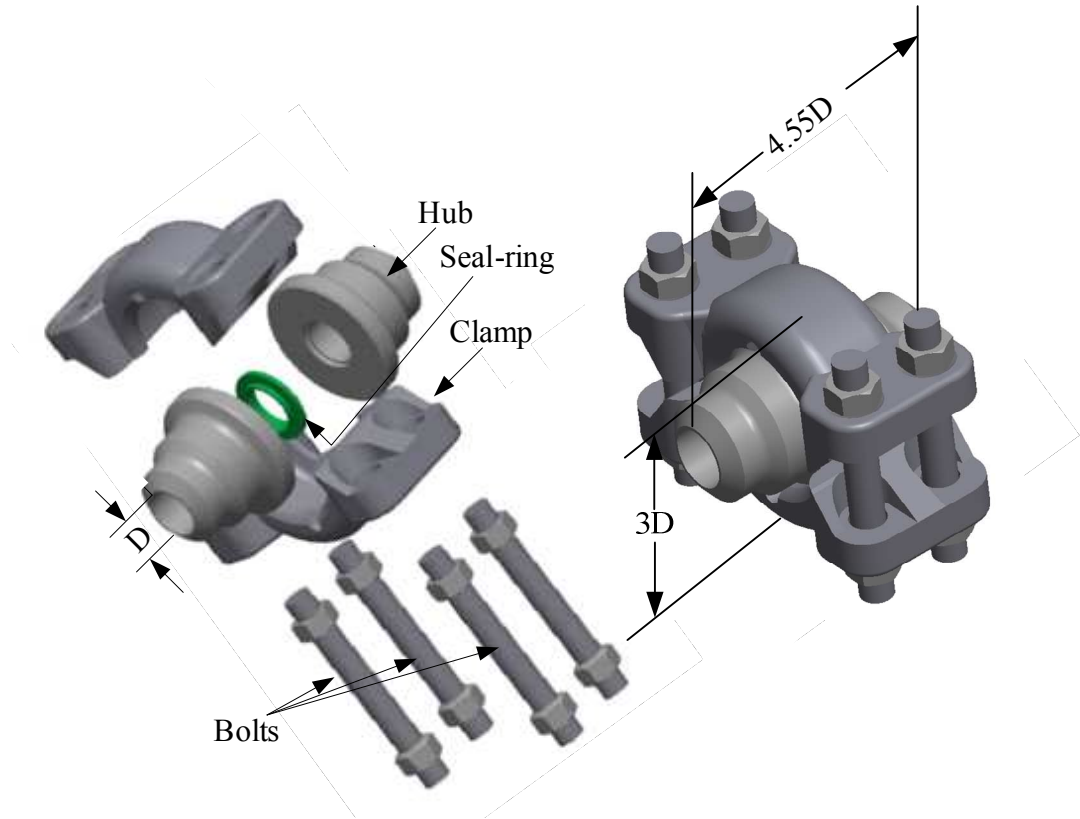


Figure 1-3: Exploded view of a Grayloc[®] clamp connector (Reproduced from Grayloc, 2010a).

The seal-ring is further energized by the internal pressure which reinforces the sealing. This sealing mechanism is illustrated for a similar pipe clamp connector in Figure 1-4. Since the hubs and the seal-ring are cylindrical, the circumferential orientation of the clamps can be chosen to suit the installation.

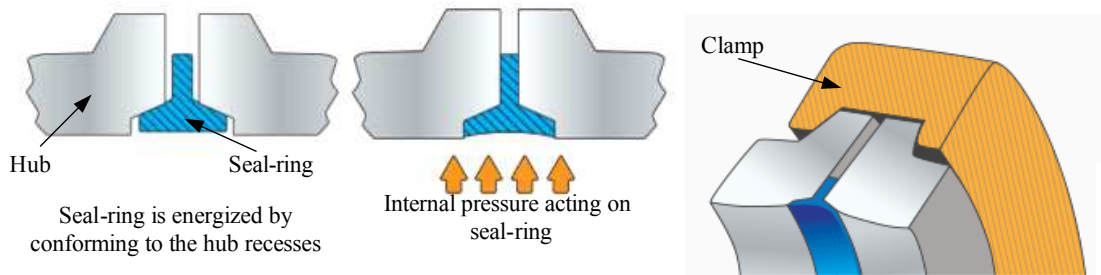


Figure 1-4: Sealing mechanism of a pipe clamp connector (Reproduced from Vector, 2012).

1.2 Objective

The present study deals with the leakage and structural integrity of the BFJA. Specifically, the investigation focuses on the stresses generated in the gasket and the flanges, establishes the bolts loadings expected during operation, and provides recommendations for the optimum bolt loading for the design conditions of the CSCW loop.

The present study deals with the leakage and structural integrity of the GCC under loadings expected during operation. Specifically, the stresses in the seal-ring are used to determine leakage integrity while the stresses generated in the remaining components of the GCC are used to identify the structural performance of the assembly. Moreover, the effect of lubrication on the surface interaction between the hub and the clamp is investigated to shed further light on the load transfer paths between the components of the GCC.

1.3 Approach

A finite element analysis was performed to determine stresses for the components of the BFJA for a fluid pressure of 27 MPa and bulk-fluid temperature of 260°C. The external loads were applied in three successive loading steps: the bolt loading was applied in the first load step, the internal pressure in the second load step and the thermal loadings in the third load step. The stresses in the gasket were evaluated after each loading and were investigated in the context of the maximum operating gasket stresses allowed for the given dimensions of the BFJA and operating conditions of the CSCW loop. The von

Mises stress distributions for the flanges and bolts on the BFJA were investigated in the context of the allowable primary and secondary stress limits, given by the ASME design code (ASME, 2010a), to establish the structural integrity of the BFJA. This multi-step approach enabled investigation of the incremental effects of the external loadings on the performance of the BFJA.

A finite element analysis was performed to determine the stresses in the GCC for a fluid pressure of 27 MPa and bulk-fluid temperature of 600°C. Similar to the BFJA analysis, the external loads namely bolt preload, internal pressure and thermal loads were applied in successive loading steps. The von Mises stress distributions in the components of the GCC were investigated in the context of the allowable primary and secondary stress limits, given by the ASME design code (ASME, 2010a), to establish the structural integrity of the GCC. This multi-step approach enabled investigation of the incremental effects of the external loadings on the performance of the GCC.

For both the BFJA and GCC analyses, initial bolt preloads were evaluated using ASME design rules (ASME, 2010b, 2010d). The initial bolt preload for the BFJA was modified based on the hard-joint condition to evaluate the optimum bolt preloading.

Chapter 2: Literature Review

This chapter describes how a bolted flange joint assembly (BFJA) and a Grayloc[®] clamp connector (GCC) have been modelled in the published literature. Section 2.1 covers literature related to material modelling and external loadings on the BFJA. Section 2.2 covers literature related to material modelling and external loadings on the GCC. For those readers who do not have a background in stress analysis, the fundamental theory of stress analysis related to the present study is presented in Appendix B.

2.1 Bolted Flange Joint Assembly (BFJA)

Analytical models have been developed to capture the deformation response of a gasket (e.g. Sawa *et al.*, 1991; Bouzid and Derenne, 2002). Sawa *et al.* (1991) modelled a metallic gasket as an elastic body. However, this approach cannot be used for semi-metallic gaskets since it does not account for the non-linear behaviour of such gaskets (Krishna *et al.*, 2007). Bouzid and Derenne (2002) modelled a semi-metallic gasket by developing a stress vs. deflection model, based on a pressure closure (p-c) curve that was developed empirically. Figure 2-1 illustrates two p-c curves: one experimental p-c curve that has a loading curve-segment 0-B_{exp} and an unloading curve-segment B_{exp}-C_{exp}; and one micromechanically-modeled computational p-c curve that has a loading curve-segment 0-B_{mic} and an unloading curve-segment B_{mic}-C_{mic}. Micromechanical modelling of the gasket refers to individually modelling each metal strip and filler layer that constitute a spiral-wound gasket. Bouzid and Derenne (2002) simplified the unloading curve-segment in their stress vs. deflection model to be completely linear by neglecting

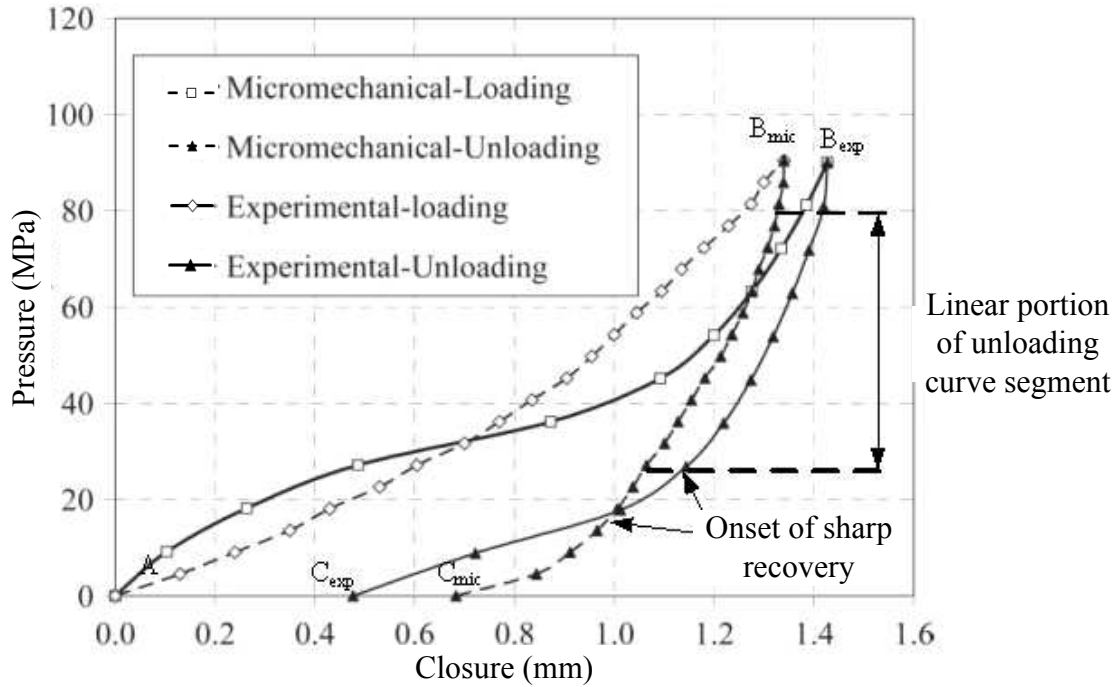


Figure 2-1: Experimental loading and unloading of a spiral-wound gasket (Adapted from Mathan and Prasad, 2009).

the sharp recovery at the end of the unloading curve-segment. Figure 2-1 illustrates that while the initial unloading of the gasket can be assumed to be linear; the sharp recovery of the gasket at the end of the unloading cycle is highly non-linear and cannot be linearized using a single function.

On a BFJA, the gasket deforms when compressed due to an initial bolt preload to provide the sealing between the raised-faces of the mating flanges. Bolt preload, internal pressure, and spatially-nonuniform thermal loads are all external loadings that act on the BFJA. Bolt preloading provides the clamping force for the BFJA; internal pressure causes decompression of the gasket; and temperature gradients generate thermal strain (Brown *et al.*, 2001a). Each of these external loads generates stresses in the components of the

BFJA. Detailed review of each external load on each component of the BFJA, presented in the following sections, lends insight into the performance of the BFJA.

Before investigating the influence of the external loadings, it is important to determine how the material for each component of the BFJA is modelled. This is presented next.

2.1.1 Material Modelling of the Semi-Metallic Gasket

The gasket material has a mixed behaviour due to its composition; an elastic behaviour due to the metal material, and a plastic behaviour due to the filler or layer material. The following sections describe practices used to model gasket materials.

2.1.1.1 Elastic and Elastic-Plastic Model

An elastic model representation of the gasket may be valid only if the stresses generated are elastic on loading and they are relieved at removal of the load (Jenco and Hunt, 2000). Sawa *et al.* (1991) modelled a raised-face metallic gasket as an elastic hollow cylinder. However, this elastic model is unsuitable for a BFJA employing a semi-metallic gasket because the external loads typically applied on the BFJA cause plastic deformation of the filler material.

Abid *et al.* (2008) used a bilinear material model to study the effect of internal pressure and thermal loadings on a spiral-wound gasket. They assumed the unloading behaviour to be linear, as shown in Figure 2-2. However, a sharp elastic recovery zone exists near the end of the unloading curve as shown in Figure 2-1, and this information is lost in linearizing the unloading curve.

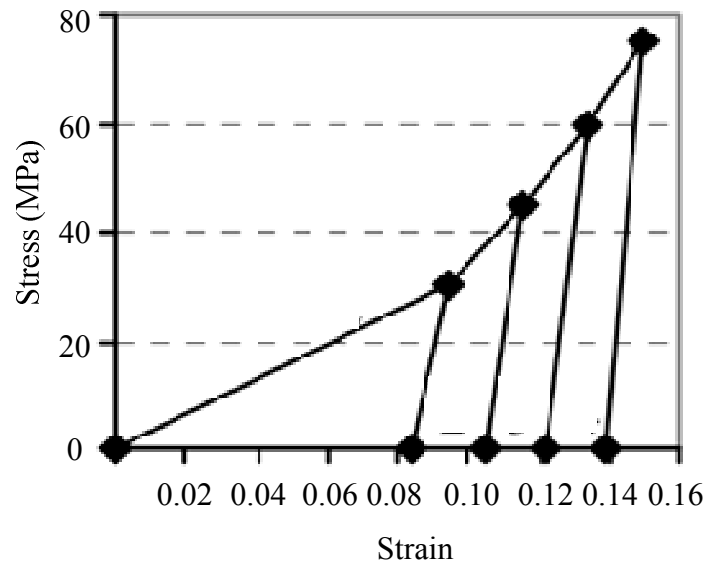


Figure 2-2: Bi-linear stress-strain curve (Reproduced from Abid *et al.*, 2008).

2.1.1.2 Hyperelastic Model

Mathan and Prasad (2009) modelled the semi-metallic gasket at the micromechanical level by assuming the semi-metallic gasket as a multi-layer composite. They modelled each metal strip as an elastic-plastic material, and each layer of polytetrafluoroethane (PTFE) filler to be a hyperelastic material. A hyperelastic model for the filler material depicts the non-linear elastic deformation by suitably relating the strain-energy density of the filler material to its deformation gradient. The micromechanical modelling of the semi-metallic gasket is cumbersome since a typical gasket has up to 20 layers of filler material squeezed between metal strips. The p-c curve (explained in Section 2.1.1.4) simplifies the micromechanical approach by representing the effective behaviour of the gasket as a single body.

The response of this micromechanical model to internal pressure is illustrated in Figure 2-1. The micromechanical model exhibits less strain under loading and a delayed strain

recovery during unloading when compared to experimental results. Mathan and Prasad (2009) attribute the discrepancies between the micromechanical model and the experimental p-c curve to the presence of voids in the actual gasket material. By assuming perfect contact between the metal and the filler in the micromechanical model, the voids present in an actual semi-metallic gasket are ignored. These discrepancies can be critical since the micromechanical model indicates higher compression of the gasket at a lesser pressure when in reality there may be separation between the gasket and the flange, as indicated by experiment.

2.1.1.3 Non-Linear Model

Gasket behaviour is complex due to the material and geometric non-linear behaviour, and the best approach is to use a general non-linear deformation model that has a non-linear curve-profile for the elastic and plastic deformations of the gasket. For this purpose, the pressure-closure (p-c) curve, as shown in Figure 2-3, is developed empirically, by conducting a load compression mechanical test (LCMT) on a particular gasket (Krishna et al., 2007). The constitutive equation that represents the mechanical behaviour of a material is given by:

$$\sigma = C(\varepsilon) \quad (3-1)$$

where $C(\varepsilon)$ is a function obtained from experimental analyses. However, a difficulty arises in developing a specific constitutive relationship between stress and strain for a semi-metallic gasket since the deformation varies between test-specimens of the same type of gasket (Jenco and Hunt, 2000). This variation is random due to the random position of voids between the metal mandrel and the filler material.

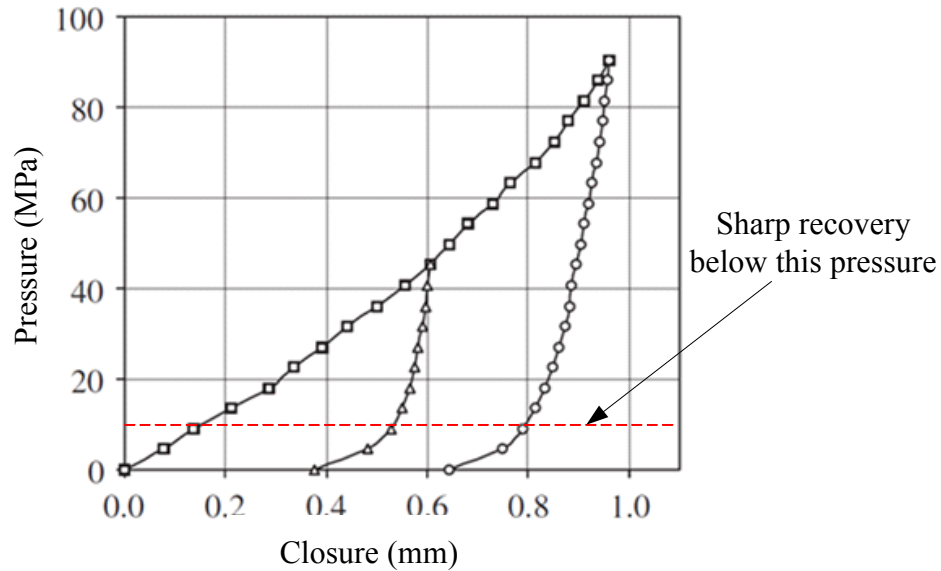


Figure 2-3: Pressure-closure curve for a graphite-filler spiral-wound gasket (Adapted from Krishna, 2007).

Bouzid and Derenne (2002) and Krishna *et al.* (2007) simplified the non-linear model by assuming that the unloading curve-segments were identical, independent of the unloading position on the loading curve-segment. Krishna *et al.* (2007) assumed that the unloading of the gasket was linear until reaching a certain pressure, as marked in Figure 2-3, beyond which the gasket sharply recovered its strain energy. Bouzid and Derenne (2002) assumed that the gasket operated in the range of the solid line shown in Figure 2-4; they contended that the gasket never fully unloaded in operation and therefore ignoring the end of the unloading curve was reasonable. However, gasket separation may occur at certain locations due to irregularities in the external loading; and this separation can only be captured by using the complete unloading curve. The analytical model of Bouzid and Derenne (2002) also assumes that the deflection of the gasket varies linearly with the radius. Furthermore, the Poisson effect is neglected meaning that the gasket area is assumed to remain constant under loading. The p-c curve developed by Krishna *et al.*

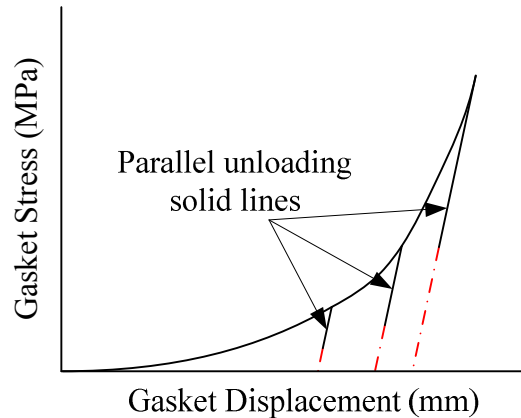


Figure 2-4: Schematic of an analytical model of the spiral-wound gasket (Adapted from Bouzid *et al.*, 2002).

(2007) accounts for the complete unloading behaviour of the semi-metallic gasket and therefore is preferred for the present work over the simplified model of Bouzid and Derenne (2002). The p-c curve is explained next.

2.1.1.4 Pressure-Closure Curve for Semi-Metallic Gasket

Schematic of a typical p-c curve, as shown in Figure 2-5, is developed by compressively loading a disc-shaped gasket specimen and measuring the deformation. The compressive loading is plotted in terms of pressure against the deformation/closure that is caused by the compressive loading. The closure is the differential deformation of the top and bottom surfaces of the specimen.

The p-c curve is developed for a particular gasket material and is specific to that gasket. For several specimens of a particular configuration of the gasket, there may be a compressibility variation under identical loading (Jenco and Hunt, 2000). This variation may occur either due to random voids between metal and filler material during manufacturing or due to a modification to the gasket surface while storing and

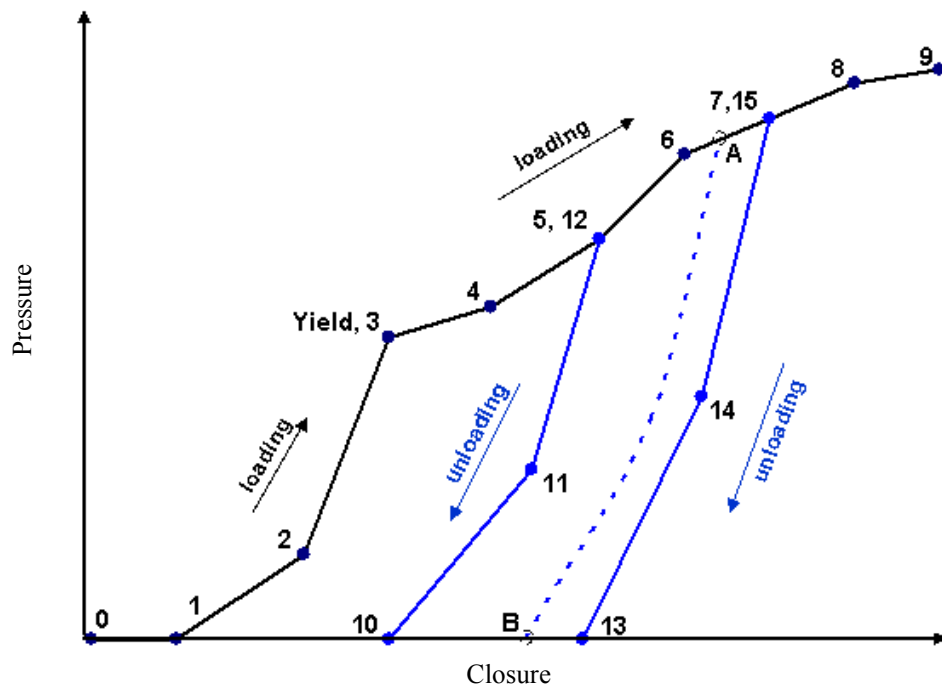


Figure 2-5: Schematic of a typical p-c curve for a gasket illustrating a loading curve-segment (0-9); and three unloading curve-segments (3-1), (12-10), (15-13) (Reproduced from AutoDesk, 2012).

transporting the gaskets. While the latter factor can be minimized by better managing practices, the former cause of variation can be minimized only by plotting the mean p-c curve developed by LCMT on several test-specimens of a particular type of gasket from the same manufacturer.

In Figure 2-5, the gasket/specimen undergoes elastic deformation for lower values of pressure (0 to 3). If the pressure on the gasket is increased, the gasket starts to permanently deform with strain hardening, requiring progressively greater pressure to cause deformation of the gasket. The gasket cannot be indefinitely loaded as it gets crushed, i.e. it loses all of its elastic ability. Depressurizing/unloading the gasket at point 5 after yielding returns the curve to point 10, illustrating permanent deformation of the gasket. The unloading curve-segment generally depends on the point of unloading and

the rate of unloading. However, for most practical purposes two assumptions are made for the unloading curve-segments: they do not depend on the position on the unloading curve-segment (3-9) and they share an identical curve-profile (Bouزيد and Derenne, 2002; Krishna *et al.*, 2007).

2.1.2 External Loading on Gaskets

Researchers have analysed the external loads applied to gaskets in different ways. Bouزيد and Derenne (2002), Krishna *et al.* (2007) and Mathan and Prasad (2009) considered the influence of internal pressure and initial bolt preload applied on the gasket on a BFJA at room temperature. Bouزيد and Nechache (2005) extended this pressure analysis to study the influence of high spatially-uniform thermal loadings. Brown *et al.* (2002) and (2005) investigated the performance of the BFJA for spatially-nonuniform thermal loadings and thermal transients, respectively. Abid *et al.* (2008) performed a study of the BFJA under internal pressure and spatially-nonuniform thermal loadings on the BFJA. Each of these investigations is reviewed below.

2.1.2.1 Internal Pressure

The internal pressure counters the compressive clamping force on the gasket and therefore decreases the compressive stresses on the gasket, as illustrated by Figure 2-6 (Krishna *et al.*, 2007). An initial bolt preload, F_p , of 30,000 N is applied on each of the six bolts on the BFJA, with internal pressures of 0, 5 and 10 MPa, represented by lines 1, 2 and 3, respectively, applied on the BFJA. Similarly, internal pressures of 0, 5 and 10 MPa with an initial bolt preload, F_p , of 35,000 N on each of the six bolts on the BFJA are

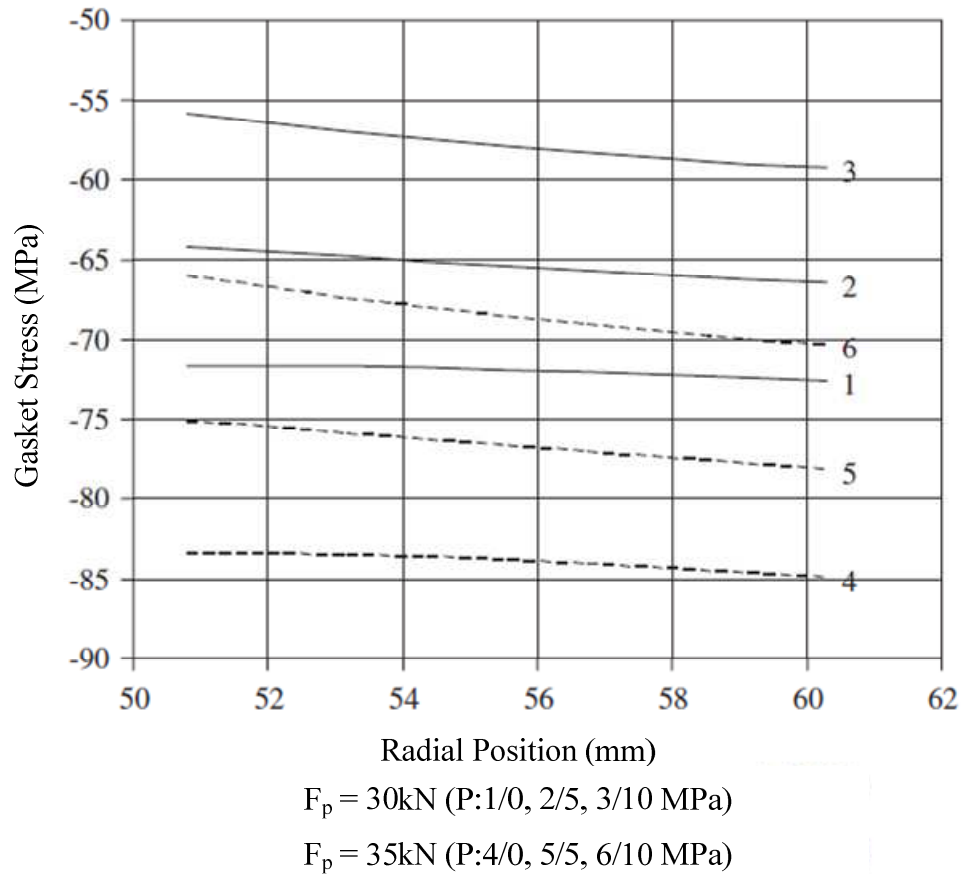


Figure 2-6: Radial gasket contact stress distribution for several pressures (Reproduced from Krishna, 2007).

represented by dashed lines 4, 5 and 6, respectively. Line 3, representing an internal pressure of 10 MPa has lower values of gasket stresses than Line 1, representing zero internal pressure. An increased initial bolt preload generates higher gasket stresses. Furthermore, the gasket stresses are higher on the outer part of the gasket, which is expected because of the increasing proximity to the bolts (Do, 2011). This effect is more pronounced for higher values of initial bolt preload, as indicated in Figure 2-6 by greater slopes of the lines plotted for higher bolt preload.

Mathan and Prasad (2009) also studied the gasket stresses across the radial-width of the gasket, as illustrated in Figure 2-7. An initial bolt preload, ranging from 25 kN to 40 kN was applied on the gasket in the bolting-up stage. A pressure of 10 MPa was then applied on the gasket in the bolting-up stage. A pressure of 10 MPa was then applied on the gasket, reducing the gasket stresses, as illustrated in Figure 2-7b by a positive-translation of the y-axis scale.

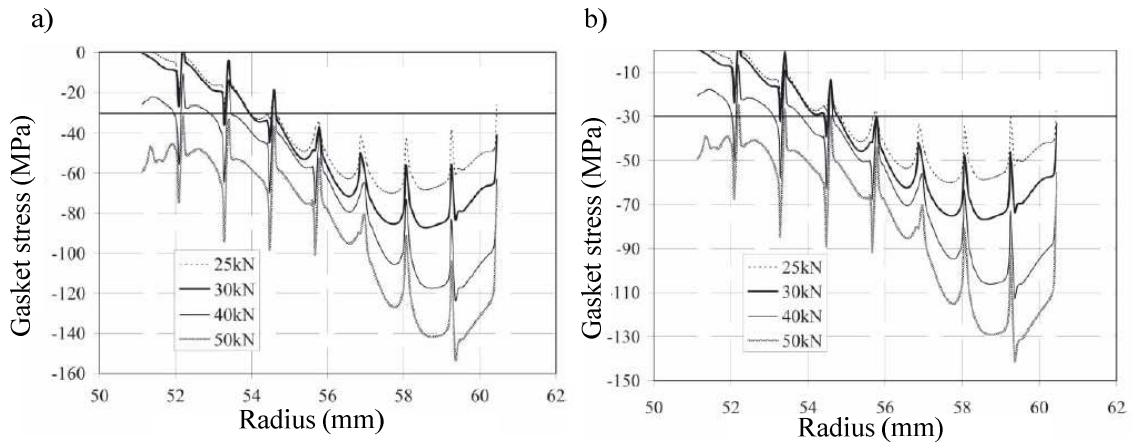


Figure 2-7: Radial contact distribution a) bolting-up stage; b) pressurizing stage (Reproduced from Mathan and Prasad, 2009).

2.1.2.2 Thermal Loading

Brown *et al.* (2001) used a decoupled thermal/mechanical load analysis to model the behaviour of the gasket. They performed a thermal analysis of the BFJA without the gasket, where the temperature of the working fluid was taken as 300°C and the temperature of the ambient air was taken as 0°C, and obtained the temperature field including values at the mating surfaces of the flange and the gasket. They then performed a static mechanical-load analysis incorporating the temperatures obtained from the thermal analysis as equivalent deflections. However, this approach does not capture the strain generated within the gasket due to the temperature gradients. The premise for a

decoupled analysis was the limitation of the interface element used to model gaskets with commercial finite element software; the interface element could not be used to model thermal loads. Furthermore, they neglected the temperature gradients within the individual components of the BFJA assuming them to be small compared to the gross thermal deformations for the BFJA as an assembly. However, the temperature gradients within the flange, for instance, will contribute to the surface interaction of the flange with the gasket. Therefore, neglecting these temperature gradients does not allow proper modelling of the sealing performance of the BFJA.

Abid *et al.* (2008) applied the external loads of bolt preload, internal pressure and temperature gradients to a two-dimensional computational model of a BFJA for a working fluid temperature range of 100-400°C and an ambient air temperature of 20°C. They noted that the change in the stresses of the spiral-wound gasket was very small compared to a metal gasket and attributed this lack of variation to the limitations of a two-dimensional model to account for the change in temperature in the circumferential direction. Furthermore, a two-dimensional model cannot be used to model the variation of the gasket stresses in the radial and circumferential directions.

2.1.2.3 Bolt Preload

The effect of bolt preloading on the gasket requires an understanding of the effect of the initial bolt preload on the flange. Therefore, the discussion for the gasket is deferred to Section 2.1.7.

2.1.3 Material Modelling of the Flange

Although the flange is the largest physical part of the BFJA, it is considerably less difficult to model than other parts of the assembly. For high-pressure and high-temperature use of the BFJA, the appropriate flange type is a weld-neck flange with raised-faces (Balouch, 2011; Krishna *et al.*, 2007; Nayyar, 2000;). The raised-faces of the flange reduce the contact area with the gasket to lower the initial bolt preload required to seat the gasket. Abid *et al.* (2008), Hwang (1994), Krishna *et al.* (2007), and Mathan and Prasad (2009) modelled the flanges as an elastic-plastic and isotropic material.

2.1.4 External Loading on the Flange

2.1.4.1 Internal Pressure

The flange behaves like an elastic-plastic body for the range of pressures expected on the CSCW loop. Mathan and Prasad (2009) evaluated the longitudinal stresses generated for the bolting-up and pressurized cases. Stresses for the pressurized case are higher than the bolting-up stage as would be expected.

2.1.4.2 Thermal Loading

The thermal loadings on the flange are applied in the form of inner and outer surface temperatures on the BFJA. Abid *et al.* (2008) modelled steady-state temperatures ranging from 100-400°C on the inner surfaces of the BFJA, while the outer surfaces were subjected to a temperature of 20°C. The stresses in the flange were reduced with increase

in inner surface temperature. Abid *et al.* (2008) attribute this reduction to the relaxation of the flange with increasing temperature.

2.1.4.3 Bolt Preload

Bolt preload is used to tighten the flanges together to achieve sealing of the BFJA. Bolt preloading causes flange rotation (Jenco and Hunt, 2000). Krishna *et al.* (2007) defines flange rotation as the angular rotation of the flange about the radial axis due to bolt preloading. However, the influence of the bolt preloading is not restricted to the radial direction. A complete definition for flange rotation is the angular rotations in the radial and circumferential directions due to bolt preloading. Krishna *et al.* (2007) further states that the flange rotation is defined in ASME Section VIII-1 (2010a) as a constant value.

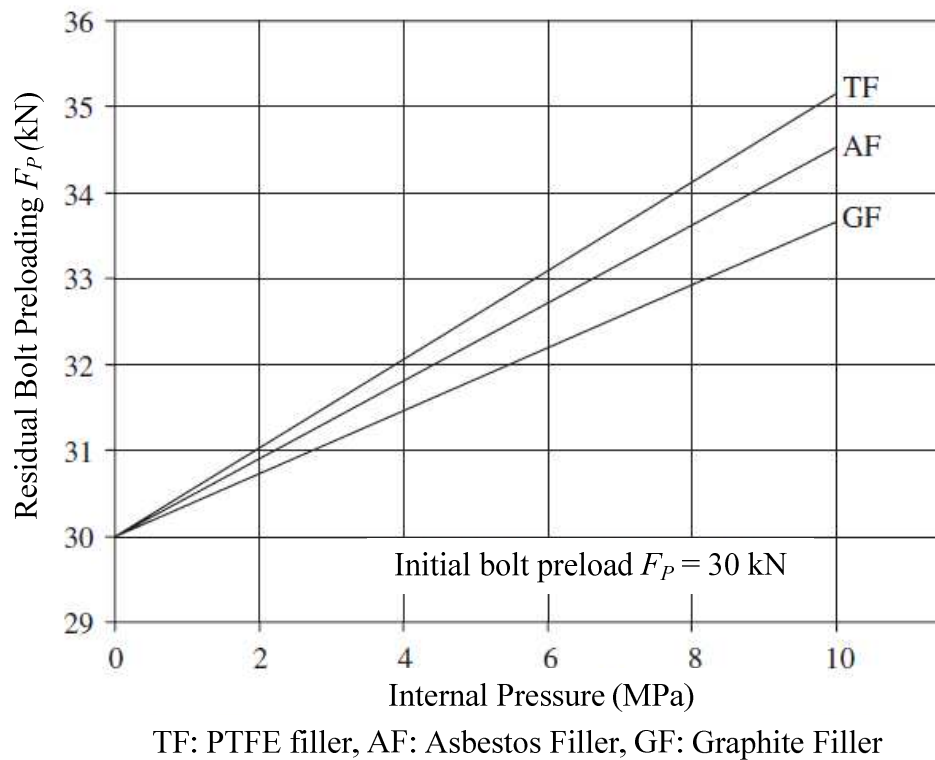


Figure 2-8: Influence of internal pressure on bolt preloading (Adapted from Krishna *et al.*, 2007).

However, as shown in Figure 2-8, the bolt preload increases when the internal pressure is applied on the BFJA, causing an increase in the flange rotation. Krishna *et al.* (2007) further showed that the constant value associated with flange rotation, given by ASME, is too high and that leakage would occur for values of flange rotation lower than those specified by ASME (2010a).

2.1.5 Material Modelling of the BFJA Bolt

Similar to flanges, bolts are expected to behave as an elastic-plastic and isotropic material. Krishna *et al.* (2007), Abid *et al.* (2008) and Mathan and Prasad (2009) all modelled the bolt as chromium steel (ASTM SA193-B7) in their respective studies.

2.1.6 External Loading on the BFJA Bolts

The influence of external loadings on the bolts, which includes the internal pressure and spatially-nonuniform thermal loadings, are discussed next.

2.1.6.1 Internal Pressure

Figure 2-8 shows that the axial component of internal pressure causes an increase in the residual bolt preload (Krishna *et al.* (2007)). The increase in axial bolt force due to internal pressure is linear, as shown in Figure 2-8, for a given spiral-wound gasket.

2.1.6.2 Thermal Loading

The bolts, in direct contact with the flange, are indirectly loaded due to the temperature gradients applied across the flanges. The relative thermal expansion between the flanges

and the bolts is responsible for an increase in the tensile forces in the bolts (Abid *et al.*, 2008).

2.1.7 Bolt Preload

On a BFJA, bolts provide the clamping force to seat the gasket on the raised-faces of the flanges to provide sealing. The initial load applied to the bolts to clamp the BFJA is termed the initial bolt preload. After the application of other external loads that may increase or decrease the bolt preload, the modified bolt preload is termed the residual bolt preload.

The BFJA is principally a tension joint and the bolts are loaded in tension. However, the bolts also experience a sustained-shear load due to the radial component of internal pressure acting on the flanges that transmit this pressure force as a shear load to the bolts. Transient shear loading in the bolts may also occur if there is relative motion between the flanges in the normal direction to the axis of the bolts (Bickford, 2008). Such relative motion may occur due to vibrations and/or thermal transients. This transient-shear loading can be neglected by assuming a stable configuration of the BFJA and slow transients (Bickford, 2008).

Figure 2-9 shows the effects of bolt preloading. A suitable initial bolt preload is important since it determines the effective gasket stresses in service. A low initial bolt preload may cause separation of the gasket when the BFJA is pressurized and cause leakage of the working fluid. A high initial bolt preload may cause crushing of the gasket and pivoting of the flange at that point (Jenco and Hunt, 2000; Bouzid and Derenne, 2002). Crushing is caused by improper loading such as tightening of the bolts beyond the

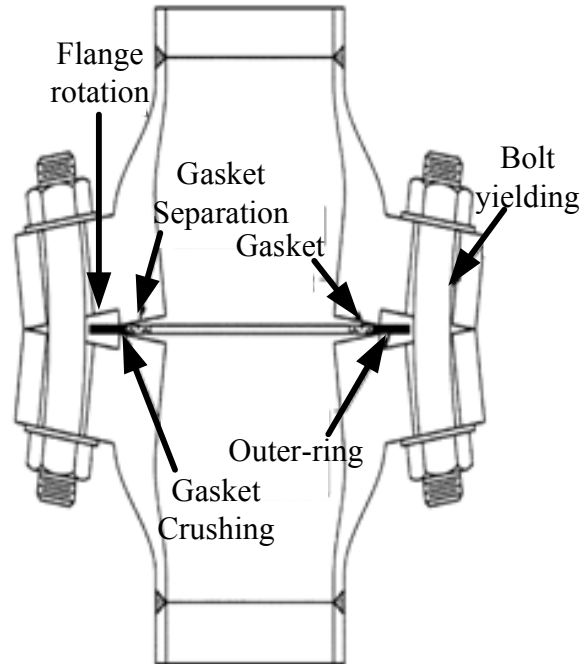


Figure 2-9: Gasket separation due to high preload (Reproduced from Jenco, 2000).

recommended torque. Crushing permanently damages the material of the gasket and the gasket can no longer perform its intended function. This may cause gasket separation as shown in Figure 2-9. Jenco and Hunt (2000) further suggested that a hard-joint reduces leakage problems. A hard-joint is where the gasket has been compressed to its maximum position and an increase in compressive loading cannot cause further deformation of the gasket (Jenco and Hunt, 2000). This happens when the additional thickness of the winding on the gasket is compressed and the outer metal ring of the spiral-wound gasket comes in direct contact with the flange surface and therefore the gasket cannot deform further. The stresses generated in the gasket for a hard-joint are the maximum limit for the gasket since any further stressing of the gasket would result in crushing of the gasket.

2.2 Grayloc[®] Clamp Connector (GCC)

GCC is known as a smaller, lightweight substitute for a BFJA (Grayloc, 2010a). This is apparent from Figure 2-10. For the given nominal pipe size and pressure rating, the GCC

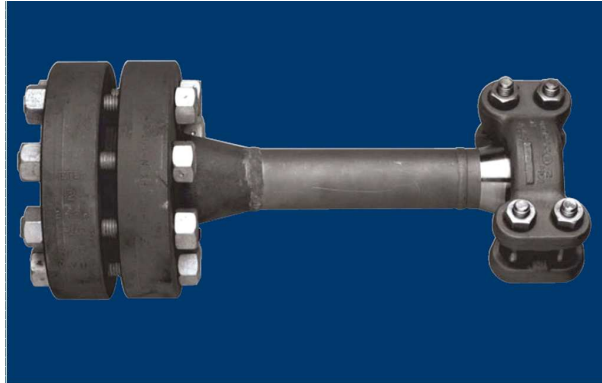


Figure 2-10: Compactness comparison of the GCC with the BFJA (Reproduced from Grayloc, 2012).

is the more compact connector and employs fewer bolts than the equivalent BFJA. Balouch (2011) selected a GCC for the CSCW loop for installation on the exit of the test section as the test section exit is elevated a significant distance from the floor making handling of heavy components difficult. The test section is required to be easily removable to allow different test sections to be installed. Therefore, to allow for ease of disassembly and compactness, the GCC was selected.

Since, the GCC is a proprietary design, material modelling becomes limited to the specifications of the manufacturer. External loadings on the GCC are similar to the BFJA, i.e. bolt preloading, internal pressure and thermal loads. The material modelling and external loadings are discussed in the following sections.

2.2.1 Material Modelling of the GCC

Material selection for the GCC was based on the design of the Carleton Supercritical Water (CSCW) experimental facility by Balouch (2011). Grayloc[®] (2012) recommends using hubs, clamps and bolts made of stainless steel for the high-pressure and high-temperature expected at the exit of the test section on the CSCW loop. Since the hubs, clamps and bolts are made of grades of stainless steel, the material behaviour is expected to be elastic-plastic and isotropic for the range of pressures expected on the CSCW loop. Grayloc[®] (2010a) recommends using a high-strength nickel alloy, Inconel-718, as the material for the seal-ring. The seal-ring has a MoS₂ lubricant coating to reduce wear and allow easy sliding of the seal-ring into the hub-recesses. The coating reduces friction between the surfaces and has been represented by a coefficient of friction of 0.1 (Shankara *et al.* 2008).

2.2.1.1 External Loading on the GCC

The external loadings on the GCC include bolt preloading, internal pressure and spatially-uniform and spatially-nonuniform thermal loads. Bolt preloading causes the clamps to push the hubs together, seating the seal-ring into the hub-recess (Grayloc, 2010a). The radial component of internal pressure reinforces the seal-ring into the hub-recess, energizing it and making the connector tighter. However, the axial component of internal pressure pushes the clamps apart. It is anticipated that thermal stresses will be generated if the GCC is subjected to elevated temperatures, that may or may not be spatially-uniform.

Dekker and Stikvoort (2004) conducted a study on the design rules for pipe clamp connectors. A Grayloc[®] clamp connector (GCC) is essentially a type of pipe clamp connector. Dekker and Stikvoort (2004) simplified the hub-recess that houses the seal-ring as a T-section, as shown in Figure 2-11. However, the geometric features between the hub and the seal-ring are lost due to simplifying the hub-recesses. Therefore, the deformation occurring in the seal-ring cannot be truly represented.

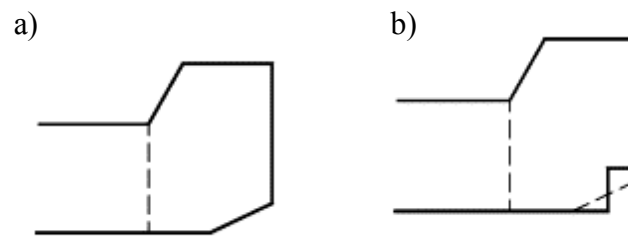


Figure 2-11: Geometry of the hub of the GCC a) true; b) T-section (Reproduced from Dekker, 2004).

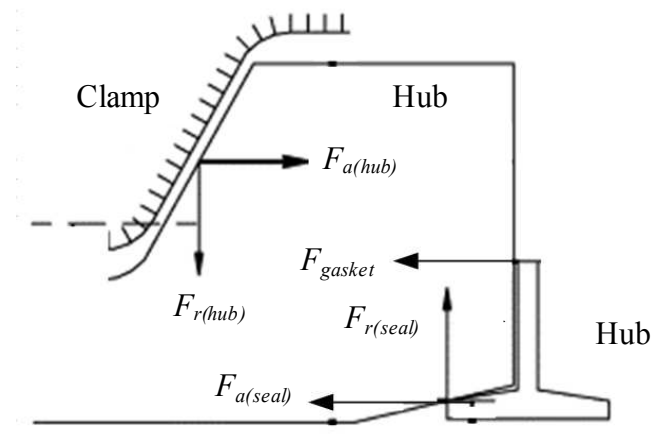


Figure 2-12: Force distribution diagram for a pipe clamp connector (Adapted from Dekker, 2004).

Dekker and Stikvoort (2004) present a force analysis on the pipe clamp connector including a force distribution diagram, as illustrated in Figure 2-12, which facilitates the understanding of the interaction of components of the GCC. All forces shown have been

resolved in the radial and axial directions. Of particular interest are the reaction forces at the hub/clamp mating surfaces. These reaction forces help in understanding the sliding friction expected between the hub and the clamp when the clamp presses on to the hub at an angle during clamping. The present study investigates the angular surface contact and its influence on the stresses generated in the hub and the clamp.

2.2.1.2 Pressure Loading

Internal pressure causes deformation of the seal-ring into the hub-recess and tightens the seal-ring in the recess between the two hubs (Dekker and Stikvoort, 2004). The hub material, which is typically softer than the seal-ring material, may plastically deform. Since the seal-ring is very small, the plastic deformation of the hub will be highly localized and may not contribute to the gross failure of the hub. However, the deformation of the seal-ring will be significant in relation to its size. It is imperative that the deformation of the seal-ring remains elastic to maintain its structural-integrity, under repeated cycles of internal pressure.

2.2.1.3 Thermal Loading

The freedom to thermally expand may be restricted due to the geometric configuration of the GCC assembly. Therefore, when the GCC is subjected to an elevated temperature, that may or may not be spatially-uniform, thermal strains may be generated in the GCC. Design rules given by ASME (2010d) are limited in considering the effect of thermal gradients. These design rules account for temperature only by considering the mechanical properties at the elevated temperature (ASME, 2010c; Brown *et al.*, 2002; PVEng, 2010).

2.2.1.4 Bolt Preloading

For a given internal pressure, the recommended initial bolt preload is higher for a bolt employed on a BFJA with a semi-metallic gasket, than the initial bolt preload for a bolt employed on a GCC. This is because a greater bolt force is required to ensure that the semi-metallic gasket is properly squeezed into the irregularities on the surfaces of the flange to provide sealing. It is anticipated that the initial bolt preload applied on the GCC will cause ‘clamp rotation’ similar to flange rotation on a BFJA. The present study investigates the effect of the bolt preload in conjunction with the internal pressure on the structural integrity of the GCC.

Chapter 3: Computational Setup of Finite Element

Analysis

To investigate the performance of the bolted-flange joint assembly (BFJA) and the Grayloc[®] clamp connector (GCC), a finite element (FE) analysis was performed on each of these assemblies. ANSYS[®] Mechanical 14.0, which is a commercial structural analysis software based on the finite element technique, was used for this purpose.

Since the computational approach is similar for the BFJA and the GCC models, their finite element analysis setups are discussed together. The analysis process for investigating the structural behaviour of the BFJA and the GCC involves the following steps: developing simplified geometric models for the BFJA and the GCC; mapping finite elements into the volume of the simplified geometric models; selecting a suitable function to describe variation of parameters within each element (shape function); defining material properties; applying boundary conditions; solving the system of equations; and analyzing (post-processing) the results. ANSYS[®] prepares the system of equations by discretizing the governing equations into a set of linear algebraic equations by approximating the terms in the governing equations using finite elements. This chapter covers the geometric modelling, mesh generation and boundary condition steps in detail, and briefly outlines the remaining steps for completeness. The analysis step is deferred to Chapters 4 and 5.

3.1 Model Geometry

Geometric models for the BFJA and the GCC were developed using Pro|ENGINEER[®] Wildfire[®] 5.0, which is a commercial parametric Computer Aided Design (CAD)

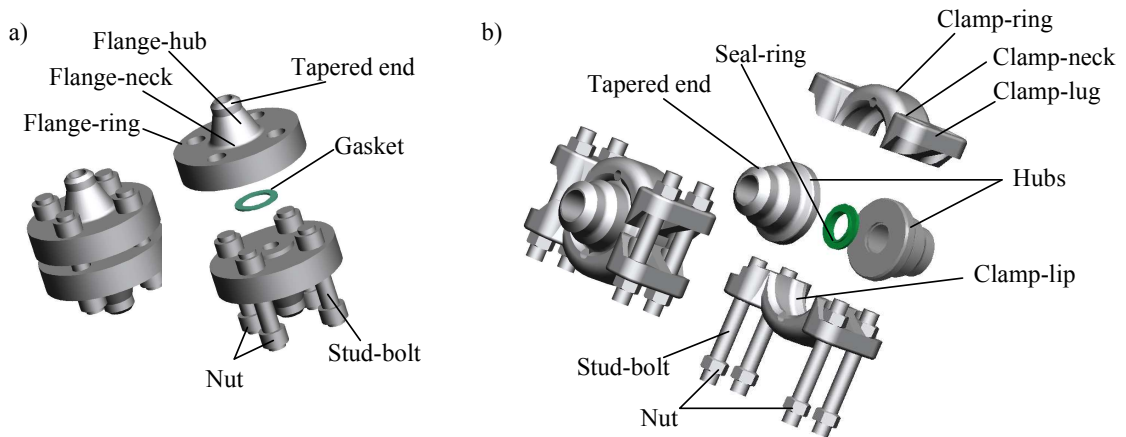


Figure 3-1: Geometric models of the a) BFJA and the b) GCC (Adapted from Grayloc, 2010b).

software. Figure 3-1 shows the exploded view of both the BFJA and GCC geometric models. The model dimensions for the BFJA are based on a standard ASME B16.5 Class 2500 nominal pipe size 1.5 flange, as shown in Figure 3-1a (Balouch, 2011). A nominal pipe size of 1.5 indicates that the nominal diameter of the pipe is 1.5 inches. The BFJA comprises of two flanges, four stud-bolts and eight nuts, and a semi-metallic gasket. The GCC comprises of two hubs, two clamps, four stud-bolts and eight nuts, and a seal-ring. The GCC dimensions are based on a 3-D model of a nominal pipe size 1.5 hub, as shown in Figure 3-1b, provided by Grayloc[®] (2010b). The salient dimensions of the BFJA and the GCC are shown in Figure 3-2 and Figure 3-3, respectively.

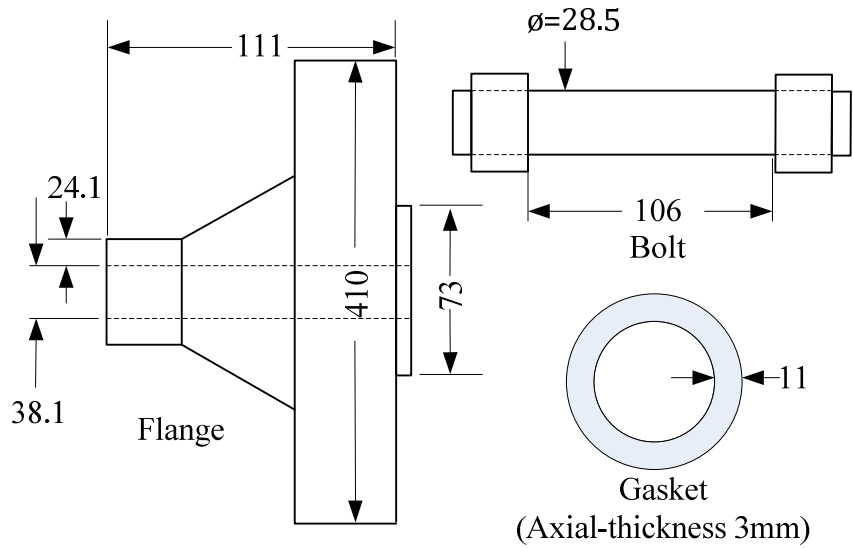


Figure 3-2: Several dimensions of components of the BFJA. All dimensions are in mm. Drawing is not to scale.

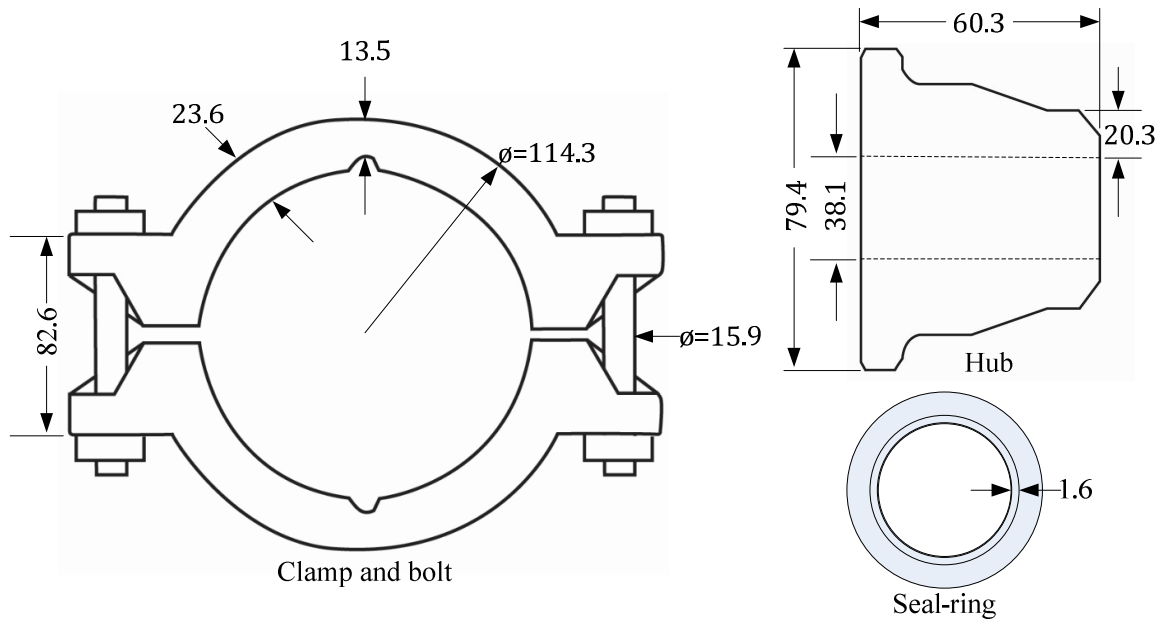


Figure 3-3: Several dimensions of components of the GCC. All dimensions are in mm. Drawing is not to scale.

The inner-ring and outer-ring of the gasket on the BFJA are not modeled; only the spiral-winding is computationally modelled in the present study. The inner-ring and outer-ring are not expected to interact with the flanges under normal operation and therefore are not

computationally modelled. The absence of the inner and outer ring will allow the winding to deform in the radial directions; however this radial deformation is avoided by employing an element that only allows deformation in the longitudinal direction (Section 3.2.2). To apply the bolt preloading in ANSYS[®], the stud-bolt and nuts were fused into a single cylindrical body, and will hereafter be referred to as a bolt (Abid *et al.*, 2008; Krishna *et al.*, 2007). The threads on the bolts were ignored by assuming a cylindrical bolt. These threads are a source of stress concentration and may lead to failure of the bolt. However, stress concentrations are expected to pose a problem only if the operating cycles of the BFJA and the GCC are high enough to potentially lead to fatigue failure. Fortunately, the operating cycles for the present application are anticipated to be quite low and fatigue is not a concern. Therefore, the bolt threads are neglected in the present computational model.

The taper at the ends of the flange of the BFJA (Figure 3-1a) and the hub of the GCC (Figure 3-1b) was removed to form a perfectly-radial contact with end-caps to allow simpler contact modelling (described in Section 3.6.2). The BFJA and GCC were further simplified based on geometric and loading symmetry (Figure 3-4). Geometric symmetry refers to planes of symmetry across which the model can be reflected to create the full geometry. Loading symmetry refers to planes of symmetry across which the loading is geometrically and functionally symmetrical.

The planes of geometric and loading symmetry of interest for the BFJA and the GCC are shown in Figure 3-4a and Figure 3-4b, respectively, by blue lines. For the BFJA shown in Figure 3-4a, the clamping force exerted by each bolt on a quarter geometry of the BFJA is identical to that exerted by each of the remaining three bolts, thus resulting in a loading

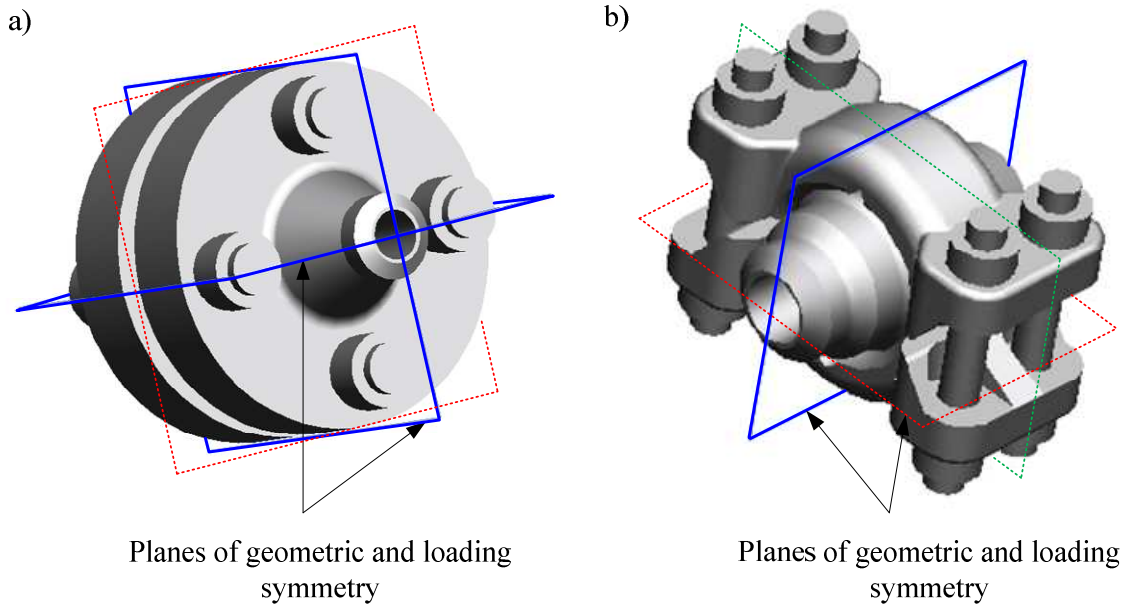


Figure 3-4: Planes of geometric and loading symmetry of the a) BFJA and the; b) GCC.

symmetry. For the GCC shown in Figure 3-4b, the clamping force exerted by one clamp-lug on a half geometry of the GCC is identical to the clamping force exerted by the second clamp-lug, again yielding a loading symmetry. The internal pressure loading is axi-symmetric along an axis that is at the intersection of the two loading symmetry planes for the BFJA (Figure 3-4a) and the GCC (Figure 3-4b). Based on these loading symmetries, both the BFJA and the GCC models can be reduced to one-quarter models. The geometric and loading symmetry represented by the red dashed line in Figure 3-4(a-b) for the BFJA and the GCC is not considered due to the computational need of applying the initial bolt preload to the centre of the bolts (described in Section 3.6.3). Accordingly, one-half of the GCC is computationally modelled instead of using a one-quarter model. Furthermore, the geometric and loading symmetry represented by the green dashed line, shown in Figure 3-4b, was also not considered to provide the option of loading each bolt in the clamp-lug to different loads. The variation of the initial bolt preload can be used to

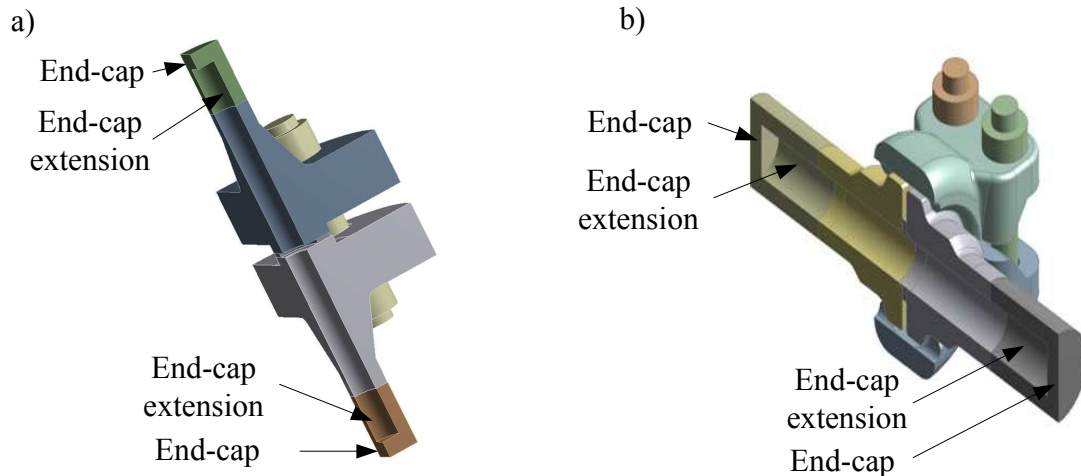


Figure 3-5: Simplified geometric models of the a) BFJA and; b) GCC.

simulate misalignment of the GCC due to bolt loading, if desired. However, while the computational model was developed to allow this option, misalignment due to bolt loading was not deemed necessary for investigation based on preliminary stress results.

The simplified geometric models of the BFJA and GCC in assembled configuration are shown in Figure 3-5a and Figure 3-5b, respectively. The BFJA and GCC are part of the CSCW loop, and under load do not operate in isolation. To model the interaction of the BFJA and the GCC with the rest of the CSCW loop, end-caps are introduced at the ends of the flanges of the BFJA and the ends of the hubs of the GCC (PVEng, 2010), as shown in Figure 3-5(a-b). The end-caps serve to produce the axial loading on the BFJA and the GCC that is expected to be present in the actual installation of these two assemblies on the CSCW loop. However, the presence of the end-caps in close proximity of the flange and the hub may result in unintended modification of the radial loads acting on the flange and the hub. To prevent these modifications, extensions in the form of pipe segments are used to keep the end-caps a conservative distance away from the flange and the hub, as shown in Figure 3-5(a-b). These extensions essentially represent the pipe segments of

corresponding diameter, wall thickness and material properties that would be welded to the flanges and the hubs in the actual installation. Through a sensitivity analysis examining the effect of proximity of the end-caps to the flanges on the BFJA and to the hubs on the GCC on the stress and strain distribution in the flanges and the hubs, a length of two diameters was found to be sufficient for these extensions.

3.2 Mesh Generation

The finite element meshes for the BFJA and the GCC computational models were generated using the ANSYS[®] Mechanical meshing tool. Since the geometries of the BFJA and the GCC models are complex, an unstructured hexahedral-dominant technique was used to map computational volumetric elements into the volumes of the computational models of the BFJA and the GCC. Hexahedral-dominant means that the meshing tool tries to create a mesh consisting of hexahedral elements; however, the meshing tool switches to tetrahedral elements in regions where it is not possible to generate good quality hexahedral elements.

A good quality element refers to an element that is not excessively distorted in shape. In ANSYS[®] Mechanical 14.0, element quality is determined by two factors: ANSYS[®] default shape checking metric; and the Jacobian ratio. The default shape checking metric is based on test-cases run by ANSYS[®] to establish the shape-integrity of an element and has a limit of 10^{-4} for sufficiently good quality of the volume element (ANSYS Inc., 2010). The Jacobian ratio is used to map an ideal finite-element on to the real finite-element in the computational model. The stretching required to map the ideal element on to the real element is the measure of distortion of the element. Mathematically, this is

achieved by evaluating the determinant of the Jacobian matrix at certain points within an element; the Jacobian ratio is the ratio of the maximum determinant to the minimum determinant evaluated at these points and has a limit of 40 for the volume element (ANSYS Inc., 2010). Both quality factors have a value of unity for an undistorted hexahedral element. These quality factors were found to exceed their respective limits in the regions shown in Figure 3-6, indicating that the hexahedral element has a high Jacobian ratio. To reduce distortion of the element in such instances, either the mesh can be refined, or another element shape that meets the shape checking criteria can be

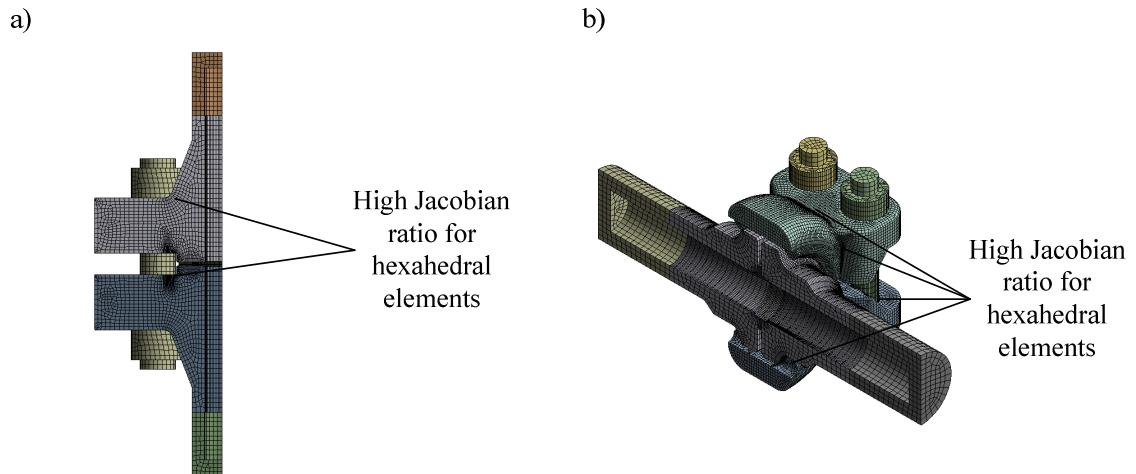


Figure 3-6: Mesh quality of the a) BFJA and; b) GCC.

employed. The former approach would greatly increase the number of elements. To circumvent this, geometrically compatible degenerate element shapes are employed in these regions (discussed in Section 3.2.1).

The selection of a finite element configuration to model the mechanical behaviour of a computational model depends on the degrees of freedom of the computational model; material properties of the particular component; and the surface and body loads that the

component is subjected to (ANSYS Inc., 2010). The BFJA and GCC have three translational degrees of freedom; elastic-plastic material properties for all components, except the semi-metallic gasket that has mechanical properties defined by a pressure-closure curve; and internal pressure, bolt preload and thermal loads as the surface load and body loads, respectively.

The density of the mesh, among other factors, depends on the order of the finite element; this is the order of the shape function that describes the variation of properties within the element. A linear element has an order of one. A quadratic element has an order of two, and so on. Increasing the order of the finite element can help capture the non-linear deformation field expected of the BFJA and the GCC computational models with fewer elements. A quadratic unstructured hexahedral mesh was deemed to be suitable to accurately model the stress and strain fields in the BFJA and the GCC with a number of finite elements that would afford acceptable computational times. The elements chosen for the present study are described in detail in the following sections.

3.2.1 SOLID186 and SOLID187 3D-Solid Elements

Quadratic volume elements SOLID186 (shown in Figure 3-7a) and SOLID187 (shown in Figure 3-7b) were used to mesh all solid components except the semi-metallic gasket. SOLID186 is a 20-node hexahedral volume element, while SOLID187 is a 10-node tetrahedral volume element. SOLID186 has a pure brick form and degenerate geometric forms including pyramids, prisms and tetrahedrals, as shown in Figure 3-7a. The brick option of the SOLID186 element maps the volumes of the BFJA and the GCC computational models with lesser elements than using only the tetrahedral option of

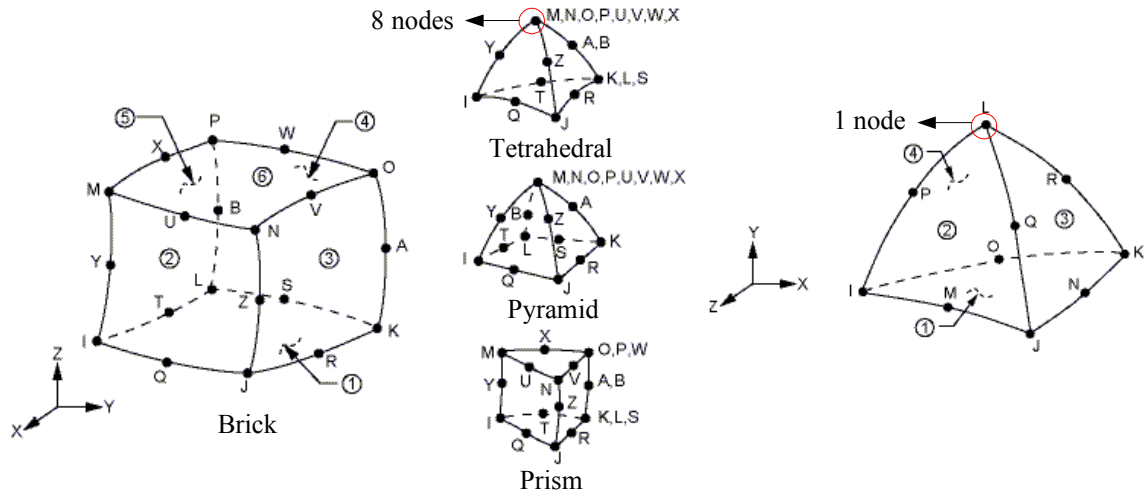


Figure 3-7: Geometric shapes of the (a) SOLID186 element and; (b) SOLID187 element (Reproduced from ANSYS Inc., 2010).

SOLID187. However, in certain regions where it is not possible to map a good quality element with the brick, pyramid and prism option of SOLID186 element, the tetrahedral element is preferred; e.g. for occupying regions shown in Figure 3-6. As such, the 20-node degenerate tetrahedral option (Figure 3-7a) of SOLID186 can be used for this purpose. However, the degenerate form of SOLID186 is computationally not efficient since eight nodes share one geometric location in the finite-element in comparison to a single node in the 10-node SOLID 187 tetrahedral element. Therefore, the 10-node SOLID187 tetrahedral element (Figure 3-7b) is employed instead of the 20-node SOLID186 degenerate tetrahedral element for a computationally more efficient mesh. The tetrahedral and hexahedral elements cannot directly conjoin in the finite element mesh for the computational models. The degenerate pyramid element serves as a transition element between these two elements; its base can connect with the brick element, and its triangular faces can connect with the tetrahedral elements.

Both SOLID186 and SOLID187 have three structural degrees of freedom, namely translation in the x-, y- and z-coordinate directions; have one thermal degree of freedom, i.e. body temperature; and are capable of capturing elastic-plastic material behaviour (ANSYS Inc., 2010). The requirements of the BFJA and the GCC computational models, stated before, are satisfied by the SOLID186 and SOLID187 elements and therefore these elements were employed to capture the behaviour expected of both computational models.

3.2.2 INTER194 3D-Interface Element

INTER194 is an interface element shown in Figure 3-8 and is designed to simulate gasket behaviour of the semi-metallic gasket of the BFJA. It is used to determine the through-thickness (local element x-direction) deformation of the semi-metallic gasket by determining the deformation of the top and bottom surfaces relative to the element midplane (ANSYS Inc., 2010). The gasket is modelled with a single layer of INTER194 interface elements. This element does not support lateral loads and therefore the gasket cannot be laterally loaded. The lateral loads on the gasket of the BFJA are expected to be

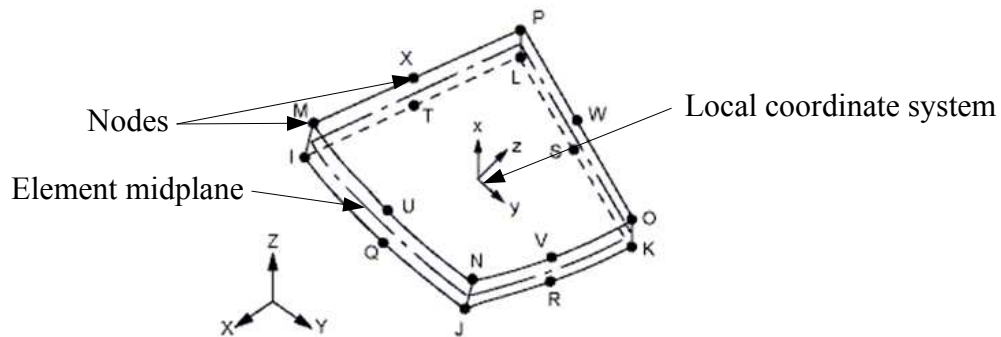


Figure 3-8: Interface element INTER194 (Reproduced from ANSYS Inc., 2010).

quite small compared to compressive loads, thus the capability of INTER194 interface element is deemed sufficient for modelling the behaviour of this gasket.

3.2.3 CONTA174 and TARGE170 3D-Contact Elements

Contact surface interaction is modelled using an element contact-pair of CONTA174 and TARGE170 (Figure 3-9). CONTA174 and TARGE170 are both 8-node quadratic contact and target surface elements, respectively. The contact and target elements have the same geometry and characteristics as the volume elements of the body that they are associated

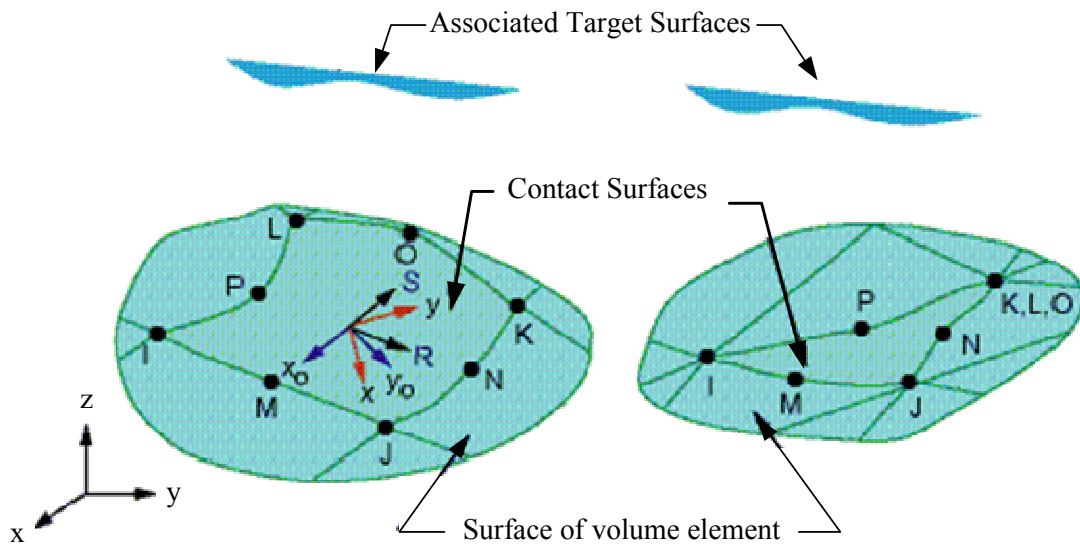


Figure 3-9: CONTA174 and TARGE170 elements overlaid on the contact body. (Reproduced from ANSYS, 2010).

with (ANSYS Inc., 2010). Target surface elements are assigned to the target body that is softer and/or has a larger contact surface. The contact elements are prescribed on the other interacting body, which is termed the contact body. For example, the flange/bolt contact surfaces were modelled by assigning the bolt contact surface with contact

elements CONTA174 and the larger flange contact surface with target elements TARGE170. A similar approach was applied to all the contact surfaces for both the BFJA and GCC computational models. The contact and target elements preferably should be of similar size to avoid reducing the quality of the elements that would occur due to stretching of either a contact or a target element to match the other element. To ensure a good match of all contact and target elements, the contact and target bodies were meshed to similar element densities on the surface.

The CONTA174 and TARGE170 elements were used to model frictional contact and bonded contact. Frictional contact allows the contacting surfaces to slide against each other based on the Coulomb friction model, and also allows for separation of the surfaces. Bonded contact does not allow either sliding or separation of the contacting surfaces. Frictional contact was modelled for the contact interaction between the components of the BFJA and between the components of the GCC, except with the end-cap extensions. Bonded contact was modelled for the contact interaction between the flange of the BFJA and the hub of the GCC with their respective end-cap extensions.

3.2.4 PRETS179 3D-Pretension Element

The initial bolt preload applied on the BFJA causes the flanges to be pressed on to the gasket. The flanges react to this initial preload, thereby inducing tension in the bolts. The mechanism is similar for the clamps of the GCC that induce tension in the bolts. The PRETS179 pretension elements were used on the bolts of the BFJA and the GCC to model this initial preload. The elements are termed pretension since the bolts are expected to be under tension before other operational loads are applied on the BFJA or on

the GCC. These 3-node pretension elements transform the bolt loading force into an effective longitudinal displacement of the bolt.

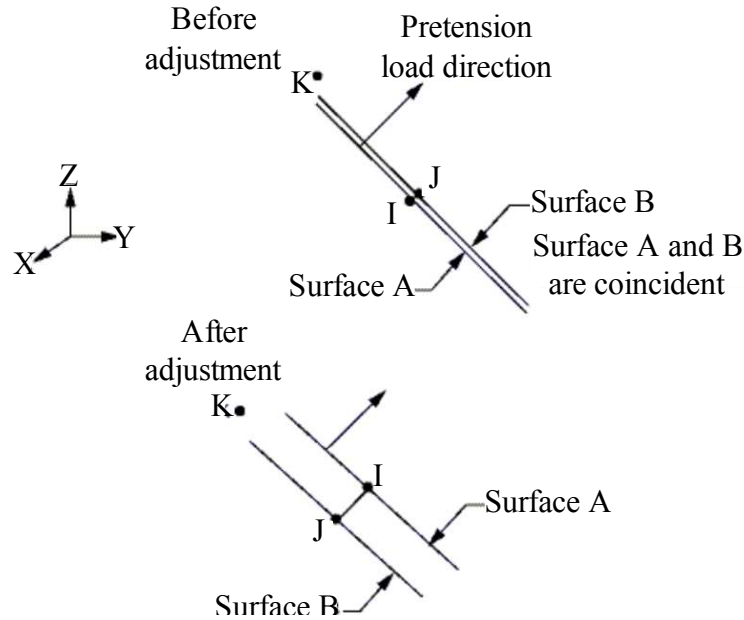


Figure 3-10: Schematic of PRETS179 element (Reproduced from ANSYS, 2010).

The mechanism of this displacement can be understood with the help of Figure 3-10 and Figure 3-11. A pretension section is created at the center of the bolt, where two coincident surfaces A and B are inserted. The pretension elements are overlaid on these two surfaces where node I and J of the PRETS179 element are associated with surfaces A and B, respectively. The third node K, associated with surface A, is responsible for transforming the bolt loading force into an effective displacement of nodes I and J. Initially, surfaces A and B are coincident where surface B serves as the fixed reference for the pretension element. The bolt loading force is applied on node K that displaces surface A equivalent to the applied bolt loading. The final position of node I with reference to node J is reported by ANSYS® as a ‘pretension-adjustment’ displacement for

the applied bolt loading. The pretension is locked as a permanent adjusted displacement representing the initial bolt preload (ANSYS Inc., 2010).

Any external loads acting on the bolts still have the freedom to stretch or compress the bolt; however this deformation is reported by either the volume or the surface elements and do not change the pretension-adjustment displacement. In practice, the initial bolt preload is locked when the bolts are assembled and the PRETS179 elements serve to mimic this behaviour.

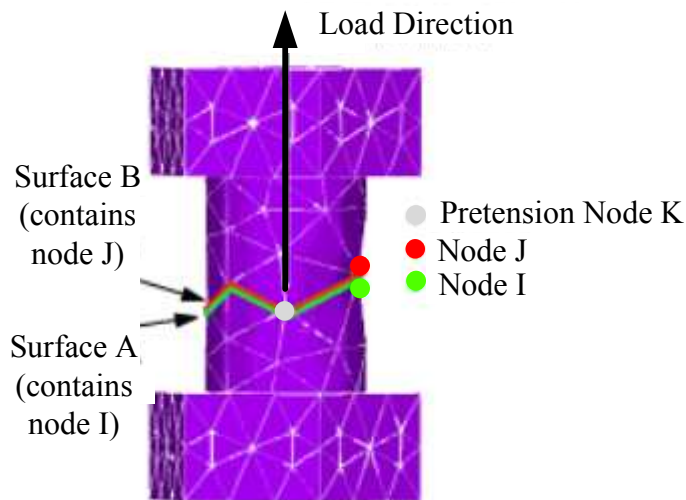


Figure 3-11: Location of cutting surfaces and the nodes of PRETS179 on the bolt (ANSYS Inc., 2010).

3.2.5 SURF154 3D-Surface Element

SURF154 is an 8-node quadratic surface element overlaid on the solid elements SOLID186 and SOLID187, and is used to apply the pressure loading on the computational models. The SURF154 element is overlaid on the pressure surfaces, i.e. the inner surfaces of the flanges of the BFJA, and the inner surfaces of the hubs and the seal-ring of the GCC, and their respective end-cap extensions and end-caps. These inner

surfaces are those surfaces that are in direct contact with the working fluid. The pressure load is applied normal to these surface elements.

3.2.6 Shape Function

SOLID186, SOLID187 are quadratic volume elements defined by a quadratic shape function for the deformation field inside the element. CONTA174, TARGE174, INTER194 and SURF154 also employ quadratic shape functions. A quadratic shape function represents the variation of the displacement field $[u]$ within the element with a polynomial function that has an order of 2. For details, the reader is referred to ANSYS® element library (ANSYS Inc., 2010).

3.3 Computational Models of the BFJA and the GCC

The finite element mesh of the BFJA and the GCC based on the elements described in the preceding sections are shown in Figure 3-12 and Figure 3-13, respectively. Despite using an unstructured mesh, certain regions (e.g., Figure 3-12(b-c) and Figure 3-13(b-d)) exhibit high-stress gradients and therefore cannot be represented by an average element size of 4 mm used for both computational models. Similarly, due to the non-uniform sticking and separation of mating surfaces, a finer surface mesh is needed to capture this non-linear behaviour. There are two ways to refine the mesh: h-type refinement that involves reducing the element size; and p-type refinement that involves increasing the order of the shape function (ANSYS Inc., 2010). For the present work, h-refinement was employed, while fixing the order of the shape function to 2. Therefore, the meshes were

refined in these high-stress gradient regions to average sizes of either 2 mm or 1 mm based on mesh sensitivity analyses.

By refining the mesh of the contact surfaces, the preferred requirement of similar mesh density of contact and target surfaces was automatically satisfied. However, this mesh

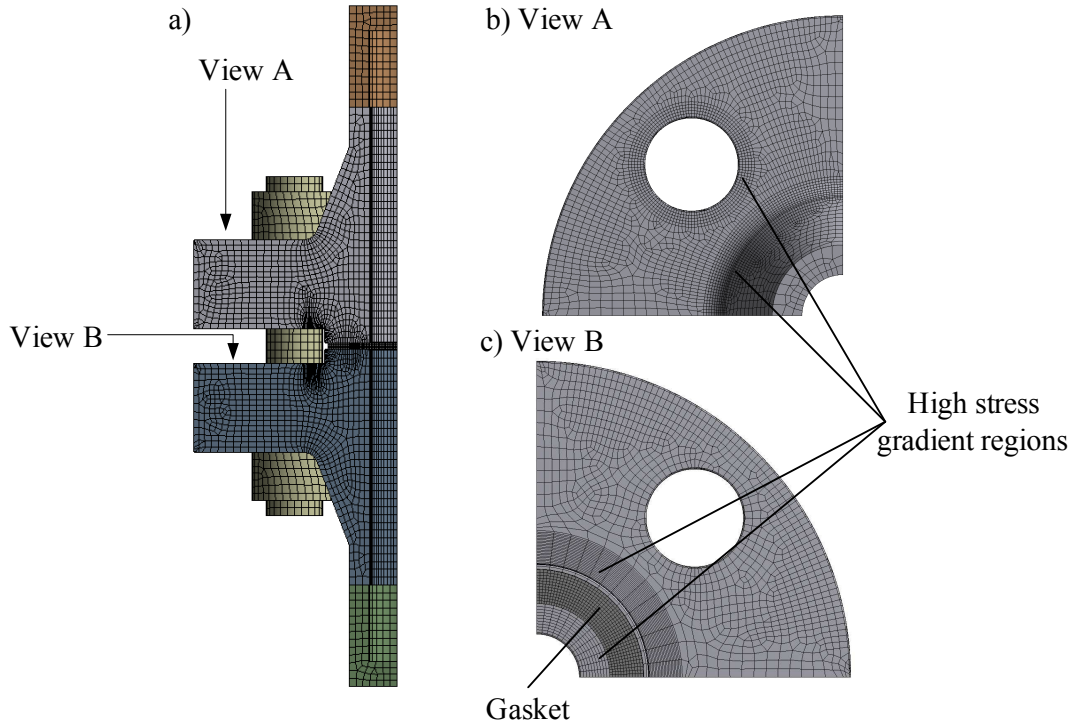


Figure 3-12: Final mesh of the BFJA.

refinement at specific locations caused a sudden jump between the sizes of finite elements of average size of 4 mm and 2 mm. To circumvent this element-size discontinuity, transition elements of gradually varying size were created.

The mesh density should be sufficient to capture the variation of stresses between adjoining finite-elements using the 2nd-order finite elements. To ensure a suitable mesh density, a mesh discretization error analysis was performed. This analysis sought to limit the variation of stresses between adjoining finite elements to a reasonable limit.

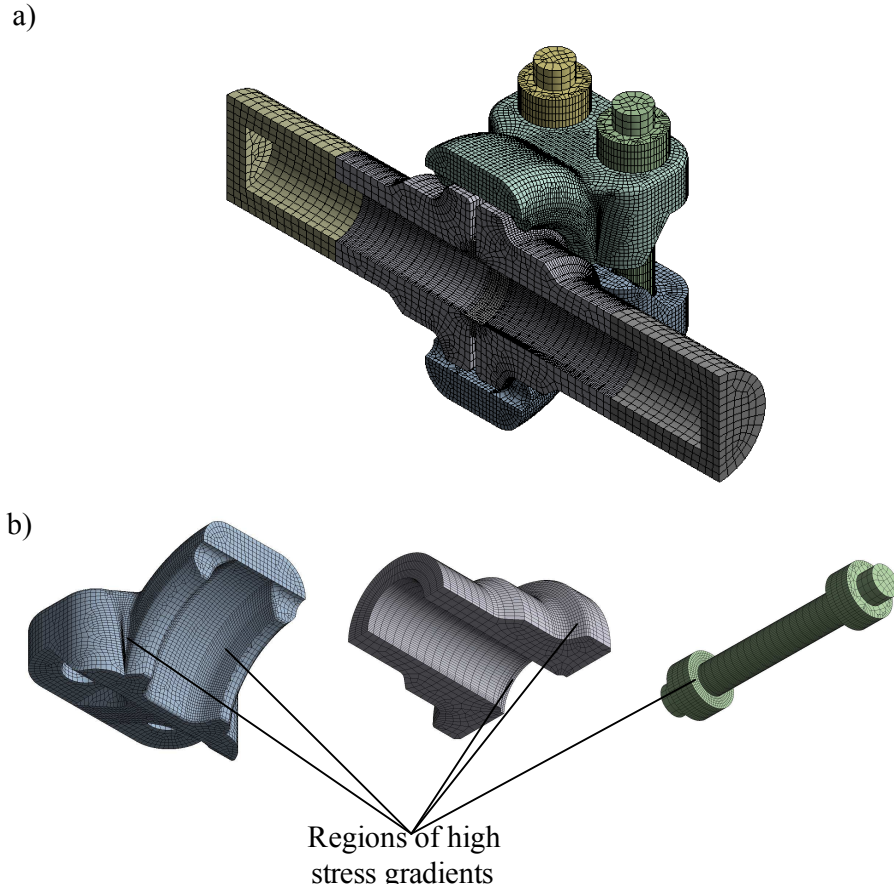


Figure 3-13: Final mesh of the GCC.

Consider one brick-element ' i ' inside the volume of a component, surrounded completely by similar brick-elements. A single corner node ' n ' of that brick-element will share the same spatial location with the one corner node from each of the surrounding seven elements. Therefore, the mean of the stresses at a node ' n ' of the surrounded brick-element ' i ' is determined by averaging the stress from all eight elements that node ' n ' shares the spatial location with. The stress error vector is developed as (ANSYS Inc., 2010):

$$\Delta\sigma_n^i = \sigma_n^a - \sigma_n^i \quad (3-1)$$

where $\Delta\sigma_n^i$ is the stress error vector at node ‘ n ’ of element ‘ i ’, σ_n^a is the average stress vector at node ‘ n ’ of element ‘ i ’ evaluated from the one corner node of all elements that share the spatial location with node ‘ n ’, σ_n^i is the stress vector of node ‘ n ’ of element ‘ i ’. This stress error vector for a single node ‘ n ’ can be extended to all nodes of that single finite element by developing the energy error norm as (ANSYS Inc., 2010):

$$e_i = \frac{1}{2} \int_{vol} (\Delta\sigma)^T [D]^{-1} (\Delta\sigma) d(vol) \quad (3-2)$$

where e_i is the energy error for element ‘ i ’, vol is the volume of the element, D is the stress-strain constitutive function matrix, $\Delta\sigma$ is the stress error vector evaluated by summing $\Delta\sigma_n^i$ for all nodes in the element. The magnitude of the energy error is used to determine the density of the mesh that is sufficient to capture the stress gradients. For the present study, the acceptable limit for the magnitude of the energy error, e_i , was set to 0.1mJ. This magnitude of the energy error limits the variation of the stress gradients to less than five percent, which is the limit set for finite element studies in design codes (ASME, 2010d; PVEng, 2010).

The initial solution for the computational models of the BFJA and the GCC was performed for an average element size of 4 mm. The components of both the BFJA and the GCC computational models were sectioned to determine if the internal volume elements satisfy the energy error limit and it was found such was the case for all components. Regions on the surface that exceeded the error limits were refined to a final average element size of 1 mm. The seal-ring was meshed with 1 mm volume elements due to its small size. Similarly, the gasket was meshed with 2 mm interface elements due to its small size. To accommodate the average element size of 1 mm for the contact

elements, the mesh of the clamps was refined to 2 mm to avoid poor quality transition elements between the surfaces and the internal volume. The final element count for each component is given in Table 3-1, with the element type and their count for each assembly given in Table 3-2.

Table 3-1: The average element size and count for the BFJA and GCC models

Assembly Type	Component	Avg. element size (mm)	Element Count
BFJA	Flange	4	67476
	Bolts	4	75167
	Gasket	2	248
	End-caps	4	986
GCC	Clamps	2	106334
	Hubs	4	28344
	Bolts	4	30426
	Seal-Ring	1	4118
	End-caps	4	2225

Table 3-2: The type and count of elements used for the BFJA and the GCC computational models.

Component Type	Type of Element	Element Count	% of total elements
BFJA	Hexahedral	81942	58
	Pyramid	35772	25
	Prism	2207	2
	Tetrahedral	21421	15
	Interface	552	-
	Pretension	315	-
GCC	Hexahedral	97660	57
	Pyramid	43407	25
	Prism	3236	2
	Tetrahedral	27144	16
	Pretension		-

In some instances, the displacement function does not converge despite the refinement of the finite-element mesh. On the contrary, the displacement function starts to diverge. When geometric segments with opposing deformation behaviour meet at a junction, the displacement behaviour cannot be resolved. In such instances, the displacement function is unable to converge to a single value. Such displacement functions are therefore unreliable since they do not capture the true deformation behaviour at that location. Similarly, the stresses derived from the displacement function are also unreliable. Stresses at such locations are termed singular stresses. These stresses are artificial and exist only in the numerical simulation.

3.4 Material and Mechanical Properties

Material and mechanical properties that are required to represent the behaviour of the flanges and bolts of the BFJA and the hubs, the clamps, the seal-ring and the bolts of the GCC computational models at room temperature of 25°C and their respective design temperatures of 260°C and 600°C, are listed in Table3-3, Table3-4 and Table 3-5, respectively. Material properties for the GCC are also evaluated at 1043°C, which is determined as the surface temperature for the test section in Section 3.8. The material and mechanical properties of the end-caps and the end-cap extensions are assigned similar to those of the flanges of the BFJA and the hubs of the GCC for the respective computational models.

Table 3-3: Material and mechanical properties of the components of the BFJA and GCC at room temperature of 25°C (ASME, 2010c).

Material	Stainless Steel			Inconel-718
Application	Flanges/Hubs	Clamps	Bolts	Seal-ring
Type-Grade	SA182-F316(H)	SA182-F304(H)	SA193-B8	SB-637
Density ρ (kg/m³)	8030	8030	8030	8193
Modulus of Elasticity E (GPa)	195	195	195	200
Poisson Ratio ν	0.31	0.31	0.31	0.294
Tensile Yield Strength (MPa)	207	207	345	1034
Thermal Conductivity k (Wm⁻¹C⁻¹)	14.1	14.8	14.8	11.1
Thermal Expansion α x 10⁻⁶ (mm/mm⁻¹C⁻¹)	15.3	15.3	15.3	12.8

Table 3-4: Material and mechanical properties of the components of the BFJA at the design temperature of 260°C (ASME, 2010c).

Material	Stainless Steel	
Application	Flanges	Bolts
Type-Grade	SA182-F316(H)	SA193-B8
Density ρ (kg/m³)	8030	8030
Modulus of Elasticity E (GPa)	178	178
Poisson Ratio ν	0.31	0.31
Tensile Yield Strength (MPa)	138	345
Thermal Conductivity k (Wm⁻¹C⁻¹)	18.8	18.8
Thermal Expansion α x 10⁻⁶ (mm/mm⁻¹C⁻¹)	17.4	17.4

Table 3-5: Material and mechanical properties of the components of the GCC at the design temperature of 600°C (ASME, 2010c).

Material	Stainless Steel			Inconel-718
Application	Hubs	Clamps	Bolts	Seal-ring
Type-Grade	SA182-F316(H)	SA182-F304(H)	SA193-B8	SB-637
Density ρ (kg/m³)	8030	8030	8030	8190
Modulus of Elasticity E (GPa)	151	151	151	167
Poisson Ratio ν	0.31	0.31	0.31	0.282
Tensile Yield Strength (MPa)	114	102	102	862
Thermal Conductivity k (Wm⁻¹C⁻¹)	22.6	22.6	22.6	20.9
Thermal Expansion α x 10⁻⁶ (mm/mm⁻¹C⁻¹)	18.8	18.8	18.8	14.8

The tensile yield strength of a material is a function of temperature and decreases with increasing temperature. For instance, the grade of stainless steel used for the clamps loses approximately 50% of its tensile yield strength as its temperature is increased from 25°C to 600°C. To account for this degradation, the material properties are taken at the design temperature. A high yield strength material is used for the seal-ring since it undergoes significant deformation during service. The semi-metallic gasket used on the BFJA is a spiral-wound gasket and its mechanical behaviour is represented by a pressure-closure (p-c) curve, as illustrated in Figure 3-14.

Experimental data for the pressure-closure curve of the spiral-wound gasket was found only at 100°C in published literature. Therefore the results of the finite element analysis do not take into account the degradation of the gasket at the design temperature of 260°C for the BFJA.

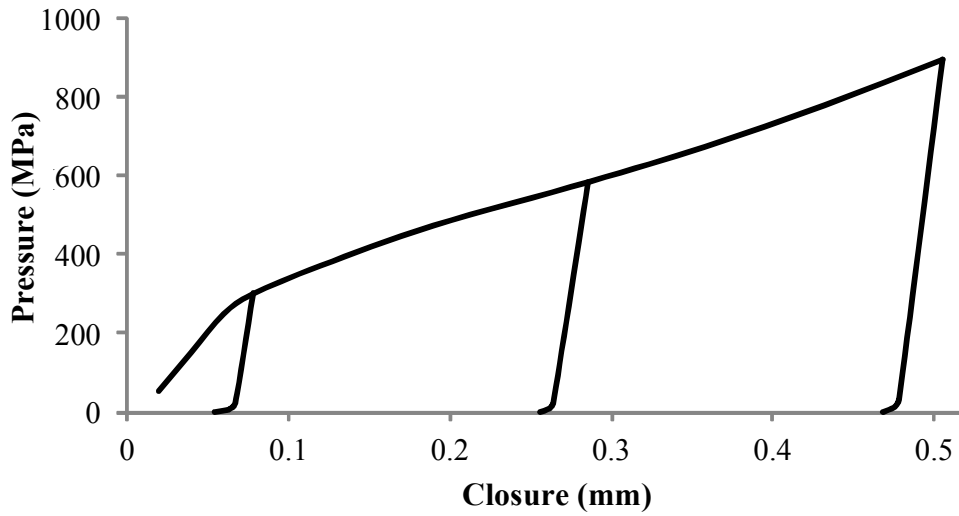


Figure 3-14: The pressure-closure curve for the semi-metallic gasket used on the BFJA (ANSYS Inc., 2010).

3.5 Finite Element Formulation

The finite element equations for numerical analysis can be obtained by two methods: solving the governing differential equations using the weighted-residual method (Rao, 2011); or developing the finite element equations by employing the principle of virtual work. ANSYS[®] uses the latter approach in its finite element formulation. The principle of virtual work states that for a small virtual displacement, the internal virtual work is equal to the external virtual work. Based on this principle, the finite element matrix equation developed for the computational models in the present work is given by,

$$[K_E][u] = [F_E^{nd}] + [F_E^{pr}] + [F_E^{th}] \quad (3-3)$$

K_E is the element stiffness matrix and depends on the strain-displacement relation and the stress-strain constitutive relation; F_E^{nd} is the nodal force matrix applied to the element and depends on the bolting preload; F_E^{pr} is the element pressure vector matrix, and is a

function of the internal pressure; F_E^{th} is the element thermal load vector matrix and depends on the temperature gradients applied to the BFJA and the GCC computational models. The solution of Equation 4-3 gives the displacement field $[u]$ for the BFJA and the GCC computational models at the nodes of the finite elements. The strain field is derived from this displacement field using the strain-displacement relationship. This strain field is then used to evaluate the stress field using the respective constitutive stress-strain relationship for each component.

3.6 Boundary Conditions

The type of boundary conditions for the BFJA and the GCC models are similar since they are subjected to similar design parameters. The boundary conditions include restraining rigid body motion; applying loading symmetry to the simplified geometric models; applying the initial preload to the bolts; applying internal pressure; and assigning surface temperatures on the BFJA and the GCC computational models. The external loads are applied in three loading steps. The sequence of applying these boundary conditions and their point of application are explained in the following sections.

3.6.1 Rigid Body Motion and Symmetry Condition

To avoid rigid body motion, the face of one end-cap of the BFJA and the GCC computational models is restrained in space by assigning the respective face as a fixed support, as shown in Figure 3-15(a-b). This artificial restraint, while preventing rigid body motion of the assemblies, imposes an artificial zero displacement locally. However, since the end-caps are outside the region of influence for the two assemblies, the

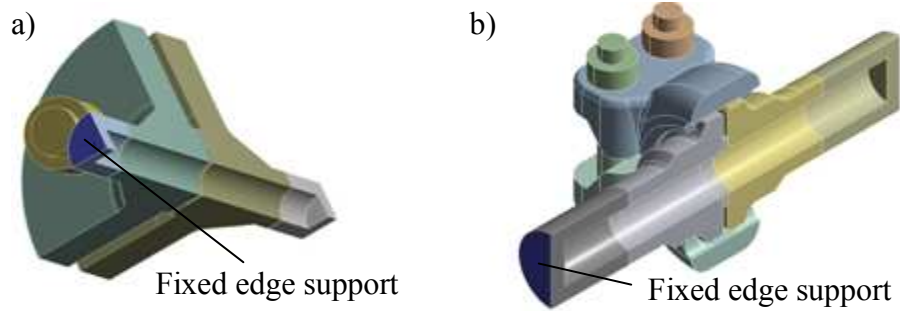


Figure 3-15: Fixed support applied on the computational models of the a) BFJA; b) GCC.

displacement field of the regions of interest of the BFJA and the GCC computational models should not be affected.

As was described in Section 3.1, the geometric models of the BFJA and the GCC were simplified based on geometric and loading symmetry. Accordingly, the computational models should not deform in the direction normal to these symmetry planes since that space is occupied by the corresponding symmetric part for the two assemblies. Therefore, the deformation normal to the blue shaded surfaces is restrained on both computational models using the symmetry boundary condition, as shown in Figure 3-16(a-b).

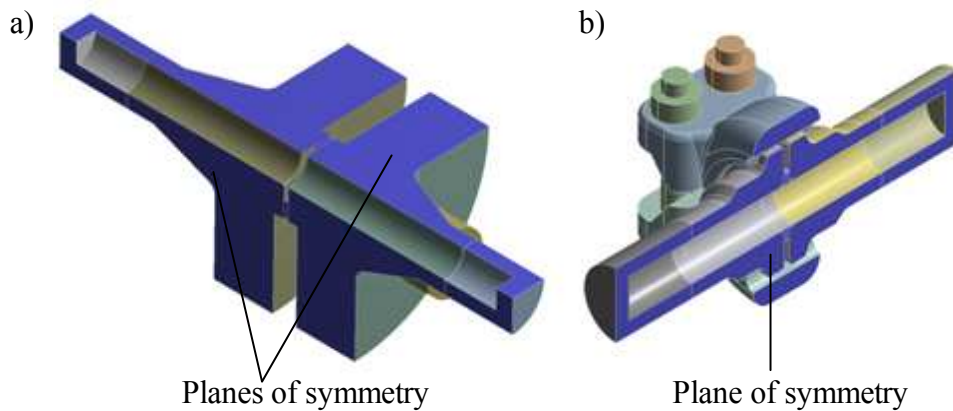


Figure 3-16: Symmetry condition applied on the section-faces of the computational model of the a) BFJA; b) GCC.

3.6.2 Contact-Surface Interaction

Frictional contact between surfaces is modelled using the Coulomb friction model. This model states that if the shear stress between any two contacting surfaces remains below a limiting friction/shear stress, the surfaces stick to each other. However, if the shear stress increases beyond the limiting value, the surfaces slide with resistance relative to each other.

The BFJA has six mating surfaces or contact-surface pairs that are categorized based on the coefficient of friction and material of the contacting bodies. Similarly the GCC has four mating surfaces or contact-surface pairs. The contact-surface pairs for the BFJA are shown in Figure 3-17(a-c). Similarly, the contact-surface pairs for the GCC are shown in

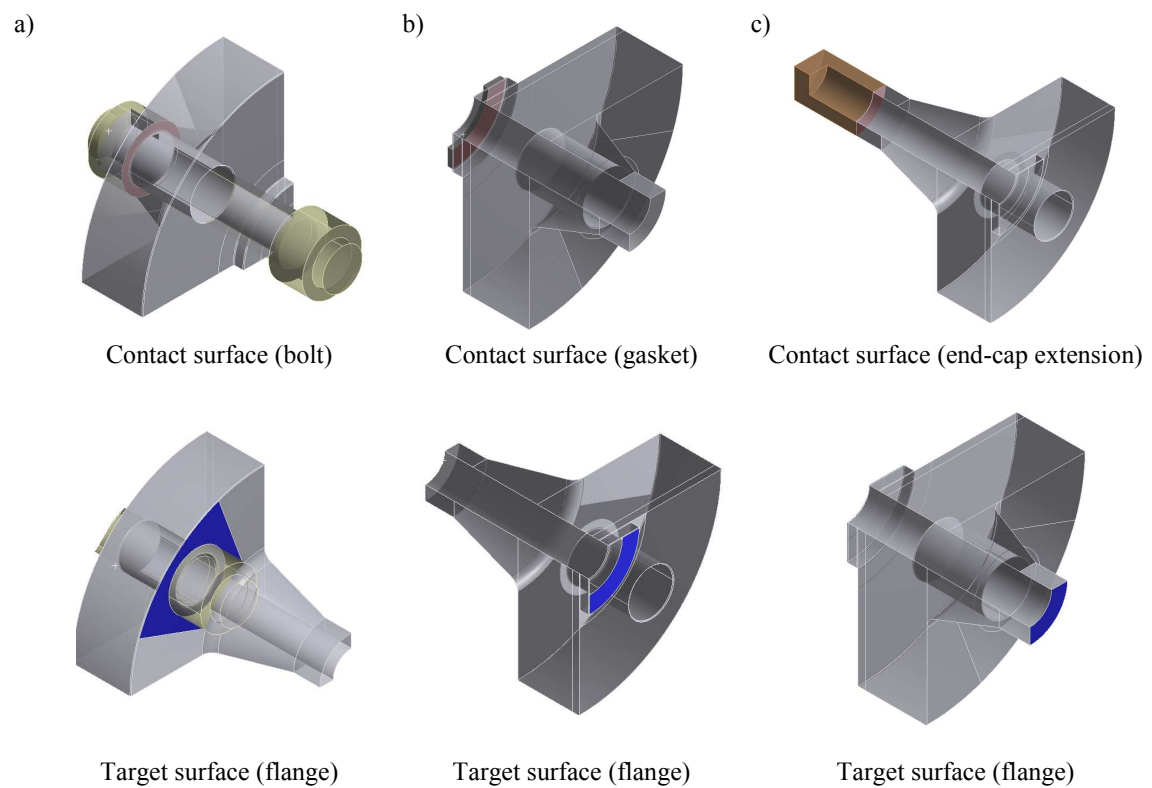


Figure 3-17: Contact-surface pairs of the BFJA computational model: a) bolt/flange; b) gasket/flange; c) end-cap extension/flange.

Figure 3-18(a-d). The contact-surface pairs and their corresponding coefficients of friction for both the BFJA and the GCC are listed in Table 3-6.

The flange/end-cap extension mating surfaces of the BFJA and the hub/end-cap extension mating surfaces of the GCC are considered to be welded joints and are therefore represented as bonded surfaces. Bonded surface contact does not allow sliding or separation of the interacting surfaces and therefore longitudinal and shear forces will be

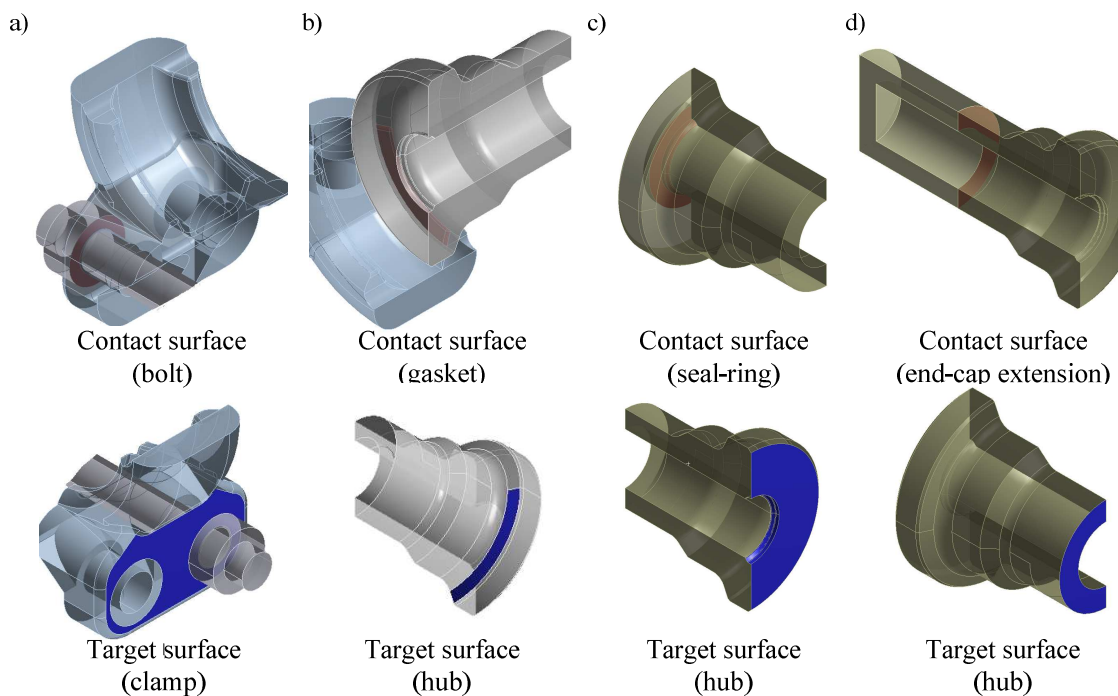


Figure 3-18: Contact-surface pairs of the GCC computational model: a) hub/clamp; b) clamp/bolt; and; c) flange/end-cap extension.

transmitted under load from the flange and the hub to their respective end-caps. The actual welding will create a radial joint and load transfer will occur across this radial joint. Tapered contact between the flange and the hub with the end-cap extension is not the true representation of the physical behaviour of the flange and the hub, since the load transfer occurs radially across the radial welded joint. Therefore, the taper on the ends of

the flange and the hub was removed for the respective computational models of the BFJA and GCC to make them perfectly radial and hence allow radial contact.

Table 3-6: Contact-surface pairs for the BFJA and GCC computational models with their associated coefficients of friction.

	Surface 1	Surface 2	Type of Contact	Coefficient of Friction
BFJA	Bolt	Flange	Sliding friction	0.4 (Artoos <i>et al.</i> , 1994)
	Gasket	Flange	Sliding friction	0.1 (Ramsdale, 2006)
	End-cap extension	Flange	Bonded Contact	1.0
GCC	Hub	Clamp	Sliding friction	0.4 (Artoos <i>et al.</i> , 1994)
	Bolt	Clamp	Sliding friction	0.4 (Artoos <i>et al.</i> , 1994)
	Seal-ring	Hub	Sliding friction	0.1 (Shankara <i>et al.</i> , 2008)
	End-cap extension	Hub	Bonded contact	1.0

3.6.3 Initial Bolt Preload

The value of the initial bolt preload is different for the two computational models. For the BFJA computational model, an initial bolt preload, F_p , of 60,000 N was determined based on ASME design rules for flange connections (ASME, 2010b), and was used as the initial preload in the iterative simulation for calculating the optimum initial bolt preload.

For the GCC computational model, an initial bolt preload, F_p , of 6,000 N was determined based on ASME design rules for clamp connections (ASME, 2010b; Grayloc, 2012). The initial bolt preload is the first external load applied on the BFJA and GCC computational

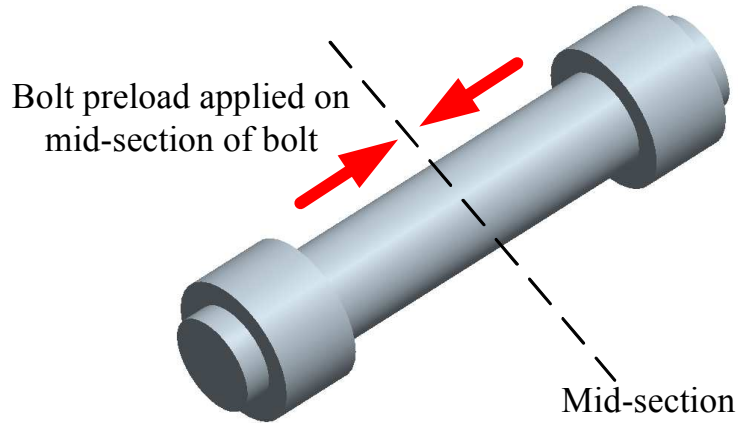


Figure 3-19: Bolt preloading.

models, and is the only load applied in the first load step of the simulation. The initial bolt preload applied on the bolt is shown in Figure 3-19. After selecting the bolt body and assigning the pretension-adjustment direction along the longitudinal axis of the bolt, the bolt loading is applied as a force. In the second load step, the bolt preload is locked as a pretension-adjustment displacement, as explained in Section 3.2.4.

3.6.4 Internal Pressure

The inner surfaces of the flanges of the BFJA and the inner surfaces of the hubs and sealing of the GCC, and their respective associated piping are subjected to internal pressure of 27 MPa, as shown in Figure 3-20. The inner surfaces are those surfaces that are in direct contact with the working fluid. The internal pressure applied on the end-caps simulates the axial loading that the rest of the CSCW loop will impose on the BFJA and the GCC. The radial component of the internal pressure is not applied on the inside face of the semi-metallic gasket due to the modelling limitations of the interface element INTER194. However, the radial pressure force acting on the gasket is $1/3^{\text{rd}}$ of the axial

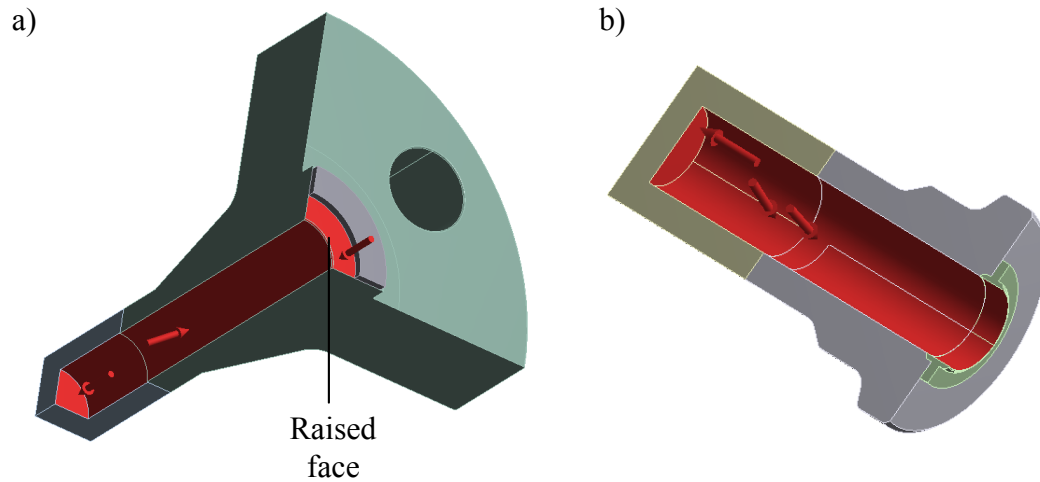


Figure 3-20: Internal pressure applied on the inside surfaces of the a) BFJA and b) GCC. Only one-half of the inside surfaces are shown for effective illustration.

pressure force that in addition to the compressive bolt loading, dominates the force on the gasket. Accordingly, the radial pressure force on the gasket can be neglected.

The internal pressure is the second external load applied on the BFJA and the GCC computational models and is applied in the second load step of the simulation. Therefore, the second load step involves locking the initial bolt preload and applying internal pressure on the computational models of the BFJA and the GCC. The influence of internal pressure on a bolted BFJA or a bolted GCC is isolated from the temperature gradients by applying only the internal pressure in the second load step of the simulation.

The computational models of the BFJA and the GCC are illustrated in Figure 3-21a and b, respectively, with the constraints of symmetry, bolt preload and internal pressure imposed on them.

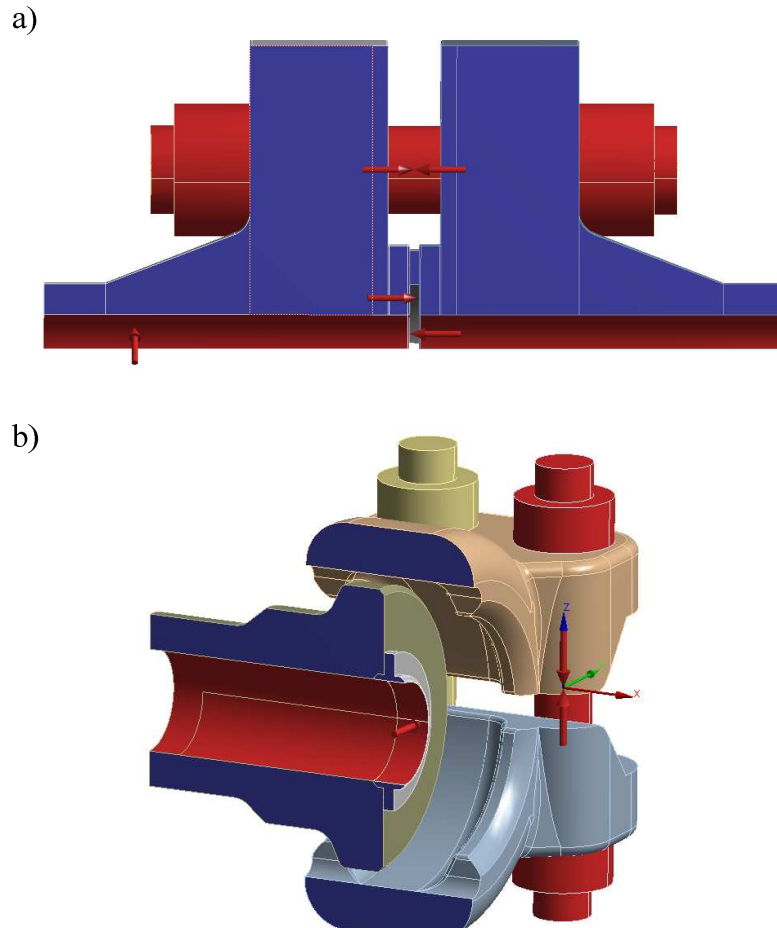


Figure 3-21: Constraints of symmetry bolt preload and internal pressure imposed on the a) BFJA; b) GCC.

3.6.5 Thermal Loadings

The modular test section on the CSCW loop (Figure 1-1) is electrically heated to produce a bulk-fluid temperature, T_w , of 600°C at 27 MPa to achieve the desired supercritical thermodynamic state for water. This hot working fluid discharging from the test section is then cooled down inside the heat exchanger to a subcritical bulk-fluid temperature of 260°C and after going through the pump to offset the frictional losses in the CSCW loop that are of the order of 100 kPa, is returned to the inlet of the test section. The BFJA is installed upstream of the test section, while the GCC is installed at the exit of the test

section. Due to the difference in temperatures between the working fluid and the ambient temperature, T_a , respective temperature gradients are generated across the BFJA and the GCC. The ambient temperature is conservatively chosen as 15°C to allow for overcooling of the lab facility or insufficient heating of the lab during cold weather.

To determine the inner and outer surface temperatures of the BFJA and the GCC for the above-noted operating conditions, certain assumptions and simplifications need to be applied. If all parts of the CSCW loop, except the BFJA and the GCC, are assumed to be perfectly insulated, stray heat transfer would occur only across the two assemblies. This assumption allows us to assign the bulk-fluid temperature of 260°C as the inlet temperature, T_w , to the BFJA. The same cannot be assumed for the GCC. As will be shown in Section 3.8.1, the test section exit heated-surface temperature value exceeds the bulk-fluid temperature of 600°C. Two thermal models were developed for the GCC. The first thermal model, termed the fluid-thermal model, is identical to that of the BFJA and assigns the bulk-fluid temperature at the inlet of the GCC as 600°C. The second thermal model, termed the surface-thermal model, conservatively assigns the inner surface temperature equal to the temperature of the heated-surface of the test section at the test section discharge. The true temperature gradient generated across the GCC is expected to be between these two thermal models.

Based on the anticipated relative magnitude of the temperature gradients affecting the BFJA assembly, it is assumed that the heat transfer is one-dimensional in the radial direction. This idealization allows the assignment of a constant inner surface temperature on the BFJA. While axial heat conduction affects the temperature of the GCC, since the thermal resistance of the GCC in the axial direction is small compared to its thermal

resistance in the radial direction, axial temperature gradients in the GCC are neglected as well.

In practice, thermal contact resistance exists at all of the contact interfaces on the BFJA and the GCC. However, for simplicity of modelling the thermal loading, contact resistance was assumed to be zero. This assumption reduces the conservatism of the present computational analysis, thus future work on the effects of thermal contact resistance is recommended.

Based on these considerations, the heat transfer analyses for the BFJA and the GCC are presented in the next two sections.

3.7 Heat Transfer Analysis for the BFJA

Due to the complex geometry of the BFJA, heat transfer from the outer surfaces of the BFJA cannot be predicted directly using conventional heat transfer correlations since they are limited to simple geometries, such as cylinders, flat surfaces transferring heat in isolation. The geometry of the BFJA may be broadly divided into primitive geometric entities. However, the convection heat transfer on the exposed surfaces of these entities will interact with each other due to their close proximity to each other and cannot be reliably modeled using the available correlations. Simplifying the BFJA into a spherical shape provides an approximate assessment of the surface temperatures expected in operation. The thermal sphere and its associated thermal resistance network are developed for the BFJA as illustrated in Figure 3-22. The thermal sphere circumscribes the BFJA reasonably well; the inner and outer surface areas of the thermal sphere

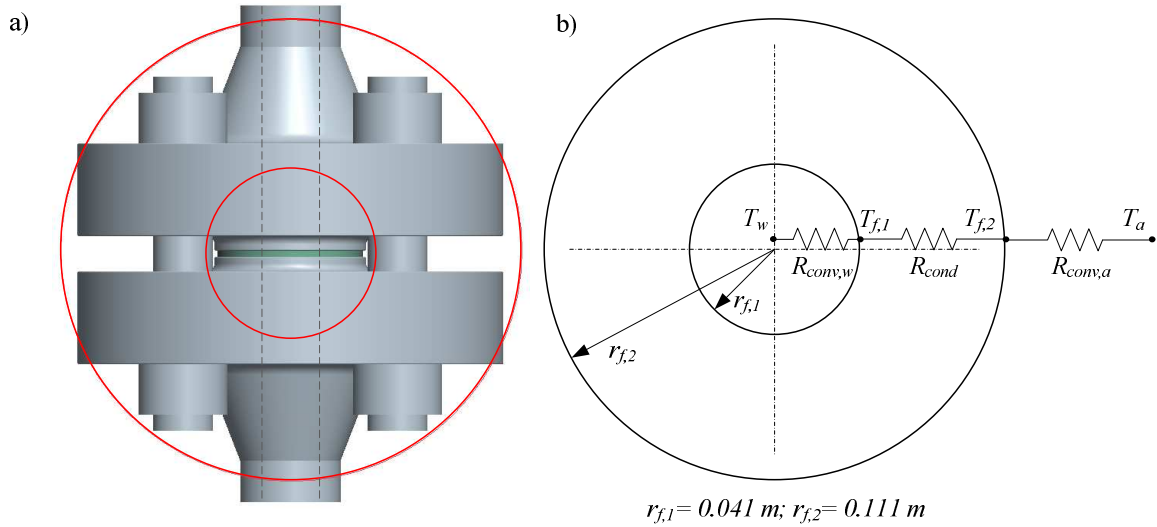


Figure 3-22: Simplified BFJA geometry for heat transfer analysis a) superimposed on the geometric model; b) shown with the thermal resistance network.

respectively match the inner and outer surface areas of the original geometry. Furthermore, suitable heat transfer correlations for the sphere indicate that the heat loss generated from the outer surfaces of the sphere will be higher than from equivalent cylindrical surfaces at any orientation. Therefore, the thermal sphere provides a conservative heat loss that is greater than the heat loss occurring in the segments of the actual BFJA geometry that resemble cylindrical shapes.

The heat transfer from the working fluid to the ambient air is resisted by the convective and conductive thermal resistances, as illustrated in Figure 3-22, and the total value of which is obtained through:

$$R_{tot} = R_{conv,w} + R_{cond} + R_{conv,a} \quad (3-4)$$

where R_{tot} is the total thermal resistance to the heat loss and is given as (Cengel, 2004):

$$R_{tot} = \frac{1}{4\pi(r_{f,1})^2 h_w} + \frac{r_{f,2} - r_{f,1}}{4\pi r_{f,2} r_{f,1} k_f} + \frac{1}{4\pi(r_{f,2})^2 h_a} \quad (3-5)$$

In this equation, h_w is the convection heat transfer coefficient related to the flow of the working fluid; k_f is the thermal conductivity of the flange material; h_a is the convection heat transfer coefficient associated with the motion of the surrounding air. The heat loss can then be estimated using the following relation (Cengel, 2004):

$$Q_{loss} = \frac{T_w - T_a}{R_{tot}} \quad (3-6)$$

Once Q_{loss} is determined from Equation 3-6, $T_{f,1}$ and $T_{f,2}$ can be determined using:

$$Q_{loss} = \frac{T_w - T_{f,1}}{R_{conv,w}} \quad (3-7)$$

and,

$$Q_{loss} = \frac{T_{f,2} - T_a}{R_{conv,a}} \quad (3-8)$$

respectively. With these surface temperatures used as thermal boundary conditions, the thermal stresses in the BFJA are determined based on the finite element model presented in Section 3.3.

3.7.1 Determination of the Surface Temperatures

In order to quantify the total thermal resistance, R_{tot} , and thereby the surface temperatures, the convection heat transfer coefficients need to be determined. The forced-convection heat transfer coefficient, h_w , is fundamentally governed by the Reynolds number:

$$Re = \frac{\rho V L_{ch}}{\mu} \quad (3-9)$$

where ρ is the density of the working fluid; V is the mean velocity of the flow; L_{ch} is the characteristic length associated with the flow and in this instance is set equal to the inner diameter of the flange; and μ is the dynamic viscosity of the working fluid. In terms of the mass flow rate \dot{m} , the Reynolds number is given as:

$$Re = \frac{\dot{m}(2r_{f,1})}{\mu A_c} \quad (3-10)$$

where \dot{m} is the maximum mass flow rate and is equal to 1.038 kg/s for the CSCW loop (Balouch, 2011); A_c is the cross-sectional flow area of the flange. The maximum flow rate is chosen for the present heat transfer analysis since it predicts the highest value of Reynolds number, in turn estimating the maximum value for h_w . It is evident from Equation 3-7 that the inner surface temperature, $T_{f,1}$, will be highest if h_w is maximum for a given Q_{loss} . h_w is represented in non-dimensional form as the Nusselt number, Nu . For the forced-convection heat transfer, Nu is a function of Re and the Prandtl number, Pr . The Prandtl number is given by:

$$Pr = \frac{\mu c_p}{k_w} \quad (3-11)$$

where c_p is the isobaric specific heat of the working fluid, and k_w is the thermal conductivity of the working fluid. As the flow in the BFJA approximates the flow in a pipe, the Nusselt number can be estimated using the forced-convection heat transfer correlation that is proposed for pipe flows. For a Re value of 1.5×10^5 and Pr value of 0.794 which corresponds to a bulk-fluid (water) temperature of 260°C and internal pressure of 27 MPa, the suitable Nusselt number correlation is given by (Cengel, 2004):

$$Nu = 0.023Re^{0.8}Pr^{0.3} \quad (3-12)$$

This correlation gives a Nusselt number estimate of 294. Accordingly, the forced-convection heat transfer coefficient, h_w , is:

$$h_w = \frac{Nuk_w}{2r_{f,1}} \quad (3-13)$$

$$h_w = 2,303 \text{ W/m}^2\text{K}$$

The natural-convection heat transfer coefficient, h_a , on the outer surface of the BFJA is fundamentally governed by the Rayleigh number, Ra (Cengel, 2004):

$$Ra = \frac{g\beta(T_{f,2} - T_a)(2r_{f,2})^3}{\nu^2} Pr \quad (3-14)$$

where g is the gravitational acceleration; β is the coefficient of volume expansion; and ν is the kinematic viscosity of air. The Nusselt number based on h_a is a function of Ra and Pr . The Nu correlation that is deemed suitable for natural convection over a heated sphere is given as (Cengel, 2004):

$$Nu = \left\{ 0.6 + \frac{0.589Ra^{1/4}}{\left[1 + (0.469/Pr)^{9/16}\right]^{4/9}} \right\}^2 \quad (3-15)$$

Once Nu is estimated from this expression, the natural-convection heat transfer coefficient, h_a , is determined as follows:

$$h_a = \frac{Nuk_a}{2r_{f,2}} \quad (3-16)$$

To determine the Nusselt number and hence h_a , the value of the Rayleigh number, Ra , is required. It is evident from Equation 3-14 that the value of $T_{f,2}$ is needed to establish the

value of Ra . In turn, the value of $T_{f,2}$ is dependent on the value of h_a as per Equations 3-5 to 3-8. Therefore, to solve for $T_{f,2}$ and h_a , and thereby the thermal resistance network for the BFJA, requires an iterative solution of Equations 3-5, 3-6, 3-8, 3-14, 3-15 and 3-16. This iterative solution yields a Ra value of 6.2×10^7 and a Pr value of 0.706 for an ambient temperature, T_a , of 15°C and atmospheric pressure. These Ra and Pr values yield a Nusselt number estimate of 42. Accordingly, the value of h_a is determined to be $6.28 \text{ W/m}^2\text{K}$.

Furthermore, this iterative solution yields a heat loss, Q_{loss} , equal to 220 W for a total thermal resistance, R_{tot} , equal to 1.11 K/W . This heat loss corresponds to the surface temperatures, $T_{f,1}$ and $T_{f,2}$, of 255°C and 242°C , respectively. These surface temperatures are applied on the inner and outer surfaces of the computational model of the BFJA in the third load step to simulate the temperature gradients across the BFJA.

3.8 Heat Transfer Analysis for the GCC

Similar to the BFJA, the complex geometry of the GCC does not allow direct prediction of heat transfer from the outer surfaces of the GCC using conventional heat transfer correlations. Accordingly, the GCC is also simplified to a thermal sphere to approximately assess the surface temperatures expected in service. This thermal sphere and its associated thermal resistance network for the GCC are illustrated in Figure 3-23. The thermal sphere circumscribes the GCC reasonably well; the inner and outer surface areas of the thermal sphere respectively match the inner and outer surface areas of the original geometry.

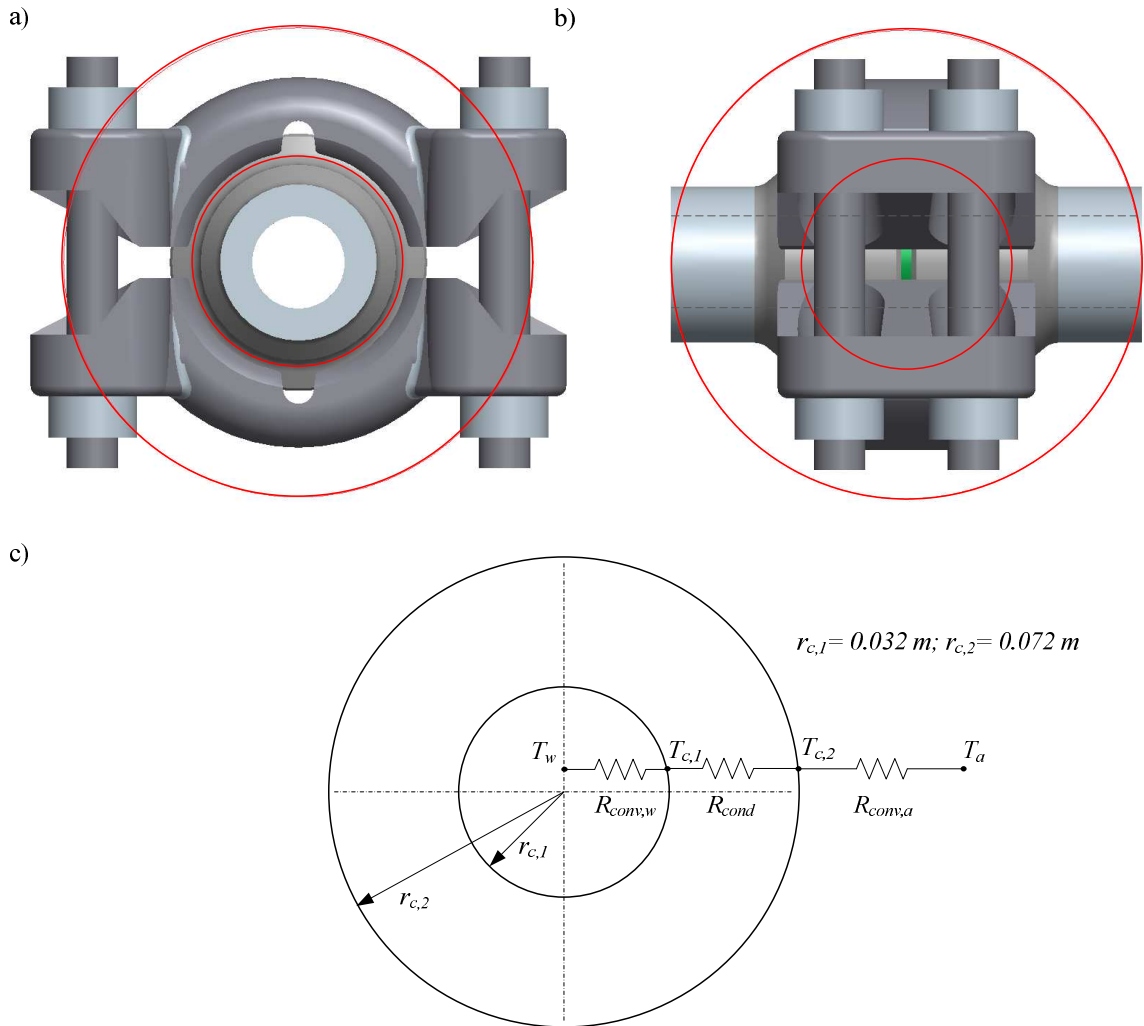


Figure 3-23: Simplified GCC geometry for heat transfer analysis a) superimposed on the geometric model; b) shown with the thermal resistance network.

Since the fluid-thermal model of the GCC is identical to that of the BFJA, the thermal analysis presented in Section 3.7 is repeated for the GCC, yielding inner and outer surface temperatures, $T_{c,1}$ and $T_{c,2}$, of $570 \text{ }^\circ\text{C}$ and $555 \text{ }^\circ\text{C}$, respectively. The surface temperatures, $T_{c,1}$ and $T_{c,2}$ are applied on the respective surfaces of the computational model of the GCC in the third load step to simulate the temperature gradients across the GCC for the fluid-thermal model.

The surface-thermal model assumes that the inner surface temperature, $T_{c,1}$, of the GCC is equal to the heated-surface temperature at the exit of the test section for a bulk-fluid temperature of 600°C. The heat transfer from the inner surface of the GCC to the ambient is then resisted by the conductive and convective thermal resistances in series, yielding a total resistance of:

$$R_{tot} = R_{cond} + R_{conv,a} \quad (3-18)$$

where R_{tot} is the total thermal resistance to the radial heat flow, and is given as (Cengel, 2004):

$$R_{tot} = \frac{r_{c,2} - r_{c,1}}{4\pi r_{c,2} r_{c,1} k_c} + \frac{1}{4\pi (r_{c,2})^2 h_a} \quad (3-19)$$

where k_c is the thermal conductivity of the hub, the clamp and the bolt material. The heat loss can then be estimated using the following relation (Cengel, 2004):

$$Q_{loss} = \frac{T_{c,1} - T_a}{R_{tot}} \quad (3-20)$$

Once Q_{loss} is determined from Equation 3-20, $T_{c,2}$ can be determined using:

$$Q_{loss} = \frac{T_{c,2} - T_a}{R_{conv,a}} \quad (3-21)$$

where $T_{c,2}$ is the outer surface temperature.

With $T_{c,1}$ and $T_{c,2}$ as thermal boundary conditions, the thermal stresses in the GCC can be determined. In order to quantify the total thermal resistance, R_{tot} , $T_{c,1}$ and h_a need to be determined. These steps are described next.

3.8.1 Determination of the Surface Temperatures

The inner surface temperature of the GCC, $T_{c,1}$, is taken as the exit surface temperature of the test section and can be estimated by applying an energy balance across the length of the test section. The rate of heat flow required to heat the working fluid from an inlet bulk-fluid temperature, T_i , of 260°C, to an exit bulk-fluid temperature, T_e , of 600°C is given as:

$$Q = \dot{m}c_p(T_e - T_i) \quad (3-22)$$

where \dot{m} is the maximum mass flow rate equal to 1.038 kg/s (Balouch, 2011). This rate of heat flow, Q , is equal to the heating power supplied by the electrically-heated surface of the tubular test section to the working fluid through convection:

$$Q = h_w A_s (T_{c,1} - T_e) \quad (3-23)$$

where A_s is the surface area exposed to the working fluid. The forced-convection heat transfer coefficient, h_w , in Equation 3-23 is determined using the same steps as in Section 3.7.1 by first evaluating the Reynolds number as:

$$Re = \frac{\dot{m}(2r_{c,1})}{\mu A_c} \quad (3-24)$$

The suitable Nusselt number correlation for estimating h_w , for a Re value of 1.3×10^5 and a Pr value of 0.873, is given as (Pioro *et al.*, 2004):

$$Nu = 0.0243Re^{0.8}Pr^{0.3} \quad (3-25)$$

Accordingly, the forced-convection heat transfer coefficient, h_w , is determined as follows:

$$h_w = \frac{Nu \cdot k_w}{2r_{c,1}} \quad (3-26)$$

$$h_w = 1,348 \text{ W/m}^2\text{K}$$

From Equation 3-22, the heat flow rate, Q , is determined to be 261 kW . This heat flow is used in Equation 3-23, to evaluate the inner surface temperature, $T_{c,1}$, as 1043°C .

The surface temperature, $T_{c,2}$, and the natural-convection heat transfer coefficient, h_a , are determined using the same iterative-solution technique as in Section 3.7.1 using the same equations. The iterative solution yields a Ra value of 7.2×10^6 and a Pr value of 0.694. These Ra and Pr values yield a Nusselt number estimate of 25.5. Accordingly, h_a is determined to be $8.70 \text{ W/m}^2\text{K}$.

Furthermore, this iterative solution yields a rate of radial heat flow, Q_{loss} , of 552 W for a total thermal resistance, R_{tot} , of 1.86 K/W . This rate of heat loss corresponds to the surface temperature, $T_{c,2}$, of 990°C . The surface temperatures, $T_{c,1}$ and $T_{c,2}$ are applied on the inner and outer surfaces, respectively, of the computational model of the GCC in the third load step to simulate the temperature gradients across the GCC for the surface-thermal model.

3.9 Solution of the Finite Element Equations

The finite element simulations performed for the BFJA and the GCC are static simulations, i.e. dynamic effects are neglected. The BFJA finite element simulation is rate-dependent, because the non-linear behaviour of the gasket is dependent on the rate of loading. All other components of the BFJA are insensitive to the rate of loading. The

GCC finite element simulation is rate-independent as all components of the GCC are insensitive to the rate of loading.

The BFJA was loaded gradually in small increments of the loading step i.e. in sub-steps. Through repeated test-runs of the finite simulation of the BFJA, 40 sub-steps for the first load step were found to adequately capture the non-linear behaviour of the gasket. The second and third loading steps were divided into 10 and 40 sub-steps, respectively.

The GCC was loaded similar to the BFJA for consistency between the finite element simulations of both assemblies.

The global system of finite element equations was solved using a Newton-Raphson iterative solver. The convergence criterion was based on the equilibrium of forces as the algorithm aimed at minimizing force imbalances. This force imbalance was reported by ANSYS[®] as a residual force. For the present work, the convergence criterion for the residual force was set at 0.1 percent of the forces applied at each sub-step. For instance, for an initial bolt preload of 55,000 N applied on the BFJA in the first load step, the convergence criterion was set at 55 N. Since the load step was divided into 40 sub-steps, the force acting on the BFJA was 1375 N at each sub-step and hence the convergence criterion was 1.375 N at each sub-step. Therefore, when the residual force went below 1.375 N, convergence was achieved. Similarly, on application of the internal pressure and temperature gradients, the system modified the convergence criterion to 0.1 percent of the resultant forces and convergence of the solution was achieved based on this updated convergence criterion.

The computational platform used for the present simulations was 8-cores of an Intel[®] Core[™] i7-2600 CPU with a 3.40 GHz clock speed. The typical CPU time taken for solving the computational model of the BJFA for all three external loads using 8-cores in parallel was 110 minutes. The typical CPU time taken for solving the computational model of the GCC for all three external loads using 8-cores in parallel was 449 minutes.

Chapter 4: Results and Discussion—Bolted Flange Joint Assembly (BFJA)

The finite element analysis (FEA) was performed to investigate the performance of the bolted flange joint assembly (BFJA) under the effects of temperature gradients. The BFJA was subjected to the external loads of initial bolt preload, internal pressure and thermal loadings in separate load steps to investigate their incremental effect on the BFJA. Four cases of finite element simulations were run to investigate the optimum bolt preload; flange rotation and gasket stresses to determine leakage integrity; and von Mises stresses in the flange and the bolt to determine structural integrity.

4.1 Validation of the BFJA Computational Model

Validation of the present FEA setup was performed by generating the gasket stresses for a 6-bolt BFJA that was investigated by Krishna *et al.* (2007). Krishna *et al.* modelled a quarter model of this BFJA for an initial bolt preload of 30,000 N at room temperature. A BFJA computational model, identical in geometry and constraints to that developed by Krishna *et al.* (2007) was developed using the techniques described in Chapter 3.

The p-c curve employed for validation was different from the one employed by Krishna *et al.* (2007) in his study. The p-c curve used by Krishna *et al.* (2007) was developed at room temperature. To account for some thermal degradation, a p-c curve developed by conducting a load compression mechanical test (LCMT) at a temperature of 100°C

(ANSYS Inc., 2010) was used in the present validation study and for the CSCW loop application discussed in later sections of this chapter.

The gasket stresses obtained from the validation study are compared to the results of Krishna *et al.* (2007) in Figure 4-1. The position of 50.80 mm represents the inner radius of the gasket, while the position of 60.35 mm represents the outer radius. The trends are

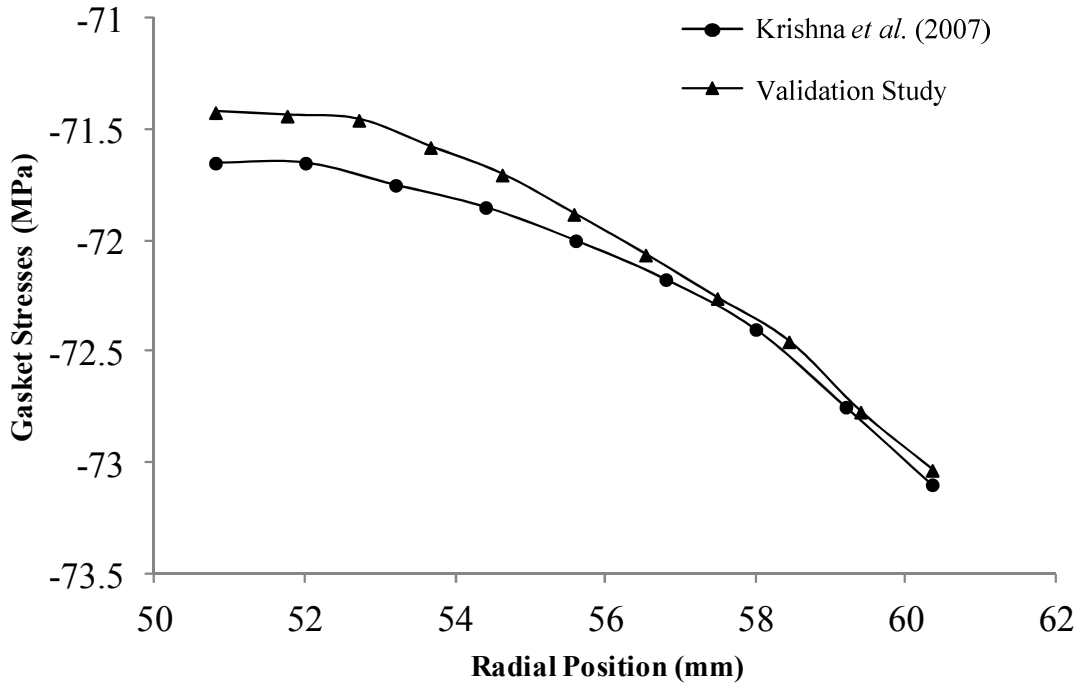


Figure 4-1: Stress distribution in the gasket.

noted to be similar for the two cases, with the stresses in the gasket increasing with closer proximity to the bolts. The small differences in the two sets of results are attributed to the differences in the p-c curve used for the respective studies. This favorable comparison is taken as an indication that the current computational model is set up correctly.

4.2 Simulation Test Matrix

The external load combinations considered for the present BFJA simulations are given in Table 4-1. An initial bolt preload, F_p , of 60,000 N was calculated using ASME design rules for flanged connections (ASME, 2010d). This initial bolt preload was used in the determination of the optimum bolt preload for the BFJA (Case 1 in Table 4-1). The deformation in the gasket generated due to this initial bolt preload was noted. The initial bolt preload was then reduced in increments of 1,000 N and the resultant changes in gasket deformation were evaluated for each incremental bolt-preload reduction. This process was continued until the desired gasket deformation (discussed in Section 4.3) was achieved and the corresponding bolt preload was taken as the optimum bolt preload.

Table 4-1: Test Matrix for the BFJA

External Loading		Case 1	Case 2	Case 3	Case 4
Bolt Preload (N)		60,000-55,000	55,000	55,000	55,000
Internal Pressure (MPa)		-	27	27	27
Surface Temperature (°C)	Inside	15	15	257	257
	Outside	15	15	257	242

The optimum bolt preload evaluated in Case 1 was then used in Cases 2, 3 and 4 for further investigation of the BFJA. In these simulation cases, an initial bolt preload of 55,000 N was applied in the first load step. An internal pressure of 27 MPa was applied in the second load step. Thermal loadings were applied in the form of inner and outer surface temperatures on the BFJA in the third load step. Cases 1 and 2 represent a BFJA operating at room temperature. Case 3 represents a BFJA that is perfectly thermally

insulated from the ambient conditions, thus all components of the BFJA reach the same elevated temperature as the inner surface temperature on the BFJA. In this case, no temperature gradients are generated across the BFJA. Case 4 represents the surface temperatures evaluated from the fluid-thermal model (Section 3.7) corresponding to the conditions expected on the CSCW loop. This systematic approach of introducing the loads enabled the analysis of the incremental effect of each of the three external loads on the components of the BFJA.

4.3 Optimum Bolt Preload

The initial bolt preload applied on the BFJA is required for seating the gasket on the faces of the flanges. The residual bolt preload is required to maintain sufficient gasket stresses for leakage integrity, after the internal pressure and the thermal load are applied on the BFJA. Moreover, the residual bolt preload should account for relaxation occurring due to creeping of the gasket over time. The BFJA will experience the pressure and thermal loads on the CSCW loop for periods that are much shorter than the duration of the bolt preload. Once the CSCW loop is assembled with the BFJA bolts installed as per their intended preload values, these preload levels will remain until the BFJA is disassembled. Yet, the pressure and temperature loads on the BFJA will only be present when the CSCW loop is operated for a few hours at a time during experiments. Accordingly, the creep of the gasket will mostly occur when the loop is not in operation. Jenco and Hunt (2000) suggested that the relaxation and creep in the gasket could be minimized by creating a hard-joint on the BFJA. Since the initial bolt preload is present over the entire

installed-life of the CSCW loop, it is most advantageous to evaluate an initial bolt preload that will develop the hard-joint condition.

Typically, the winding on a spiral-wound gasket is thicker in the axial direction than the thicknesses of the inner and outer rings, so that it can be compressed to conform to the faces on the flanges. If the gasket is compressed completely to this additional axial-thickness of the winding, the gasket no longer has the ability to deform in any way. This is the hard-joint condition where the gasket creep is minimized since the gasket is fully deformed. Accordingly, the initial bolt preload required to compress the gasket into a hard-joint is taken as the optimum bolt preload.

The total additional axial-thickness of the winding, at room temperature, is 0.031 mm for the spiral-wound gasket used on the CSCW loop. As per Case 1 in Table 4-1, an initial bolt preload of 60,000 N, equivalent to the ASME design bolt preload, was applied on the BFJA. The compression in the gasket was noted to be 0.033 mm. The simulation was repeated by incrementally decreasing the bolt preload by 1,000 N until a compression of 0.031 mm was achieved for a bolt preload of 55,000 N. Hence, 55,000 N was taken as the optimum bolt preload to achieve a hard-joint on the BFJA.

4.4 Deformation Terminology of the BFJA

The deformation behaviour in the radial-plane of the flange-ring on the BFJA is illustrated schematically in Figure 4-2. The total axial displacement of the flange is split into two components: the rotational axial displacement, D_{rot} (Figure 4-2a); and the pure axial displacement of the flange, D_{axi} (Figure 4-2b). The rotational axial

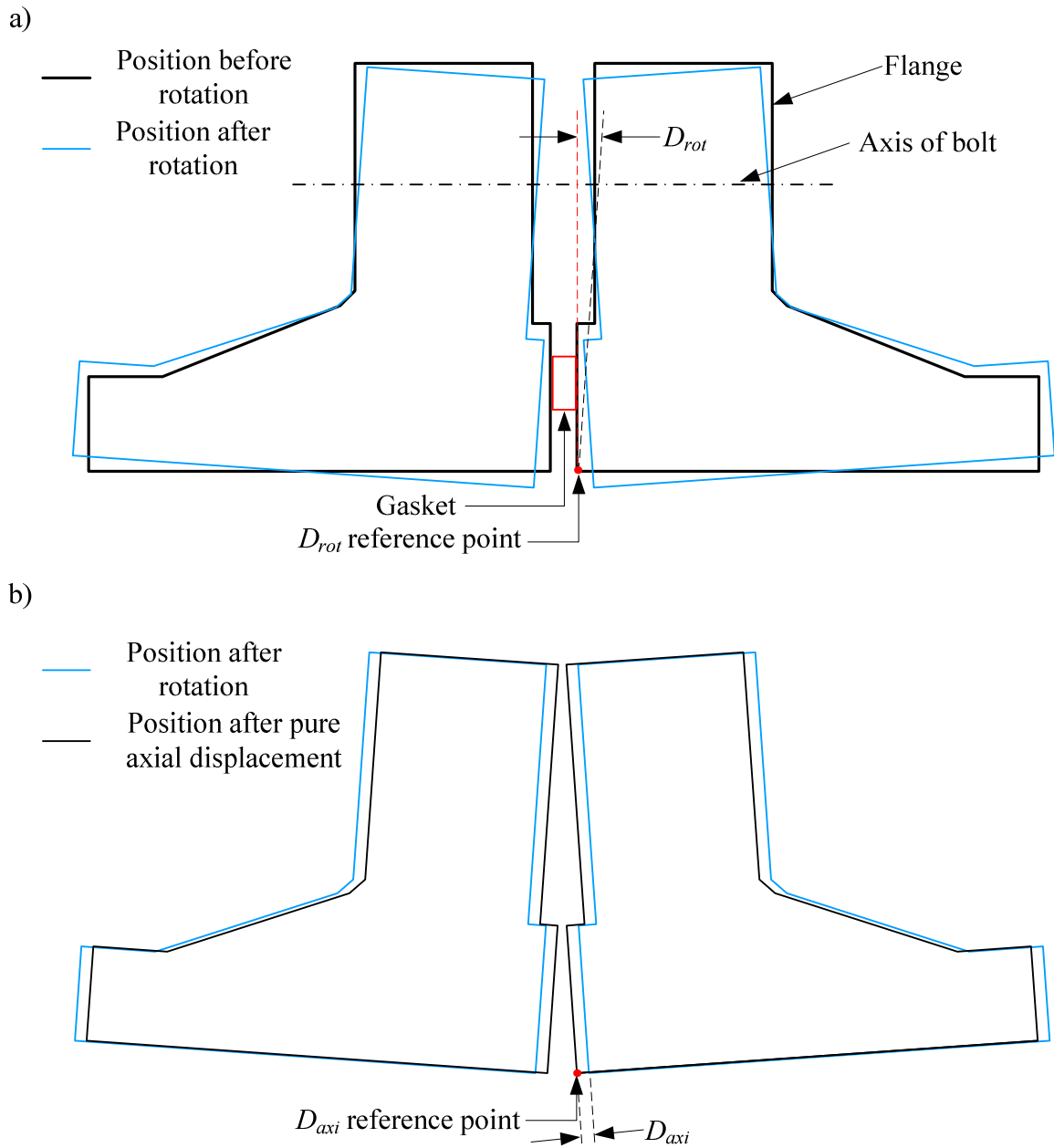


Figure 4-2: Deformation of the flange-ring a) rotational axial displacement, D_{rot} ; b) pure axial displacement, D_{axi} . The amount of deformation is exaggerated for illustration.

displacement, D_{rot} , is measured at the raised-face of the flange-ring, relative to the undeformed inner surface, as illustrated in Figure 4-2a. The rotational deformation of the flange yields a negative D_{rot} value thus pulling the two flange-rings toward each other at

the location of the bolt, while pulling them away closer to the inner edge of the flange-rings, with the gasket serving as the pivot point. Given that this rotational deformation promotes an uneven contact of the gasket with the flange faces, D_{rot} is detrimental to the leakage-integrity of the BFJA. The pure axial displacement, D_{axi} , is the axial displacement of the flange at the inner surface. The difference between the total axial displacement and D_{axi} measured along the radial-width of the flange is equal to D_{rot} . D_{axi} is responsible for evenly compressing the gasket and compensating for the lopsided contact of the gasket with the flange due to the rotational deformation, D_{rot} .

The true deformation of the flange for Case 4 is shown in Figure 4-3 to illustrate the

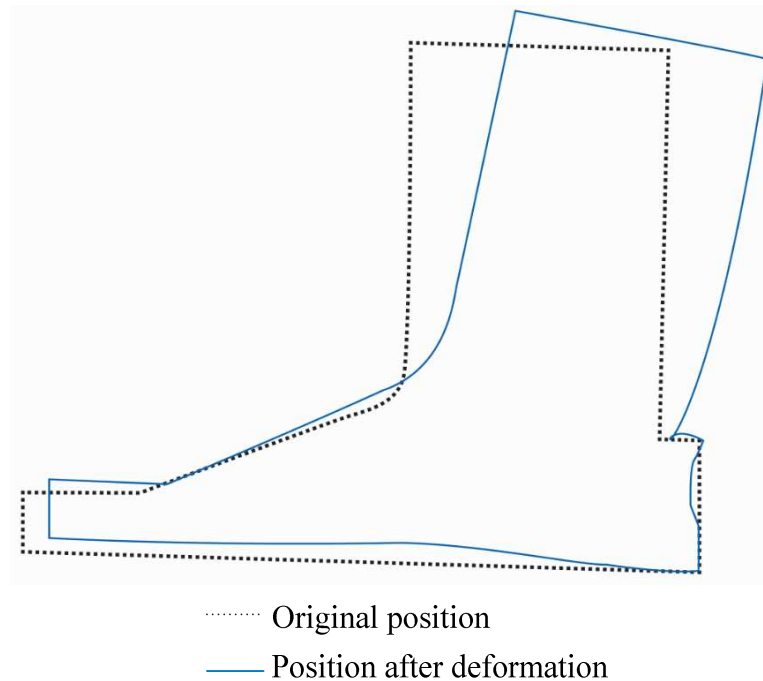


Figure 4-3: Computed deformation of the flange under the combined effects of initial bolt preload, internal pressure and spatially-nonuniform elevated temperature. The amount of expansion has been amplified by 500 times for the purpose of effective illustration.

suitability of the choice of deformation parameters D_{rot} and D_{axi} for studying the deformation of this flange.

4.5 Flange Rotation

Flange rotation is one of the factors affecting the leakage integrity of a BFJA. It is the deformation of the flange in the radial and circumferential directions. The radial deformation is due to the rotation of the flange in the radial plane about a pivot point that is located on the gasket. The position of the pivot point on the gasket depends on the direction of the external load acting on the flanges and the deformed shape of the gasket and therefore shifts as each incremental load is applied.

The circumferential deformation on the BFJA is best illustrated by “unfolding” the flange-ring into a horizontal plate, as illustrated in Figure 4-4. As the initial bolt preload is applied, the bolts pull the flange-rings toward each other. The circumferential

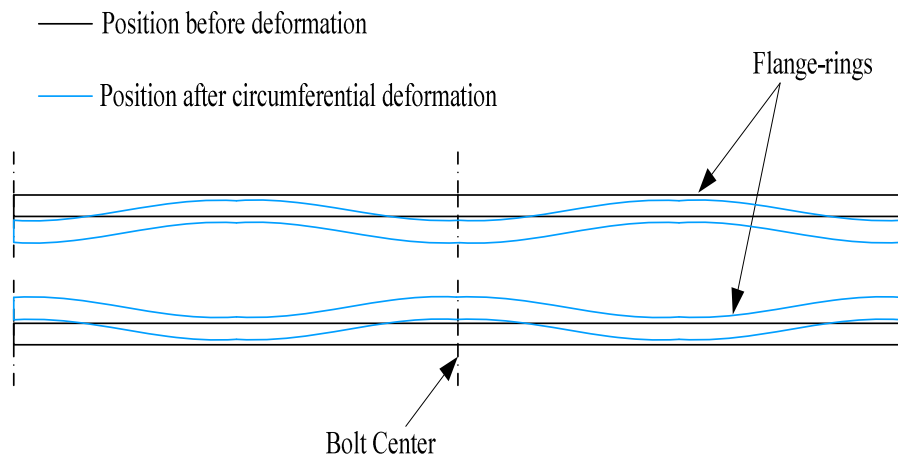


Figure 4-4: Circumferential deformation of the “unfolded” flange-ring of the BFJA. The amount of deformation is exaggerated for effective illustration.

deformation of the flange-rings is greatest at the location of the bolts and decreases towards the mid-plane between two adjacent bolts. For typical spacing of bolts along the circumference of the flange and the amount of bolt preload applied, the axial displacement at the mid-plane is negligibly small. Unlike the radial deformation, the circumferential deformation does not have a tangible pivot point. By considering the minimum-displacement location as a pivot point, the circumferential deformation can also be viewed as a circumferential rotation about the mid-plane similar to that illustrated for the radial rotation in Figure 4-2.

Radial flange rotation is largest in the radial plane of the flange that coincides with the radial plane of the bolts. Since the bolt preload causes the highest compression of the gasket in this radial plane, it is termed the high-stress gasket plane, and is illustrated in Figure 4-5 with red lines. D_{axi} and D_{rot} are highest in this plane. Similarly, the circumferential deformation is minimum in the mid-plane between two adjacent bolts. The gasket at this location experiences the least compression due to the circumferential

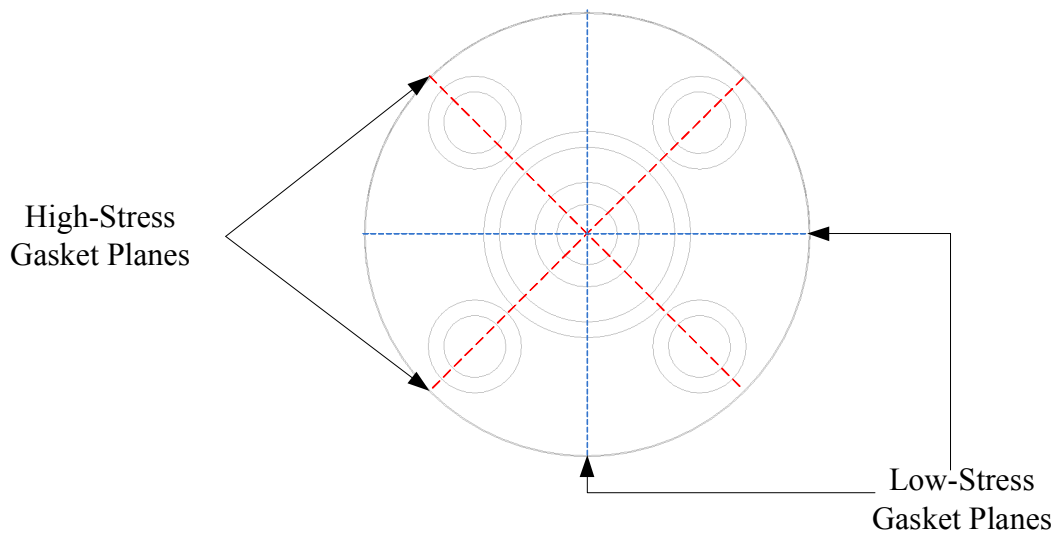


Figure 4-5: High-stress and low-stress radial planes on the gasket.

rotation. Moreover, the gasket at this location also experiences the least compression due to radial rotation. Accordingly, this mid-plane is termed the low-stress gasket plane, as illustrated in Figure 4-5 with blue lines. The low-stress gasket plane coincides with the symmetry plane of the computational model of the BFJA, shown in Figure 3-16 in Section 3.6.1. D_{axi} and D_{rot} are minimum in this plane. Given the importance of D_{axi} and D_{rot} to the sealing performance of the BFJA, the low-gasket stress plane is the most susceptible plane for leakage of the working fluid on the BFJA and is studied in further detail. The radial distributions of D_{rot} and D_{axi} in the low-stress gasket plane are shown for each of the three load steps in Figure 4-6a, as per loading Cases 1 to 4 in Table 5-1.

By definition, D_{axi} is constant along the radial width of the flange for each of the three load steps. The region defined by r/R_f values of 0 to 0.12 corresponds to the location where the overall axial length of the flange is the largest (Section 3.1). Here, $r=0$ corresponds to the inner diameter of the flange. This results in high stiffness of the flange to rotational deformation in this region, to the extent of yielding negligible values of D_{rot} . Since D_{rot} is negligible in this region, D_{axi} represents the overall axial displacement effect of the BFJA on the CSCW loop. D_{axi} is maximum for the initial bolt preload and is reduced when the internal pressure and the thermal loadings are applied. This reduction in D_{axi} is the axial displacement of the BFJA occurring on the CSCW loop during operation. The negative increment in D_{axi} due to pressure loading (Case 2) causes the flanges to be pulled apart increasing the tension in the bolts. Specifically, the residual bolt preload is increased by 16% from Case 1 to Case 2. The negative increment in D_{axi} due to elevation of temperature (Case 3) does not affect the gasket since this does not induce any changes in the bolt tension. This is because the axial portions of the bolts

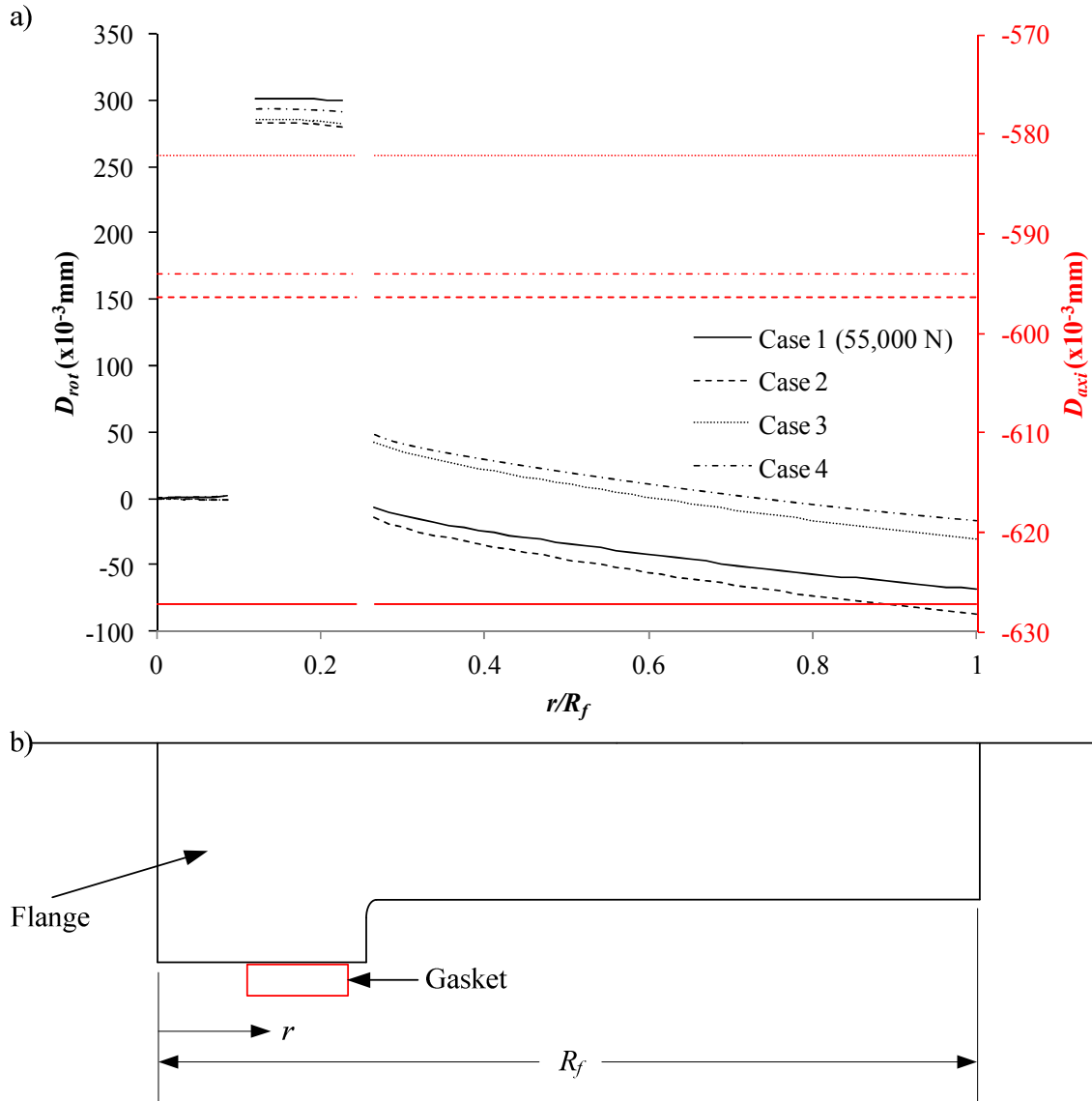


Figure 4-6: Radial flange rotation at the low-stress gasket plane for Cases 1 to 4. Note: The y-axis ranges for D_{rot} and D_{axi} are not the same to allow for effective visualization of the trends in these two parameters.

corresponding to the axial thickness of the flanges axially expand by the same amount as the flanges due to the thermal expansion coefficients having the same values for these two components. The axial portion of the bolts corresponding to the thickness of the gasket axially expands by a lesser amount compared to the gasket due to the difference in

the thermal expansion coefficients of these two components. This increases the residual bolt preload by 0.7% and affects D_{rot} as explained later in the text.

In Case 4, the portion of the flange at lower radii reaches higher temperatures than the flange segment and the bolts situated farther out in the radial direction. This prompts the flange segment at lower radii to axially expand by a larger amount than the flange segment at larger radii and the bolts. This differential expansion results in the D_{axi} increment between Case 3 and Case 4, shown in Figure 4-6. This effect, combined with the larger relative expansion of the gasket compared to the bolt segment spanning the gap between the two flanges (due to difference in temperature as well as thermal expansion coefficients of the gasket and the bolts), prompts an increase in D_{rot} as seen in the figure. The results of these deformations is a 1.8% increase in the residual bolt preload for Case 4 compared to Case 3. While the magnitude of D_{rot} changes with each incremental load, the largest contribution comes from the initial bolt preload. D_{rot} is negligible for the region on the flange where r/R_f increases from zero to 0.12 since, as noted earlier, the geometry of the flange results in notably increased stiffness to radial deformation in this region. Over the range of r/R_f values 0.12 to 0.24, the flange is in contact with the gasket, and thus the increment in D_{rot} is equivalent to the deformation/closure occurring in the gasket. Internal pressure acting on the flange, as per Case 2, generates a net moment on the flange about the gasket contact point that pushes the flanges together at the location of the bolts, which slightly increases the degree of rotation of the flange. This rotation would tend to reduce the tensile force in the bolts. However, the increment of D_{axi} , due to the axial component of internal pressure tending to pull the two flanges away from each other, generates an increase in tension in the bolts that is much greater in

magnitude than the reduction in tension that would result from the decrease in D_{rot} . Accordingly, the net effect of internal pressure is an increase in the tensile stress in the bolts, as indicated earlier by the rise in residual bolt preload. This effect of internal pressure concurs with similar investigations in published literature (Krishna *et al.*, 2007; Mathan and Prasad, 2009).

When the temperature of the BFJA is elevated in a spatially-uniform manner, as per Case 3, there is a notable positive increment in the rotational deformation, D_{rot} , for r/R_f values greater than 0.24. The increased stiffness of the gasket at elevated temperature makes it more difficult to rotate the flange for the same residual bolt preload.

The increase in flange rotation can be reduced by using a wider gasket. However, a wider gasket will require a greater initial bolt preload to sufficiently compress the gasket; an increase in bolt preload increases the chances of crushing the segment of the gasket in close proximity to the bolt. Therefore, a compromise has to be made between a higher flange rotation and a higher bolt preload. For the present application, due to the high internal pressure that increases the residual bolt preload significantly, preference has been given to a lower initial bolt preload and therefore a smaller width gasket has been employed.

4.6 Leakage Integrity of the BFJA

In practice, the gasket is seated into the imperfections of the flange face to achieve sealing on the BFJA. Therefore, sufficient gasket stresses should be generated to conform the gasket to the flange face and not allow leakage of the working fluid. The minimum-

seating gasket stresses are those required to seat the gasket on the flange under the initial bolt preload. The minimum operating gasket stresses are those required to maintain sufficient compression on the gasket for leakage integrity when subjected to the residual bolt preload and other external loads. The ASME design rules (ASME, 2010d) define the minimum operating gasket stresses, when the residual bolt preload and the internal pressure are acting on the BFJA as:

$$\sigma_{g,o} = mP \quad (4-1)$$

where m is the gasket maintenance factor, and P is the internal pressure. The gasket maintenance factor represents the difference between the seating stresses and the operating stresses. For a spiral-wound gasket this factor is typically taken to be 3. Accordingly, for the design pressure of 27 MPa, $\sigma_{g,o}$ is equal to 81 MPa. Equation 4-1 is defined by two parameters, both of which are a function of the internal pressure. Therefore, Equation 4-1 remains valid even after imposing the temperature gradients on the BFJA, and the gasket stresses must satisfy the equation to offset the influence of internal pressure. However, this equation does not provide any indication if the gasket stresses are sufficient for the temperature gradients that are applied on the BFJA. Therefore, the minimum gasket stresses required under imposed temperature gradients cannot be ascertained using this equation.

Leakage integrity of the gasket was investigated by subjecting the BFJA to external loadings as per Cases 1 to 4 in Table 4-1 to evaluate the stresses of the gasket, as illustrated in Figure 4-7. The average gasket stresses generated for Cases 1 and 2 satisfy the minimum-seating and minimum-operating gasket stresses. When internal pressure is

applied, as per Case 2, the axial component of pressure tries to pull the two flanges apart, which causes a decrease in the gasket stresses. Nonetheless, these stresses are

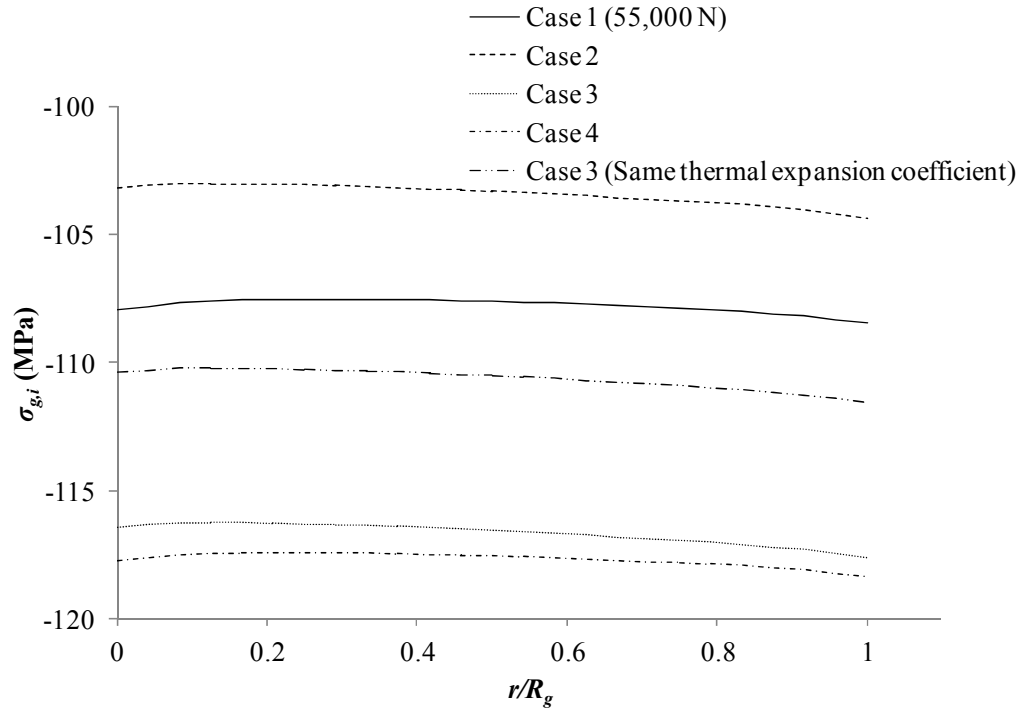


Figure 4-7: Gasket stresses across the radial-width of the gasket.

significantly high to account for additional factors such as vibration that may be encountered during the operation of the CSCW loop.

The average stresses in the gasket increase for Case 3 and Case 4 by 13% and 14%, respectively. However, the increase in residual bolt preload is only 0.7% and 1.8% for Case 3 and Case 4, respectively. To isolate the primary effect responsible for this increase in the gasket stresses which notably exceeds the increment due to the residual bolt preload, the finite-element simulation for Case 3 was repeated by employing the same coefficient of thermal expansion for the gasket as the flange and the bolt. By doing so, the thermal expansion at the uniform elevated temperature would be uniform for all

components of the BFJA and there would be no relative deformation between components to generate an increase in the gasket stresses. However, Figure 4-7 indicates that even for this case, the average gasket stresses increase to 110 MPa. This behaviour is attributed to the increase in the elastic modulus with temperature for the gasket material. An increase in the elastic modulus for the same strain would generate an increase in the gasket stresses according to the constitutive equation (Section 2.1.2) for materials. Therefore, the combined effect of the increased elastic modulus and the higher coefficient of thermal expansion for the gasket is responsible for the increase in the gasket stresses for Cases 3 and 4.

4.7 Structural Integrity of the BFJA

This section investigates the stresses generated within the flange and the bolt under thermal loadings on the BFJA, within the context of the allowable stress limits set by ASME (2010c; 2010d). These stresses are presented in terms of the von Mises stresses, commonly used as a failure criterion (ASME, 2010d). The von Mises stresses are calculated based on the principal stresses in three dimensions and therefore are representative of the three-dimensional stress field.

To investigate the structural integrity of the flange and the bolt, the BJFA was loaded as per Cases 2, 3 and 4 in Table 4-1. For Case 2, the primary von Mises stresses generated must remain within the following primary stress limit (ASME, 2010d):

$$\sigma_{p,a} = S_C \quad (4-1)$$

where S_C is the allowable stress of the component material at room temperature (ASME, 2010d). Upon subjecting the BFJA to the thermal loadings as per Cases 3 and 4, the secondary von Mises stresses generated must remain within the following secondary stress limit:

$$\sigma_{s,a} = f(1.25S_C + 0.25S_H) \quad (4-2)$$

where f is a stress range factor, and S_H is the allowable stress of the component material at the elevated temperature (ASME, 2008). f is equal to 1.2 for the elevated temperature of 260°C that is expected for the BFJA during operation of the CSCW loop. Table 4-2 lists the allowable stresses for the flange and the bolt material.

Table 4-2: Allowable stresses for the flange and the bolt at room temperature and elevated temperature of 260°C (ASME, 2010c).

	Flange	Bolt
S_C (MPa)	138	130
S_H (MPa)	125	89
$\sigma_{p,a}$ (MPa)	138	130
$\sigma_{s,a}$ (MPa)	244	222

4.7.1 Stress Distribution in the Flange

The effect of thermal loading on the flange was investigated by comparing the stress distributions within the flange under the bolt preload and internal pressure with and without thermal loading. Specifically, the BFJA was subjected to external loadings as per

Cases 2, 3 and 4 to evaluate von Mises stresses in the flange, at room temperature, and for spatially-uniform and spatially-nonuniform thermal loadings, respectively. The von Mises stress contours for these three cases are plotted in Figure 4-8(a-c).

For Case 2, the average stress in the flange is comfortably within the allowable primary stress limit. Similarly, for Cases 3 and 4, the average stresses are comfortably within the allowable secondary stress limit. However, the maximum stresses marked in red, occurring at the junction of the flange-ring and the raised-face, exceed the allowable limits in all the three cases. Due to its geometric configuration, this junction behaves like

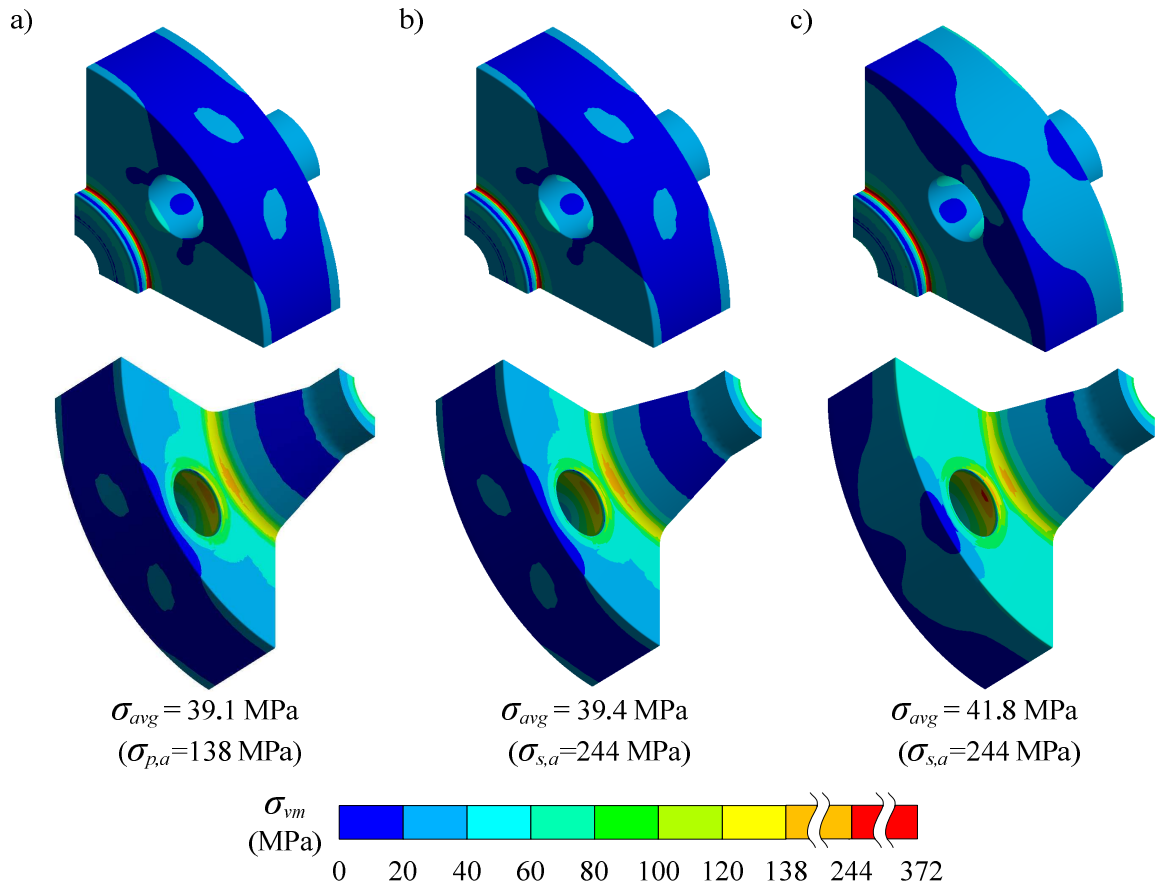


Figure 4-8: Von Mises stresses for the flange a) Case 2—room temperature; b) Case 3—uniform elevated temperature; c) Case 4—temperature gradients across the BFJA at elevated temperature.

a local structural discontinuity and therefore the stresses are high. However, as discussed in Section 3-3, the deformation at this location cannot be captured reliably due to divergence of the displacement function. Accordingly, the stresses at this location are termed singular stresses. Despite the unreliable nature of these stresses, the stresses are expected to be high at this location. Since the computed stresses are divergent in nature, they are an overestimation of the true stresses. As such, if these singular stresses meet the allowable stress requirement associated with the stress concentration, the true stresses at this location can be deemed safe as well. ASME provides a higher limit for the stresses at this location equivalent to $3\sigma_{p,a}$ and $3\sigma_{s,a}$, at room temperature and the elevated temperature, respectively. Accordingly, the stresses at this location are within the allowable stress concentration limits at this location. Moreover, high stresses in the flange occur at the flange-neck and in the bolt hole. Unlike the junction at the raised-face these geometric locations are accurately captured by the computational model developed for the BFJA. The stress intensification at the flange-neck is expected since it is a gross structural discontinuity. Similarly, high stresses exist in close proximity of the bolt-holes as the bolt preload is transferred to the flange through these localized regions.

The stress distributions on the flange for Cases 2 and 3 are seemingly identical. The flange and the bolt have the same coefficient of thermal expansion and therefore there is no relative thermal expansion between the two components. The gasket expands more than the flange and the bolt due to its higher thermal expansion coefficient. However, due to the relative small size of the gasket, its influence on the stresses on the flange is observed to be restricted to the segment of the raised-face of the flange it is in contact

with. Accordingly, the average stress in the flange increases only by 0.3 MPa or 0.8% from Case 2 to Case 3.

When the temperature gradients are imposed on the BFJA, as per Case 4, there is a 7% increase in the average stresses. Moreover, as illustrated in Figure 4-8c, the stresses increase on the flange-ring in the proximity of the bolt. This increase in stresses occurs due to the relative thermal expansion between the flange and the bolt since both components are at different average temperatures.

The average stress in the flange for Case 4 is much lower than the allowable limits. Accordingly, only temperature gradients across the BFJA that are significantly larger than the scenario considered for Case 4 will structurally fail the flange. However, the gasket will lose its leakage integrity before the flange fails. Therefore, the performance of the BFJA is driven by the performance of the gasket and structural integrity of the BFJA is ensured if the gasket maintains its leakage integrity under a given thermal load. In conclusion, the flange is deemed safe for operation under the external loadings, as per Cases 2 to 4.

4.7.2 Stress Distribution in the Bolt

Bolts are designed to operate under tension when preloaded. As the bolts pull the flanges together, the resistance offered by the flanges stretch the bolts. Moreover, the bolts bend toward the gasket in the radial direction. The effect of thermal loads on the bolts was investigated by evaluating the average von Mises stresses for the bolt, with and without the imposed thermal loads. Accordingly, the BFJA was subjected to external loadings as per Cases 2, 3 and 4 to evaluate von Mises stresses in the bolt, at room temperature, and

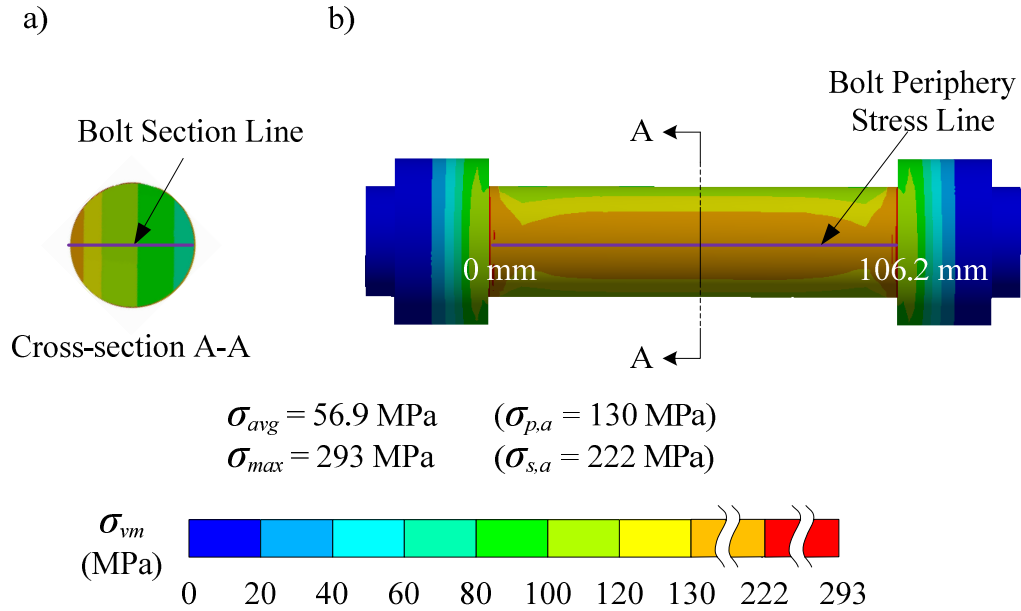


Figure 4-9: a) Bolt section stress; b) bolt periphery stress for spatially-nonuniform elevated temperatures across the BFJA, as per Case 4.

for spatially-uniform and spatially-nonuniform thermal loadings, respectively. The average von Mises stresses in the bolts for Cases 2, 3 and 4, were 55.8, 56.2 and 56.9 MPa, respectively. The stress distributions on the cross-section and the periphery of the bolt for Case 4, are illustrated in Figure 4-9a and b, respectively. The stresses vary from a maximum to a minimum from the peripheral location where the tensile force due to the bending of the bolt is highest, to the other end of the bolt section line, where bending of the bolt reduces the bolt tension locally. While the average stresses satisfy the allowable primary and secondary stress limits for Case 2, 3 and 4, the bolt exceeds the primary stress limit at the location of maximum stretching of the bolt (Figure 4-9b) for Case 4. To account for this tensile deformation, ASME (2010d) defines two safety parameters; the bolt section stress and the bolt periphery stress. The bolt section stress is the mean of the stresses on the bolt section line, shown in Figure 4-9a. The bolt section line is drawn at the section located at the mid-position of the bolt denoted by section A-A in Figure 4-9b.

The periphery bolt stress is determined by evaluating the mean stress along the periphery line, as illustrated in Figure 4-9b, where maximum stretching of the bolt occurs under operation. The allowable bolt section stress and bolt periphery stress are given by ASME as $2S_H$ and $3S_H$, respectively (ASME, 2010c; ASME, 2010d). ASME (2010d) dictates that the stress concentration occurring at the junction of the stud-bolt and nut are neglected when evaluating the periphery stress. Accordingly, the bolt section stress has a magnitude of 102, 103 and 104 MPa for Cases 2, 3 and 4, respectively. The bolt periphery stress has a magnitude of 131, 132 and 137 MPa for Cases 2, 3 and 4, respectively. Both the average bolt section stress and the periphery stress are within their respective allowable stress limits.

The junction between the stud-bolt and the nut behaves similar to a local structural discontinuity and therefore the stresses are intensified at that location. ASME provides a higher limit for the stresses at this location equivalent to $3\sigma_{p,a}$ and $3\sigma_{s,a}$, at room temperature and the elevated temperature, respectively. The maximum stress occurring at this junction for Cases 2, 3 and 4 lies comfortably within the allowable stress concentration limit. Therefore, the bolt is deemed structurally safe for the external loads expected on the CSCW loop.

Chapter 5: Results and Discussion—Grayloc[®] Clamp Connector (GCC)

The finite element analysis (FEA) was performed to investigate the performance of the Grayloc[®] clamp connector (GCC) under the effects of thermal loading. The GCC was subjected to the external loads of bolt preloading, internal pressure and thermal loading, where each external load was applied in separate load steps to investigate their incremental effect on the GCC. Five cases of finite element simulations were run to determine stresses in the seal-ring which affect the leakage integrity of the GCC, and the stresses in the hub, the clamp and the bolts to determine structural integrity. The simulations also examine the effect of lubrication applied on the interface surfaces between the hubs and the clamps on the load transfer between components and thereby the structural integrity of the GCC.

5.1 Simulation Test Matrix

The combinations of the external loads applied on the GCC for the present study are given in Table 5-1. Cases 1-5 of Table 5-1 were used to investigate the leakage integrity of the seal-ring and structural integrity of the hubs, clamps and the bolts. In these simulation cases, an initial bolt preload, F_p , of 6,000 N was applied in the first load step, which was calculated using ASME design rules for flanged connections (ASME, 2010d). An internal pressure of 27 MPa was applied in the second load step. Thermal loadings were applied in the form of inner and outer surface temperatures on the GCC in the third load step. Case 1 represents a GCC at room temperature. Case 2 represents a GCC that is

perfectly thermally insulated from the ambient conditions, thus all components of the GCC reach the same temperature as the inner surface temperature on the GCC. In this case, no temperature gradients are generated across the GCC. Cases 3 and 5 represent the surface temperatures evaluated from the fluid-thermal model and surface-thermal model (Section 3.8), respectively. Case 3 represents surface temperatures evaluated for the conditions expected on the CSCW loop. Case 4 extends this analysis from Case 3 to establish the limit of temperature gradients that can be imposed across the GCC without failure. Case 5 represents surface temperatures evaluated from the surface-thermal model developed in Section 4.8. Case 6 is used to study the effect of lubrication between the hub and the clamp on the structural integrity of the GCC. In this simulation case, the coefficient of friction used to model the friction contact between the hub and the clamp under the initial bolt preload was modified from 0.4 to 0.1. A coefficient of friction of 0.4 represents dry-contact while a value of 0.1 represents lubricated contact between the hub and the clamp interface. This simulation case was compared to Case 1 after the first load step, to isolate the effects of lubrication on the GCC.

Table 5-1: Test-Matrix for the GCC

External Loading	Case 1	Case 2	Case 3	Case 4	Case 5	Case 6
Bolt Preload (N)	6,000	6,000	6,000	6,000	6,000	6,000
Internal Pressure (MPa)	27	27	27	27	27	0.1
Surface Temperature (°C)	15	600	570	570	1043	15
	15	600	555	470	990	15
Coefficient of Friction	0.4					0.1

5.2 Deformation Behaviour of the Clamp

Case 1 in Table 5-1 is used to study the deformation behaviour of the clamps at room temperature, as illustrated schematically in Figure 5-1. Parts a and b of this figure illustrate the non-deformed and deformed position of the clamps, respectively. The clamp bends inwards toward the mid-position of the assembly as the initial bolt preload is applied on the GCC. This bending of the clamp is likened to the flange rotation on the

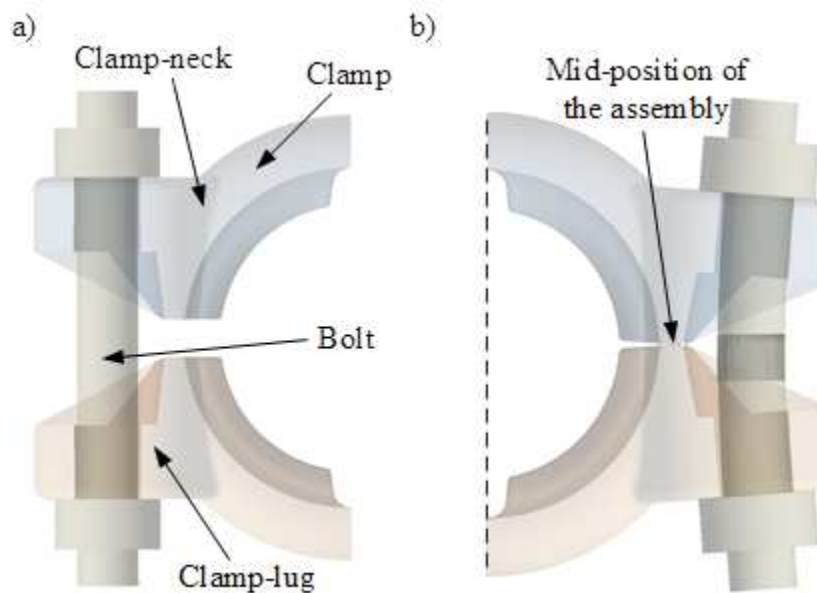


Figure 5-1: Schematic of the clamp and the bolt in the a) non-deformed position; b) deformed position under external loads at room temperature. The amount of deformation is exaggerated for clarity.

BFJA and is termed as ‘clamp’ rotation. This clamp rotation occurs about the mid-plane on the clamp marked by a dashed vertical line on Figure 5-1b. The strongest contact of the clamp with the hub occurs near the mid-position of the assembly. This mid-position is referred to later in Section 5.3.1. This rotation of the clamp locally reinforces the contact of the hub with the seal-ring. Grayloc[®] (2010a) suggests that this helps to energize the

seal-ring within the hub-recess when the internal pressure is applied. However, since this effect is localized, it does not reinforce the sealing at all points along the circumference. Accordingly, this local reinforcement does not ensure energizing of the seal-ring over its entire circumference. The clamp rotation needs to be limited to avoid high deformation in the clamp-neck. As will be seen from results of the finite-element simulations, the deformation behaviour of the GCC is primarily driven by the bolt preload. For the first load step, the initial bolt preload drives the deformation of the GCC. For the second and third load step, the residual bolt preload (modified initial bolt preload due to the internal pressure and thermal loading), drives the deformation of the GCC. Accordingly, the magnitude of the residual bolt preload best represents the influence of the other external loads on the GCC.

The loading occurring due to internal pressure, in addition to the initial bolt preload, can be resolved into two components: a uniform radial component that tries to pull the clamps apart, and simultaneously energizes the seal-ring through hoop stresses generated in the seal-ring; and a uniform axial component that tries to pull the hubs apart. Longitudinal and shear forces are generated in the bolts in response to these pressure loads causing an increase in the bolt preload. The radial component makes the clamp-neck most susceptible to deformation. To ensure efficient transmission of the external load to/from the clamp-lug, this deformation must remain within acceptable limits.

The deformation of the GCC when heated, as per Cases 2 and 3 in Table 5-1, is illustrated in terms of the clamp rotation in Figure 5-2a and b, respectively. Since the seal-ring has the lowest coefficient of thermal expansion amongst the component of the GCC, it expands by the least amount relative to the other components. Accordingly, the

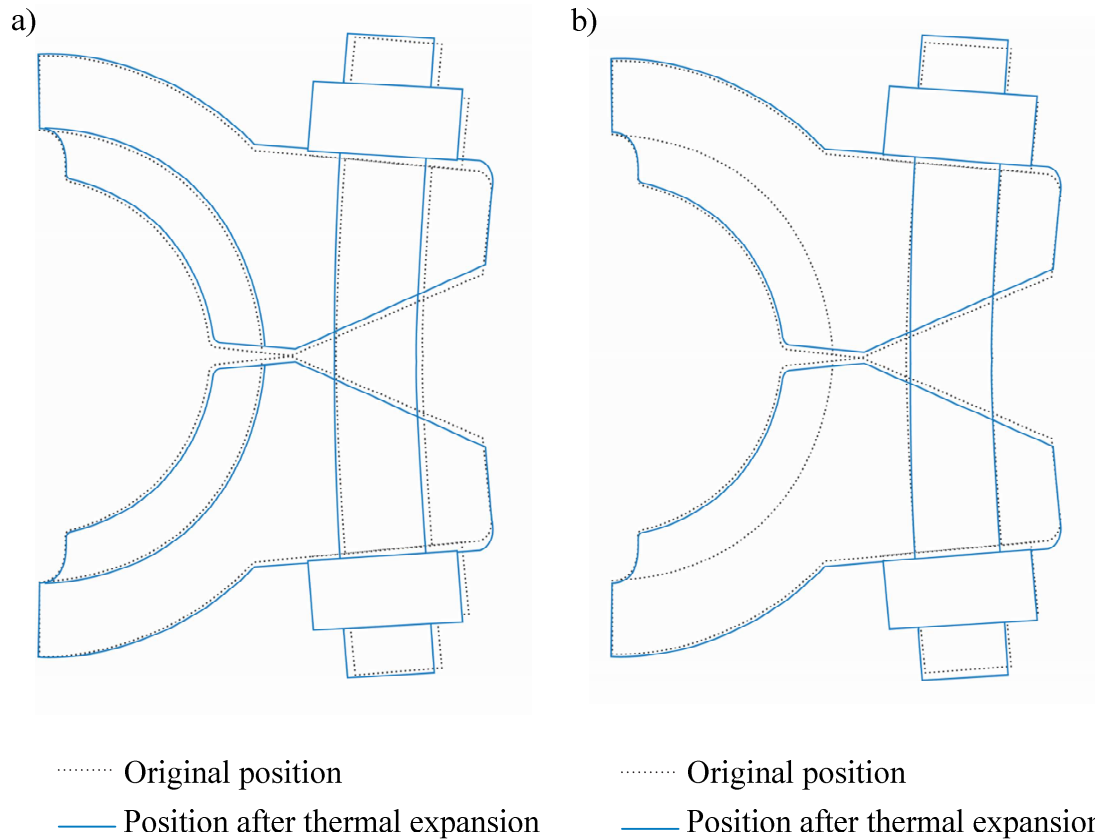


Figure 5-2: Clamp rotation when the GCC is subjected to a) Case 2--uniform elevated temperature; b) Case 3—temperature gradients across the GCC at elevated temperature. The amount of expansion has been amplified by 40 times for the purpose of clarity.

load exerted on the seal-ring by the hub, in both the radial and axial directions, is relaxed due to the relative thermal expansion between the two components. In turn, the contact force between the hub and the clamp is also reduced. Accordingly, the residual bolt preload is reduced by 10%, for spatially-uniform elevation of temperature, as per Case 2. Moreover, radial relaxation of the hub and the clamp in this case reduces the bending of the bolt and thereby the clamp rotation, as illustrated in Figure 5-2a. Since the hub, the clamp and the bolt have the same coefficient of thermal expansion, there is no relative expansion between these components.

For Case 3, however, the residual bolt preload increases by 1.4% compared to the bolt preload for Case 1. The reduction in the residual bolt preload due to elevation of temperature is more than offset by the increase in the residual bolt preload due to the temperature difference across the GCC. The deformation profile of the GCC follows the temperature profile imposed across the GCC, with the highest thermal expansion occurring on the inner surface of the GCC, increasing the rotation of the clamp. Since the temperature difference across the GCC is small, the rotation of the clamp due to this effect is also relatively small. Moreover, due to the temperature difference, there is relative thermal expansion between the clamp and the bolt since both these components have different average temperatures and thereby different average thermal expansions. This relative thermal expansion between the clamp and the bolt is mainly responsible for the increase in the residual bolt preload. The deformation behaviour of the GCC for higher temperature gradients is discussed in Section 5-4.

5.3 Structural and Leakage Integrity of the GCC

This section discusses the stresses generated within the hub, clamp, bolts and the seal-ring under imposed loadings on the GCC, within the context of the allowable stress limits set by ASME (2010c; 2010d). These stresses are presented in terms of the von Mises stresses, commonly used as a failure criterion (ASME, 2010d). The von Mises stresses are calculated based on the principal stresses in three dimensions and therefore are representative of the three-dimensional stress fields.

To investigate the leakage and structural integrity of the GCC, it is loaded as per Cases 1 to 5 in Table 5-1. For Case 1, the primary von Mises stresses generated must remain within the following primary stress limit:

$$\sigma_{p,a} = S_C \quad (6-1)$$

where S_C is the allowable stress of the component material at room temperature (ASME, 2010d). Upon subjecting the GCC to the thermal loadings as per Cases 2 to 5, the secondary von Mises stresses generated must remain within the following secondary stress limit:

$$\sigma_{s,a} = f(1.25S_C + 0.25S_H) \quad (5-2)$$

where f is a stress range factor, and S_H is the allowable stress of the component material at the elevated temperature (ASME, 2008). f is equal to 1.0 for the elevated temperature of 600°C. Table 5-2 lists the allowable stresses for the hub, clamp, seal-ring and bolt materials.

Table 5-2: Allowable stresses for the hub, clamp, seal-ring and the bolt at room temperature and elevated temperature of 600°C.

	Hub	Clamp	Bolt	Seal-ring
S_C (MPa)	138	138	130	255
S_H (MPa)	81	64	65	209
$\sigma_{p,a}$ (MPa)	138	138	130	255
$\sigma_{s,a}$ (MPa)	193	189	179	371

5.3.1 Stress Distribution in the Hub

The effect of thermal loads on the structural integrity of the hub was investigated by subjecting the GCC to external loadings as per Cases 1, 2 and 3 in Table 5-1 to evaluate von Mises stresses in the hub at room temperature, spatially-uniform elevated temperature and spatially-nonuniform elevated temperatures, respectively. The von Mises stress contours for these three cases are plotted in Figure 5-3(a-c). The average von Mises

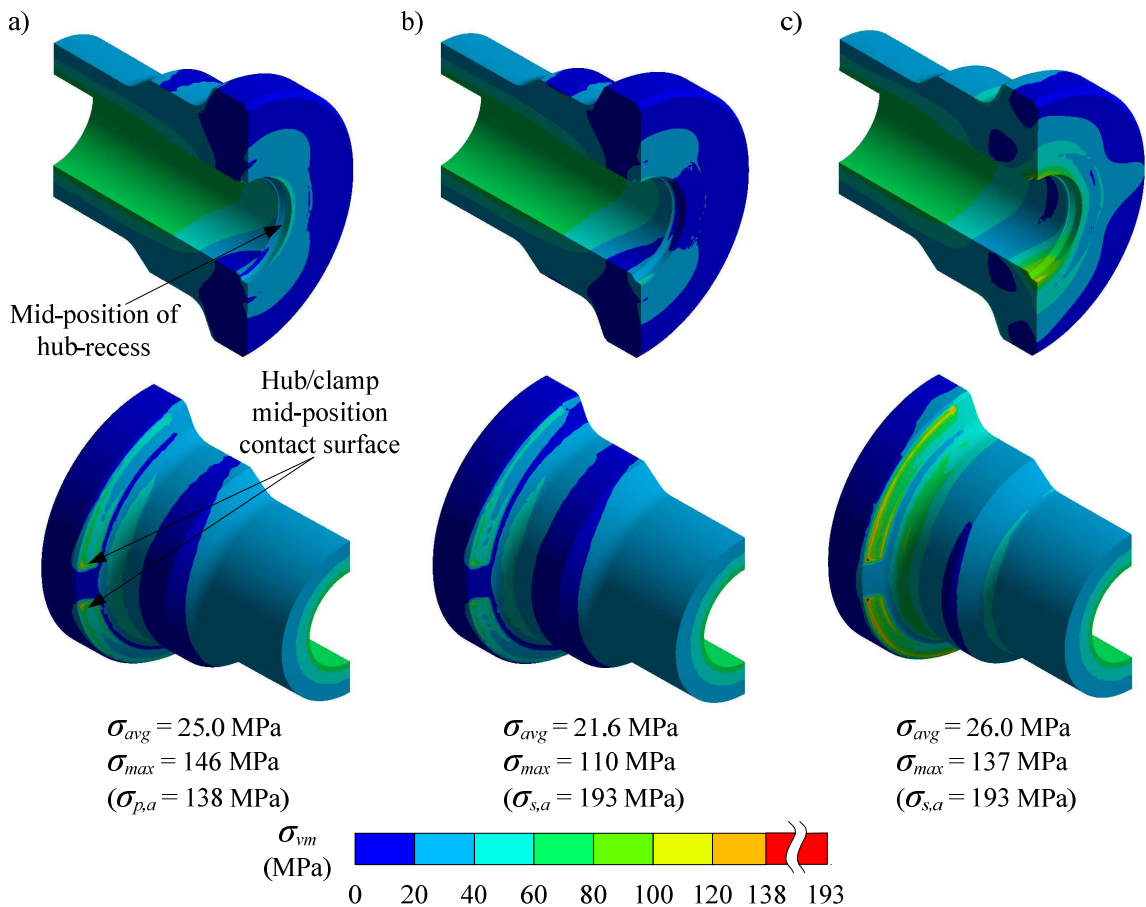


Figure 5-3: Von Mises stresses for the hub a) Case 1—room temperature; b) Case 2—uniform elevated temperature; and c) Case 3—temperature gradients across the GCC at elevated temperature.

stresses in the hub are comfortably within the allowable primary and secondary stress limits for Cases 1, 2 and 3.

As stated in Section 5.3.1, the maximum force applied by the clamp on the hub occurs at the mid-position of the assembly at room temperature. Accordingly, the maximum stresses on the hub occur at the mid-position contact between the hub and the clamp. At room temperature, the stresses are lowest in the hub at the position coinciding with the plane of rotation of the clamp (Figure 5-1) and increase gradually toward the mid-position on the hub that is farthest from the plane of rotation. The corresponding mid-position on the inner surfaces of the seal-ring in contact with the hub also experiences a similar stress distribution (described in Section 5.3.4). As described in Section 5.2, the clamp bends inward toward the mid-position of the assembly due to the bolt preload (Figure 5-1). The contact of the clamp with the outer surface on the hub at this mid-position exerts the maximum force on the mid-position of the hub-recess and thereby on the mid-position of the seal-ring. As discussed in Section 5.2, the clamp rotation is reduced for Case 2. Accordingly, the maximum stresses are reduced, as shown in Figure 5-3b, at the mid-position.

The average and maximum stresses in the hub decrease when the GCC is heated from room temperature to the spatially-uniform elevated temperature, as per Case 2. This reduction is expected due to the pattern of relative thermal expansion of the components yielding a decrease in the residual bolt preload, as described in Section 5-2.

It is interesting to note that with the imposition of a temperature gradient of only 15°C, the average contact stresses on the hub/clamp contact surface increase by 30% from Case

2 to Case 3. The thermal expansion of the hub and clamp are expected to differ despite the fact that they have the same thermal expansion coefficient because the temperature gradient across the GCC results in different temperatures for the clamp and the hub. This behaviour is similar to that noted earlier for the clamp and the bolt where the two components expanded differentially increasing the residual bolt preload. Accordingly, the combined influence of the relative expansion of the hub in the radial and axial directions, relative to the clamp, and the accompanying increase in the residual bolt preload generates these higher stresses at the hub/clamp interface. Moreover, the maximum stresses generated, as illustrated by the red spots in Figure 5-3c, are due to the increase in clamp rotation for Case 3. Despite these thermal influences, the average stresses generated in the hub are low and therefore the hub is deemed structurally safe for operation on the CSCW loop for Cases 1, 2 and 3.

Given that the stresses generated in the components of the GCC are the result of bolt loads, the circumferential stress distribution in the seal-ring would be expected to follow a pattern similar to that of the hub. This will be demonstrated to be the case in Section 5.3.4.

5.3.2 Stress Distribution in the Clamp

The effect of thermal loads on the structural integrity of the clamp was investigated by subjecting the GCC to external loadings as per Cases 1, 2 and 3 in Table 5-1 to evaluate von Mises stresses in the clamp at room temperature, spatially-uniform elevated temperature and spatially-nonuniform elevated temperatures, respectively. The von Mises stress contours for these three cases are plotted in Figure 5-4(a-c). The average von Mises

stresses in the clamp are comfortably within the allowable primary and secondary stress limits for Cases 1, 2 and 3.

The maximum stresses occur at the clamp-neck due to the stress intensification associated with the clamp-neck, by virtue of its geometry (Appendix B). The influence of this stress intensification is seen to propagate up to the location of the bolt hole on the clamp-lug, and over the entire span of the clamp-ring. These maximum stresses exceed the allowable primary stress limits (Figure 5-4a) for the room temperature condition; however, this is

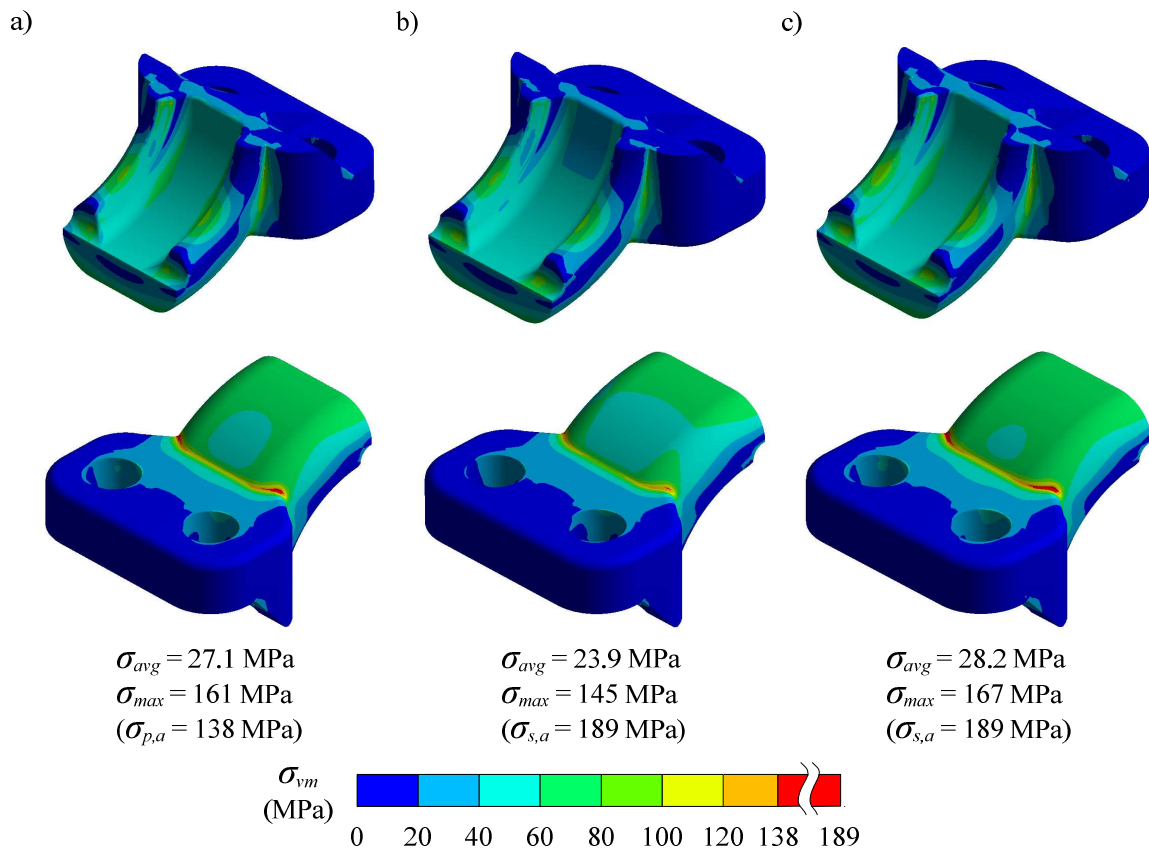


Figure 5-4: Von Mises stresses for the clamp a) Case 1—room temperature; b) Case 2—uniform elevated temperature; and c) Case 3—temperature gradients across the GCC at elevated temperature.

not sufficient to deem the clamp as structurally unsafe. These maximum stresses are restricted only to the surface of the clamp-neck and represent localized surface yielding. For the clamp to fail, this yielding must propagate within the thickness of the clamp-neck. Accordingly, the clamp-neck is considered safe for the external loads based on Cases 1, 2 and 3.

As observed in Figure 5-4a, b and c, high stresses are generated on the outer region of the clamp-ring. The incremental change in the stresses generated on the outer surface of the clamp-ring is similar to the change in the residual bolt preload, when the internal pressure and thermal loads are applied. This reaffirms the argument that the reaction of the GCC components to incremental external loads can be readily anticipated by the reaction of the preload of the bolts to such external load changes. Similar to the hub, the clamp also experiences reduction in stresses when the temperature of the GCC is elevated uniformly, as per the discussion in Section 5.3.1. Similarly, the increase in the stresses in the clamp for spatially-nonuniform elevation of temperature is small, as seen for the hub. Fortunately, these stresses are within the allowable primary and secondary stress limits and therefore the clamp is deemed structurally safe for Cases 1, 2 and 3.

5.3.3 Bolt Stresses

The effect of thermal loads on the structural integrity of the bolts was investigated by subjecting the GCC to external loadings as per Cases 1, 2 and 3 in Table 5-1 to evaluate von Mises stresses in the bolts at room temperature, spatially-uniform elevated temperature and spatially-nonuniform elevated temperatures, respectively. The average von Mises stresses in the bolt for Cases 1, 2 and 3 are 27.1, 23.9 and 27.4 MPa,

respectively, and are comfortably within the allowable primary and secondary stress limits at the design temperature. These low stress magnitudes indicate that the bolt is able to withstand the longitudinal and shear loads that are imposed due to the initial bolt preload and the incremental changes to this preload due to the internal pressure and thermal loading. Accordingly, the bolts are deemed structurally safe for Cases 1, 2 and 3.

5.3.4 Stress Distribution in the Seal-Ring

The leakage integrity of the GCC can be determined by investigating the structural response of the seal-ring to the external loads identified in Table 5-1. The sealing mechanism of the GCC, described in Section 2.2, suggests that the initial bolt preload and the internal pressure applied on the GCC at room temperature are favorable in energizing the seal-ring. Both of these external loads help to deform the seal-ring into the hub-recesses to form an effective seal between the hub and the seal-ring. However, this deformation must remain elastic under load. If plastic deformation occurs, it permanently modifies the geometry of the seal-ring generating a mismatch in the contact surfaces of the seal-ring and the hub-recesses, reducing the leakage integrity of the GCC.

Moreover, the present study also introduces a third external load in the form of spatially-uniform and spatially-nonuniform elevated temperatures. Deformation generated at elevated temperatures due to thermal expansion may significantly add to the room-temperature deformation of the seal-ring. The deformations of the seal-ring are best quantified in terms of the von Mises stresses generated in the seal-ring. For acceptable leakage integrity of the GCC, the von Mises stresses in the seal-ring should remain within the allowable primary and secondary stress limits outlined by ASME (ASME, 2010d).

The von Mises stresses generated in the seal-ring for Cases 1, 2 and 3 in Table 5-1 are plotted in Figure 5-5a, b and c, respectively. The average and maximum stresses in the seal-ring at room temperature are comfortably within the allowable primary stress limit (Figure 5-5a). The circumferential stress distribution in the seal-ring matches the

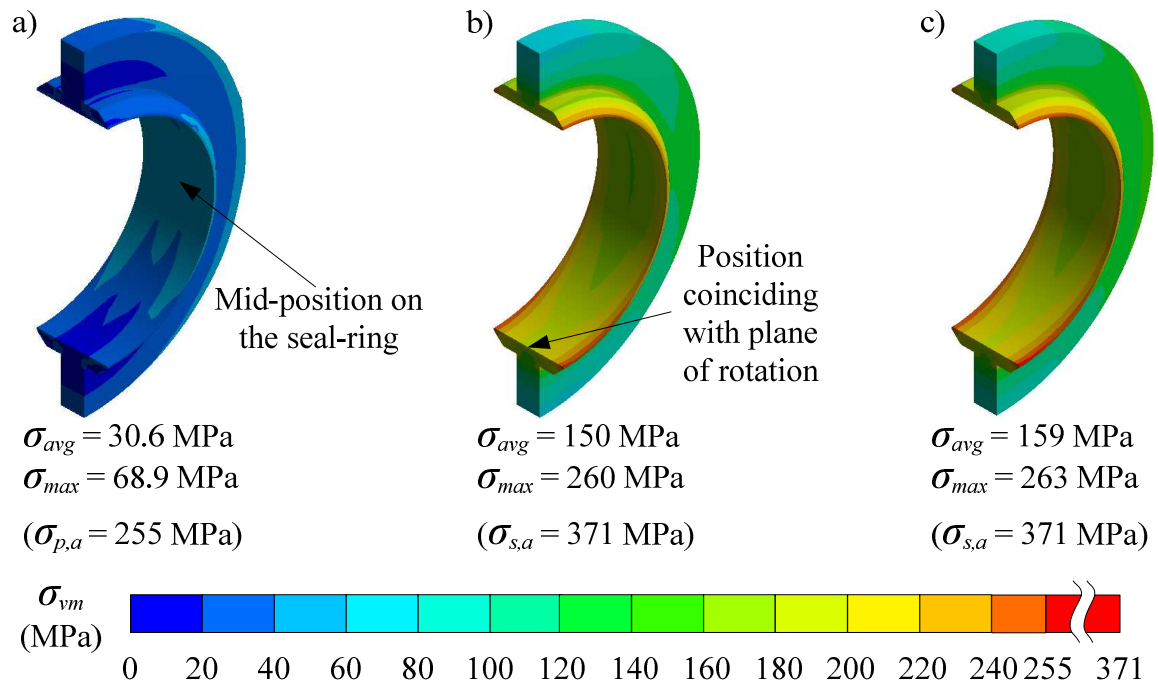


Figure 5-5: Von Mises stresses for the seal-ring a) Case 1—room temperature; b) Case 2—uniform elevated temperature; and c) Case 3—temperature gradients across the GCC at elevated temperature.

circumferential stress distribution observed at the corresponding positions on the hub.

At room temperature, the stresses are lowest in the seal-ring at the position coinciding with the plane of rotation of the clamp (Figure 5-1) and increase gradually toward the mid-position on the seal-ring that is farthest from the plane of rotation. The contact of the

clamp with the outer surface on the hub at this mid-position exerts the maximum force on the mid-position of the hub-recesses and thereby on the mid-position of the seal-ring.

Unlike the reduction in stresses for the hub, the clamp and the bolt, the stresses increase rapidly when the GCC is heated to a spatially-uniform elevated temperature (Figure 5-5b). At room temperature, the residual bolt preload drives the stresses generated in the seal-ring. Since the residual bolt preload decreases for Case 2 due to the relaxation of the hub on the seal-ring, the stresses should decrease in the seal-ring. Therefore, this increase in the stresses in the seal-ring cannot be attributed to the residual bolt preload and thereby the contact load exerted by the hub on the seal-ring. This behaviour of the seal-ring and the hub can be explained by closely inspecting the direction of thermal expansion.

The deformation profile at the cross-section of the seal-ring, as per the loading of Cases 2 and 3 is illustrated in Figure 5-6a and b, respectively. When the internal pressure is applied to the seal-ring at room temperature, the inner-ring is pushed into the hub-recess. The outer-edge of the seal-ring conforms to the shape of the hub-recess. The inner-ring deforms outward at the location coinciding with the outer-ring. The outer-ring is not confined by the hub-recess and therefore slides between the two hub surfaces. The deformation profile is modified when the temperature of the GCC is elevated uniformly, as illustrated in Figure 5-6b. As stated in Section 5.2, relaxation of the hub occurs as the seal-ring expands less relative to the expansion of the hub. Therefore, the load exerted by the hub on the seal-ring (radially within the hub recesses and axially along the outer-ring of the seal-ring) to counter the deformation of the seal-ring under the effect of the internal pressure decreases, thus resulting in the increased stresses in the seal-ring for Case 2. This is indicated by the flipped-curve profile of the deformation of the inner-ring in

contact with the hub-recess. Imposing temperature gradients, as per Case 3, generates a 9

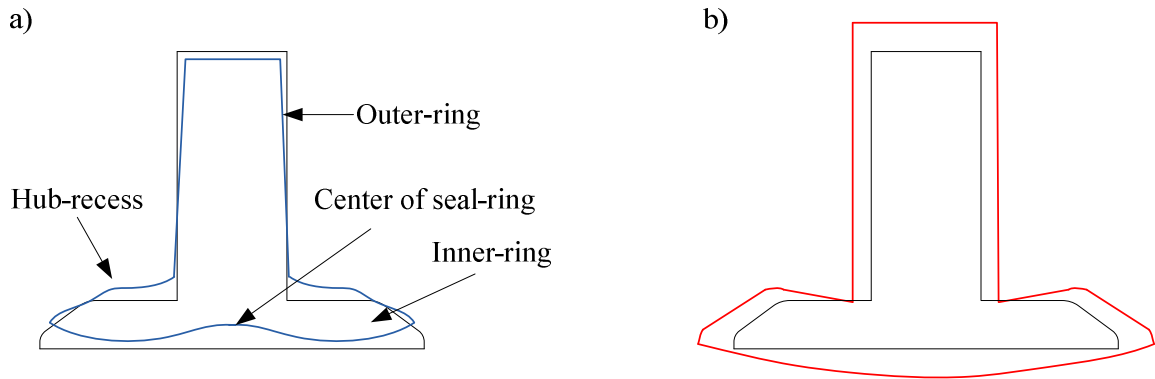


Figure 5-6: Deformation of the seal-ring cross-section for a) Case 1-room temperature; b) Case 2-spatially-uniform elevated temperature. The amount of deformation has been exaggerated 1000 times for clarity.

MPa increase in average stresses compared to Case 2. This increase is due to the increase in the residual bolt preload for Case 3.

Across the axial width of the seal-ring, the highest stresses occur on the tapered-lip of the seal-ring. The sealing mechanism, described in Section 2.2.1.1 suggests that the tapered-lip of the seal-ring is designed to deform to conform to the hub-recesses. The secondary stresses on the tapered-lip are within safe limits for thermal loadings, as per Cases 2 and 3. Nonetheless, there is possibility of localized yielding on the seal-ring since the maximum stresses exceed the value of S_H at the elevated temperature. While the seal-ring is expected to shakedown to elastic behaviour (Appendix B), there may be relaxation of the seal-ring once the GCC is cooled down. It is therefore recommended that the initial bolt preload is checked for proper torque for the first few thermal cycles on the GCC to accommodate any localized yielding. As such, the seal-ring is deemed structurally safe

for Cases 1, 2 and 3. The effect of thermally loading the seal-ring as per Cases 4 and 5 is investigated in Section 5.4.

5.4 Thermal Modelling of the GCC

Preceding sections addressed only one of the thermal models, the fluid-thermal model, developed in Section 3.8. The fluid-thermal model assumed that the bulk-fluid was the only source of heat to the system. It was noted that the components of the GCC were structurally safe for the temperature gradients evaluated from this model. The fluid-thermal model was developed based on certain assumptions. One assumption was that the GCC was employed on the CSCW loop in a controlled environment for a specific mass flow rate of the working fluid. In similar applications, the mass flow rate may vary. Furthermore, the mode of heat transfer from the outer surfaces of the GCC may involve forced convection that may increase the stray heat transfer rate. To account for such changing parameters, the present study was extended to include larger temperature gradients across the GCC. The temperature gradients were gradually increased until leakage or structural failure of the GCC was seen to occur. The initial region of failure on the GCC was observed to be the hub-recess. The von Mises stresses are illustrated in Figure 5-7a and b for Case 3 and Case 4, respectively. The high stresses observed in the hub-recess for Case 3 are amplified in Case 4, as marked by regions with red-coloured contours. The expansion/deformation gradient across the GCC in the radial direction increases due to the higher temperature difference, inducing a greater rotation of the clamp. Furthermore, the relative thermal expansion between the clamp and the bolt increases due to the greater temperature difference across the GCC, increasing the

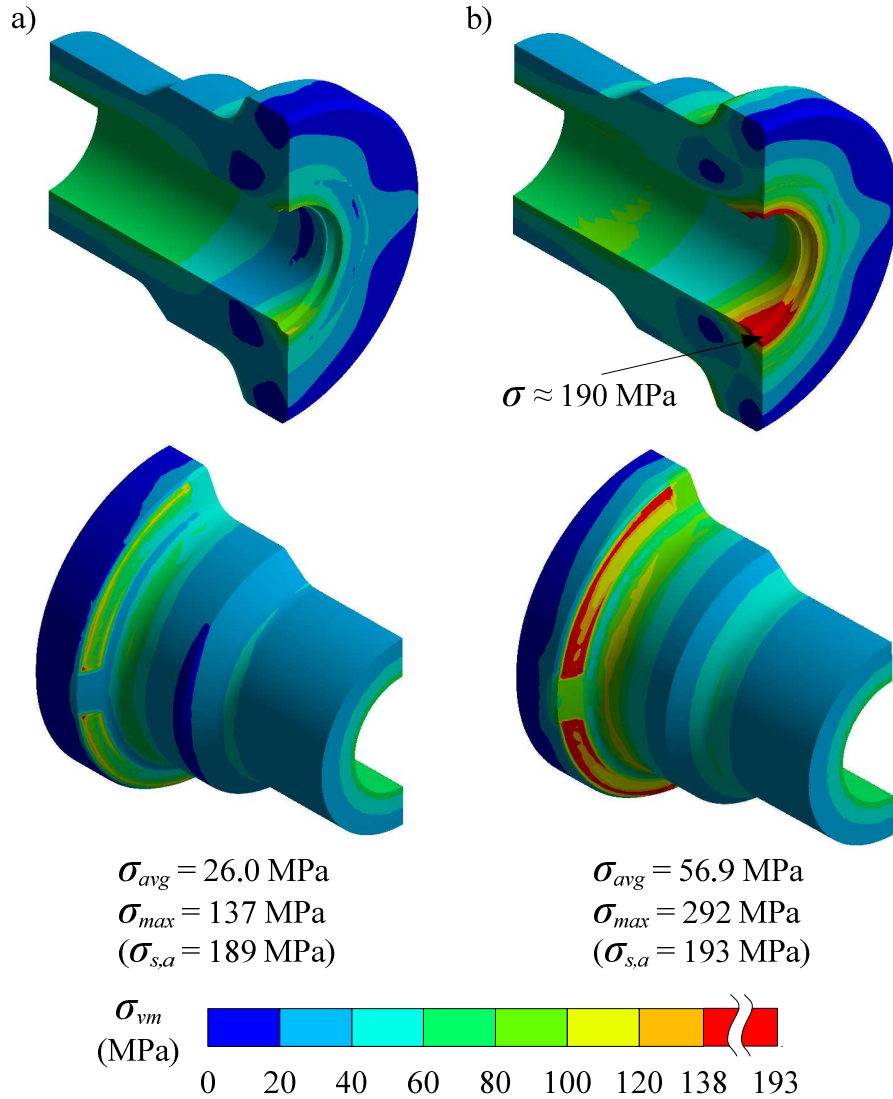


Figure 5-7: Von Mises stresses for the hub for temperature gradients a) Case 3—temperature gradients across the GCC at elevated temperature; b) Case 4—higher temperature gradients.

residual bolt preload by 90%. The increased residual bolt preload generates very high stresses at the hub/clamp interface, as illustrated for the hub in Figure 5-7b. Since the seal-ring is made of a stronger material, it resists the increased contact load exerted by the hub generating very high stresses in the hub-recess. These high stresses reach the allowable secondary stress limit for Case 4.

As per the stresses observed, this deformation almost exceeds the allowable stress limits for the hub, increasing the risk of significant localized yielding between the seal-ring and the hub, thereby reducing the leakage integrity of the GCC. Therefore, it is advised that the use of the GCC be limited for applications where the temperature gradients do not exceed 100°C. If higher temperature gradients exist, thermal insulation must be used to reduce the temperature gradient to acceptable levels.

Due to the close proximity of the GCC to the electrically-heated test section on the CSCW loop, the fluid-thermal model may not be sufficiently precise. In order to include the influence of the test section on the temperature field of the GCC through axial-conduction heat transfer, another thermal model was developed based on the heated-surface of the test section, termed the surface-thermal model, in Section 3.8. The external loadings as per Case 5 in Table 5-1 represent the temperatures evaluated from this surface-thermal model.

It was stated in Section 3.4 that the materials employed in manufacturing the components of the GCC degrade considerably with increasing temperatures. For example, the yield strength of the clamp material degrades by 50% when it is heated from room temperature to the design temperature of 600°C of the CSCW loop. This degradation continues as the temperature is further increased to 1000°C. ASME limits the use of the clamp material to a maximum temperature of 825°C where the allowable stress limit, S_H , for the clamp is 8.8 MPa. Theoretically, using Equation 4-2, the secondary stress limit can be limited to $1.25S_C$. However, engineering analysis of the material suggests that the material is not recommended for use by ASME since it would be highly ductile at such high temperatures, and prone to gross deformations. Gross deformations may cause critical

regions like the hub-recesses and the clamp-neck to lose their dimensional integrity and thereby lend the GCC unsuitable for proper sealing and clamping. Since the test section has to be joined to the rest of the CSCW loop, the GCC may be employed using a stronger material for the components such as Inconel-625, which is used for the test section. However, the seal-ring would interact differently with a harder material and therefore a change of material necessitates a re-design of the clamp connector.

5.5 Friction Sensitivity Analysis

The functionality of the GCC is realized by the transmission of the bolt preload from the clamp-lug to the clamp-ring and from there to the hub and the seal-ring. The effectiveness of the clamping of the hub depends on how the load is transmitted across the contact surfaces of the hub and the clamp. This surface contact can be quantified by the coefficient of friction. The external loads, as per Cases 1 to 5, applied on the GCC in the preceding sections all assumed dry surface contact. This segment of the present study investigates if the effectiveness of the surface contact can be significantly altered by employing lubrication. To simulate lubrication, a coefficient of friction of 0.1 was used to model the contact between the hub and the clamp. The von Mises stresses for the clamp for dry and lubricated contact are illustrated in Figure 5-8(a-b).

As seen in Figure 5-8a, the dry contact surfaces have slightly higher stresses than those for the lubricated contact. The lower stresses for the lubricated contact can be attributed to the greater sliding at the contact interface; greater sliding will reduce the tangential force transmitted between the hub/clamp contact-surfaces, thereby generating lower stresses than those for dry surface contact.

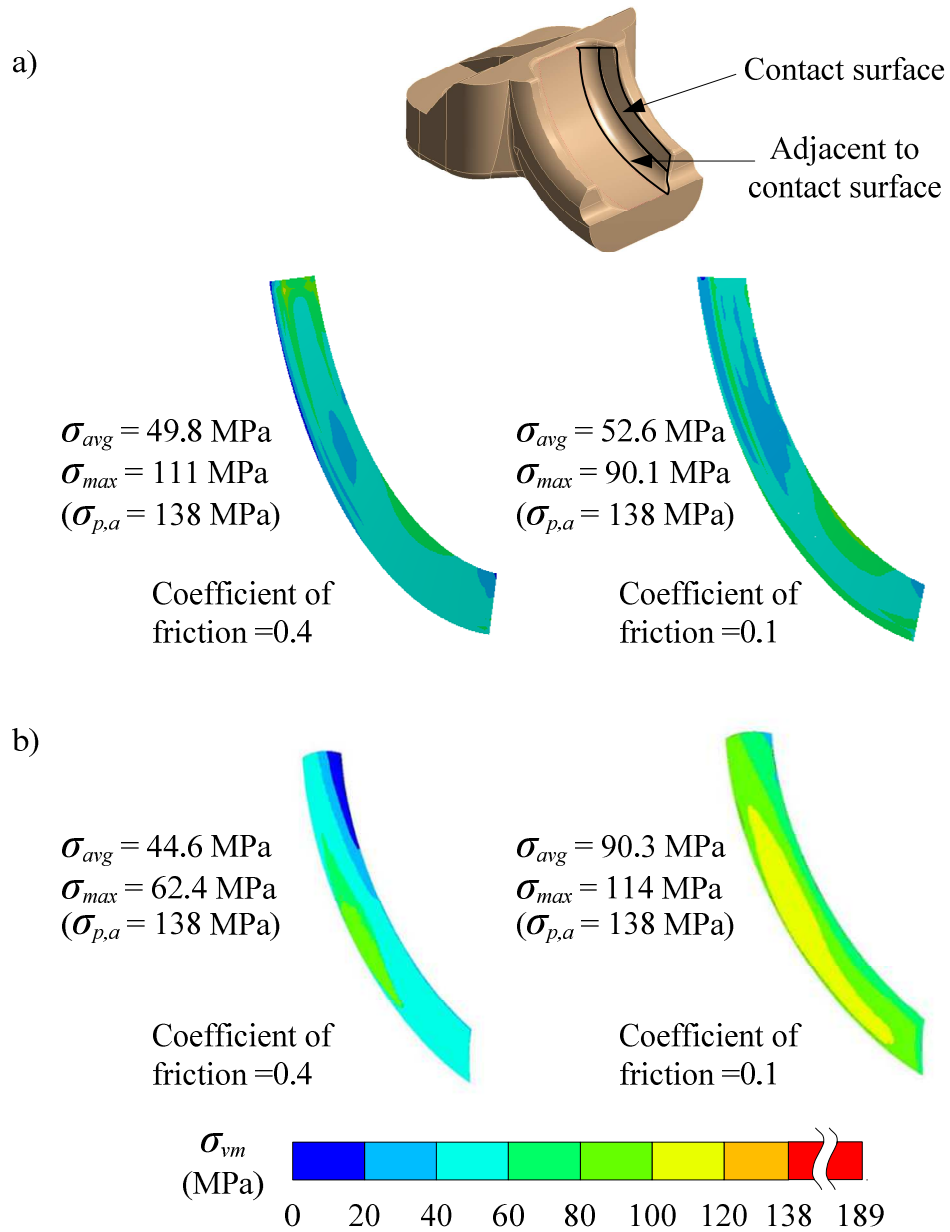


Figure 5-8: Von Mises stresses generated on the a) contact surface; b) surface adjacent to the contact surface

Conversely, as observed in Figure 5-8b, the von Mises stresses are higher in the mouth of the clamp for lubricated contact than for dry contact (Figure 5-8a). The higher stresses are due to increased sliding motion of the hub into the clamp due to lubrication. This

increased sliding stretches the clamp-lips outward generating higher stresses at the base of the clamp.

Since higher stresses exist for lubricated contact between the hub and the clamp, lubrication between the surfaces of the hub and the clamp should not be performed. Hence, a dry contact between the hub and the clamp is preferred for a better grip of the clamp on the hub. In practice, the hub has a polished surface while the clamp has a cast surface. The premise of not polishing the clamp surface during manufacturing is to allow for greater friction at the hub and clamp interface.

Chapter 6: Conclusions

A finite element analysis was performed to investigate the leakage and structural integrity of the bolted flange joint assembly (BFJA) for the design conditions on the low-temperature (260°C) side of the Carleton Supercritical Water (CSCW) loop. Similarly, a finite element analysis was performed to investigate the leakage and structural integrity of the Grayloc[®] clamp connector (GCC) for the design conditions of the high-temperature (600°C) side of the CSCW.

The performance of the BFJA was investigated for the external loads of an initial bolt preload having a magnitude of 55,000 N, an internal pressure of 27 MPa, and spatially-uniform and spatially-nonuniform thermal loadings evaluated for a bulk-fluid temperature of 260°C for the working fluid. The deformation of the BFJA was studied in terms of the rotation of the flange when subjected to these external loads. The modification in the deformation of the flange under spatially-uniform and spatially-nonuniform elevated temperatures was explained. The flange rotational behaviour was used to understand the stresses generated within the gasket. Moreover, the stresses in the gasket were investigated in detail to determine the leakage integrity of the BFJA. The stresses in the gasket were seen to increase when the BFJA was subjected to thermal loadings. It was also determined that the flange and the bolt were structurally safe for the low-temperature (260°C) and pressure (27 MPa) conditions on the CSCW loop.

The performance of the GCC was investigated for the external loads of an initial bolt preload having a magnitude of 6,000 N, an internal pressure of 27 MPa, and spatially-uniform and spatially-nonuniform thermal loadings evaluated for a bulk-fluid

temperature of 600°C for the working fluid and a metal surface temperature of 1043°C. The structural response of the hubs, the clamps, the bolts and the seal-ring was investigated in terms of the von Mises stress distribution. It was determined that the hub, the clamp, and the bolts were structurally safe for the thermal loadings evaluated for the bulk-fluid temperature of 600°C for the working fluid on the CSCW loop. The leakage integrity of the seal-ring was maintained for the same thermal loadings. The GCC can perform safely for temperature gradients that are lower than 100°C. The use of a GCC is not recommended at the exit of the test section of the CSCW loop.

Furthermore, it was determined that lubrication between the hub and the clamp had a detrimental effect on the transmission of load to/from the bolts from/to the clamp. It is recommended that no lubrication be employed between the hub and the clamp surfaces.

References

- Abid *et al.*, M. (2008). Performance of a Flange Joint Using Different Gaskets Under Combined Internal Pressure and Thermal Loading. In X.-T. a. Yan (Ed.), *Advanced Design and Manufacture to Gain a Competitive Edge*. Springer London.
- ANSYS Inc. (2010). ANSYS Mechanical APDL Element Reference.
- Artoos *et al.*, K. (1994). The Measurement of Friction Coefficient down to 1.8K for LHC magnets. *International Cryogenic Engineering Conference ICEC 15*. Genova, Italy.
- ASME. (2008). *ASME Code for Pressure Piping--Power Piping B 31.3*.
- ASME. (2010a). *ASME Boiler and Pressure Vessel Code, Section VIII, Division I*.
- ASME. (2010b). *Design of Clamped Connections; ASME BPVC, Section VIII, Division 1*.
- ASME. (2010c). *ASME Section II-D, Material Properties*.
- ASME. (2010d). *ASME Boiler and Pressure Vessel Code Section VIII Division II*.
- ASME. (2010e). *ASME Code for Pressure Piping B31.1*.
- ASME. (2010f). *ASME PCC-1, Guidelines for Pressure Boundary Bolted Flange Joint Assembly*.

- AutoDesk. (2012). *Gasket Material Properties*. Retrieved from http://download.autodesk.com/us/algos/userguides/mergedProjects/setting_up_the_analysis/nonlinear/materials/Gasket_Material_Properties.htm
- Azih *et al.*, C. (2012). Direct Numerical Simulation of convective heat transfer in a zero-pressure-gradient boundary layer with supercritical water. *Journal of Thermal Science*, 21, 49.
- Balouch, M. N. (2011). Design of Test Loops for Forced Convection Heat Transfer Studies at Supercritical State.
- Beardmore, R. (2012). *ROYMECH*. Retrieved from http://www.roymech.co.uk/Useful_Tables/Screws/Preloading.html
- Becht, C. (2002). *Process Piping: The Complete Guide to ASME B31.3*.
- Bickford, J. H. (2008). *Introduction to the Design and Behavior of Bolted Joints (Non-Gasketed Joints)* (Fourth Edition ed.). CRC Press.
- Bouزيد, A.-H., & Derenne, M. (2002). Analytical Modeling of the Contact Stress with Nonlinear Gaskets. *J Pressure Vessel Technology*, 124, 47-53.
- Bouزيد, A.-H., & Nechache, A. (2005). An Analytical Solution for Evaluation of Gasket Stress Change in Bolted Flange Connections Subjected to High Temperature Loading. *Journal of Pressure Vessel Technology*, 127, 414-422.
- Brown *et al.*, W. (2001a). Determination of Gasket Stress Levels during High Temperature Flange Operation. *ASME Pressure Vessels and Piping Conference* (pp. 185-192). Atlanta, Georgia: ASME.

- Brown *et al.*, W. (2001b). Determination of the Mechanical and Thermal Properties of selected Gasket types. *ASME Pressure Vessels and Piping Conference*, (pp. 35-43).
- Brown *et al.*, W. (2002). Determination of Gasket Stress Levels during Thermal Transients. *ASME Pressure Vessels and Piping Conference*, (pp. 21-28).
- Cengel, Y. A. (2004). *Heat Transfer, A Practical Approach* (Second Edition ed.). Tata McGraw-Hill.
- Dekker, C. J., & Stikvoort, W. J. (2004). Improved Design Rules for Pipe clamp connectors. *International Journals for Pressure Vessels and Piping*, 141-157.
- Do, T. D. (2011). *Effect of Bolt Spacing on the Circumferential Distribution of the Gasket Contact Stress in Bolted Flange Joints*. *Journal of Pressure Vessel Technology*.
- Fukuoka, T. (2005). Finite Element Analysis of the Thermal and Mechanical Behaviours of a Bolted Joint. *Journal of Pressure Vessel Technology*, 127, 402-407.
- Gere, J. M. (1991). *Mechanics of Materials* (Third SI Edition ed.). Chapman & Hall.
- Grayloc. (2010a). Grayloc-Products-Catalog-GLOC-105-12-02-A4-1.
- Grayloc. (2010b). Grayloc Connection Drawing, 1 1/2" GR11, Dwg. No: H800307-949.
- Grayloc. (2012). *Analysis of Grayloc Clamp Connectors In Accordance with ASME Section VIII, Division I*.
- ISG. (2012). *Industrial Seal and Gaskets Ltd*. Retrieved from <http://www.isg.ie/Spiral.html>

- Jenco, J. M., & Hunt, E. S. (2000). Generic issues effecting spiral-wound gasket performance. *International Journal of Pressure Vessels and Piping*, 77, 825-830.
- Krishna *et al.*, M. M. (2007). A study on the sealing performance of bolted flange joints with gaskets using finite element analysis. *International Journal of Pressure Vessels and Piping*, 349-357.
- Lemmon *et al.*, E. (2013). "Thermophysical Properties of Fluid Systems" in NIST Chemistry WebBook. In P. J. Lindstrom, & W. G. Mallard (Eds.), *NIST Chemistry WebBook, NIST Standard Reference Database Number 69*. Gaithersburg, MD: National Institute of Standards and Technology. Retrieved from <http://webbook.nist.gov> (retrieved August 15, 2013)
- Mathan, G., & Prasad, N. S. (2009). Micromechanical modelling and gasket stress evaluation in flange joints under bolt load and internal pressure. *Proceedings of the Institution of Mechanical Engineers, Part E: Journal of Process Mechanical Engineering*, 223, 21-26.
- Nayyar, M. L. (2000). *Piping Handbook* (7th Edition ed.). McGraw Hill.
- OECD, N. E. (2010). *GEN-IV International Forum*. Retrieved from GEN-IV International Forum: www.gen-4.org
- Pioro *et al.*, I. L. (2004). Heat Transfer to supercritical fluids flowing in channels-- empirical correlations (survey). *Nuclear Engineering and Design*.
- PVEng. (2010). *Finite Element Analysis Report-VIII-1 (Tri-Clamp FEA)*.

Ramsdale, R. (2006). *Coefficient of Friction*. Retrieved from Engineer's Handbook:
<http://www.engineershandbook.com/Tables/frictioncoefficients.htm>

Rao, S. S. (2011). *The Finite Element Method in Engineering* (Fifth Edition ed.). Elsevier
Inc.

Sawa *et al.*, T. (1991). A Stress Analysis of Pipe Flange Connections. 494-503.

Shankara *et al.*, A. (2008). Study of solid lubrication with MoS₂ coating in the presence
of additives using ball-on-flat scratch tester. *Sadhana*, 207-220.

Tamarin, Y. (2002). *Atlas of Stress-Strain Curves, 2nd Edition* . ASM International.

Appendix A: Fluid Properties for Water and Air

The fluid properties required for Sections 3.7 and 3.8 are given in this Appendix. Fluid properties for water are given in Table A-1 and Table A-2. Fluid properties for air are given in Table A-3, Table A-4, Table A-5 and Table A-6.

Table A-1: Property data for water at subcritical temperature of 260°C and pressure of 27 MPa (Lemmon, McLinden and Friend, 2013).

Material	Water
Density ρ (kg/m ³)	809.3
Dynamic Viscosity $\mu \times 10^{-3}$ (kg/ms)	0.108
Thermal conductivity k_w (W/m°C)	0.638
Specific Heat c_p (J/kg°C)	4.698

Table A-2: Property data for water at supercritical temperature of 430°C and pressure of 27 MPa (Lemmon *et al.*, 2013).

Material	Water
Density ρ (kg/ m ³)	141.7
Dynamic Viscosity $\mu \times 10^{-6}$ (kg/ms)	2.940
Thermal conductivity k_w (W/m°C)	0.134
Specific Heat c_p (J/kg°C)	7.048

Table A-3: Property data for air at mean film temperature [(125+15)/2] of 70°C under atmospheric pressure (Cengel, 2004).

Material	Air
Thermal Diffusivity $\alpha \times 10^{-5}$ (m ² /s)	2.780
Kinematic Viscosity $\nu \times 10^{-5}$ (m ² /s)	1.995
β (1/°C)	0.003
Thermal conductivity k_a (W/m°C)	0.029

Table A-4: Property data for air at mean film temperature [(245+15)/2] of 130°C under atmospheric pressure (Cengel, 2004).

Material	Air
Thermal Diffusivity $\alpha \times 10^{-5}$ (m²/s)	3.730
Kinematic Viscosity $\nu \times 10^{-5}$ (m²/s)	2.634
β (1/°C)	0.002
Thermal conductivity k_a (W/m°C)	0.029

Table A-5: Property data for air at mean film temperature [(885+15)/2] of 450°C under atmospheric pressure (Cengel, 2004).

Material	Air
Thermal Diffusivity $\alpha \times 10^{-4}$ (m²/s)	1.004
Kinematic Viscosity $\nu \times 10^{-5}$ (m²/s)	6.997
β (1/°C)	0.001
Thermal conductivity k_a (W/m°C)	0.052

Table A-6: Property data for air at Mean Film Temperature [(845+15)/2] of 430°C under atmospheric pressure (Cengel, 2004).

Material	Air
Thermal Diffusivity $\alpha \times 10^{-5}$ (m²/s)	9.604
Kinematic Viscosity $\nu \times 10^{-5}$ (m²/s)	6.686
β (1/°C)	0.001
Thermal conductivity k_a (W/m°C)	0.052

Appendix B: Fundamentals of Stress Analysis

This chapter covers the fundamental theory of stress analysis relevant to the present study. Features of a spiral-wound gasket are briefly explained. Stress categories and structural discontinuities are defined.

B.1 Spiral-Wound Gasket

A spiral-wound gasket shown in Figure B-1 comprises of a core made of metal that is filled or layered with a soft material to reduce the stiffness and allow conformation of the gasket with the surface it is in contact with. The metal provides strength while the non-metal material allows it to conform to the flange surface and provide sealing (Nayyar, 2000).

Spiral-wound gaskets are one of the most commonly used gaskets in the industry (Jenco and Hunt, 2000) and are therefore frequently subjected to numerical modelling. In the construction of a spiral-wound gasket, the core is created by winding a filler material such as graphite on a metal mandrel. This spiral-winding forms the effective gasket, which is enclosed by an inside metal ring to avoid buckling and an outside ring that helps in centering the gasket. The spiral-winding acts like a spring; it flattens under compressive load, and springs back when there is relaxation during operation. As is evident from the cross-section shown in Figure B-1b, the spiral-winding is thicker than the inside and outside rings. Ideally, this additional thickness is the degree to which the gasket can relax under operation. This means the spiral-winding allows for differential expansion of the flanges during operation. The gasket typically has to undergo many

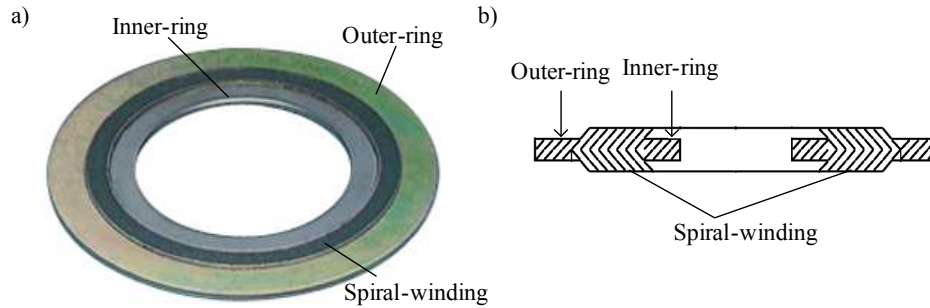


Figure B-1: Spiral-wound gasket a) full view; b) section view (Reproduced from ISG, 2012).

cycles of compression and relaxation during operation (Jenco and Hunt, 2000). However, it has been observed that graphite loses this cyclic ability over time and is unable to regain its original position when relaxed. Inability of the gasket to spring back causes tiny gaps to be created between the gasket and the flange, causing leakage.

B.2 Stress Categories

Stresses are generated by two types of loading; direct loading and indirect loading. Direct loading is when a direct force acts on the BFJA and the GCC such as the initial bolt preload and internal pressure. The stresses generated due to these direct loads can be calculated by dividing the load by the surface area over which it acts. These stresses are referred to as primary stresses or load-controlled stresses because they are evaluated directly from the load (ASME, 2010d; Becht, 2002). Indirect loading on the BFJA and the GCC occurs due to the effect of temperature on the material. Temperature cannot be used directly to calculate stresses; the strain generated due to the temperature gradients across the BFJA and the GCC are used to evaluate the stresses. Therefore, the temperature gradients act as an indirect load on the two assemblies. The product of the

strain and the effective elastic modulus at that location of the strain gives the thermal stresses.

Thermal stresses fall into the category of secondary stresses or strain-controlled stresses because they are evaluated from the strain (ASME, 2010d; Becht, 2002). The secondary stress range is equivalent to the primary stress before yielding of the component since the elastic modulus is identical for both approaches of calculating stress. However, after yielding of the material, the primary stresses are no longer proportional to strain, and therefore cannot be represented by Young's modulus of elasticity. The primary stresses are still calculated directly by dividing the load by the surface area over which it acts. However, for evaluating secondary stresses the elastic modulus is extrapolated up to the strain generated in the material due to the indirect loading. The corresponding stress values at that strain are the secondary stresses. As is evident from Figure B-2, after yielding of the material, the primary and secondary stresses correspond to different strains. Since a higher strain would mean greater distortion of the material, higher primary stresses represent greater chances of failure of the material. Conversely, higher ranges of secondary stresses are allowed since they correspond to lower strain. This explains higher ranges allowed by ASME (2008) for secondary stresses than stress limits for primary stresses. Accordingly, it has been deemed overly-conservative to limit the secondary stresses caused by thermal expansion to the yield strength of the material (Becht, 2002).

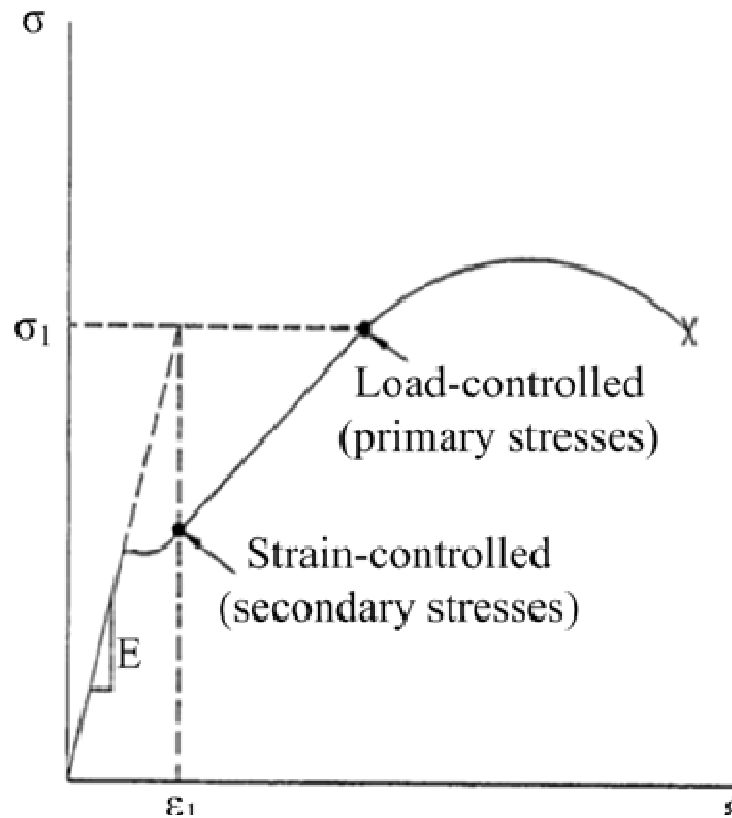


Figure B-2: Load-controlled vs. Strain-controlled behaviour (Reproduced from Becht, 2002).

The concept of elastic shakedown is introduced to allow for a higher secondary stress range. Figure B-3 illustrates the concept of elastic shakedown. Suppose a material is thermally loaded such that the thermal strain developed in the material ϵ_1 , corresponds to a stress value that is equal to twice the yield stress $2\sigma_y$, as shown in Figure B-2. The material would initially develop an elastic strain (A-B) and then yield plastically (B-C). If the thermal load is now removed, the material tries to recover the elastic strain. In order to return to a strain-free state, the material is stressed in the opposite direction to a stress value that is equal to the yield stress of the material (C-E-D). After this initial loading cycle, when the material is subjected again to a thermal load, the material develops a thermal strain following a different path (D-E-C) than the strain-path for the initial loading cycle (A-B-C). In both cases, the end-strain is identical, however, in the second

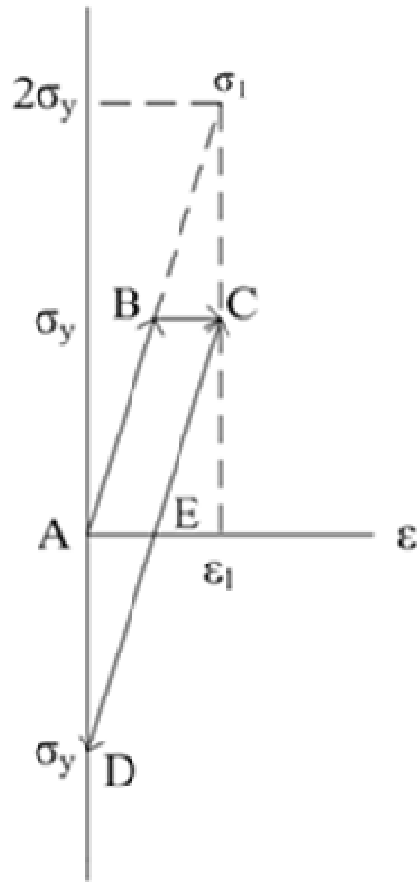


Figure B-3: Stress-strain plot illustrating elastic shakedown behaviour (Reproduced from Becht, 2002).

loading cycle the material does not incur any permanent deformation. The range of ‘elastic’ behaviour of the material is increased. This phenomenon is termed as elastic shakedown. The material can now be subjected to repetitive loading cycles without permanent deformation.

ASME (2008) conservatively limits the elastic shakedown of a material to $1.25\sigma_y$. Therefore, instead of the $2\sigma_y$ limit in the above discussion, the material is allowed to incur plastic strain up to a stress value equal to $1.25\sigma_y$ in the initial cycle. This phenomenon of elastic shakedown, by utilizing the reverse stress in a material allows using a material at higher stress ranges without plastic failure.

Furthermore, secondary stresses are given as allowable secondary stress ranges in design codes (ASME, 2010d) since the material is expected to deform over the range of temperatures, from initial temperature to design temperature. The strength of the material is therefore a function of both the initial temperature and the design temperature.

B.3 Structural Discontinuities

The geometries of the BFJA and the GCC are complex. Since both assemblies consist of geometric junctions, it is important to understand the concept of structural discontinuities. A structural discontinuity can be defined as a region that has intensification of stresses. Local structural discontinuities experience an intensification of stress that is localized in its scope and does not influence the stresses in the rest of the component. For example, as shown in Figure B-4a, a local structural discontinuity is restricted to the weld toe and will intensify the stresses in the weld toe only. Gross structural discontinuities are regions that experience intensification of stresses that can influence the rest of the component and contribute to the overall stress pattern of the component; for example, head-to-shell junctions. For example, as shown in Figure B-4b, a gross structural discontinuity is located at the interface of the head and cylinder, and its influence propagates in the head and the cylinder changing the overall stress pattern.

While the BFJA does not have sharp edges that would exhibit a local structural discontinuity, local structural discontinuities exist at several geometric features on the GCC. Similar to the head-shell junction, the BFJA has a flange-ring to flange-hub junction and the GCC has a clamp-ring to clamp-lug junction. Both the BFJA and the GCC are expected to experience gross structural discontinuities at these junctions.

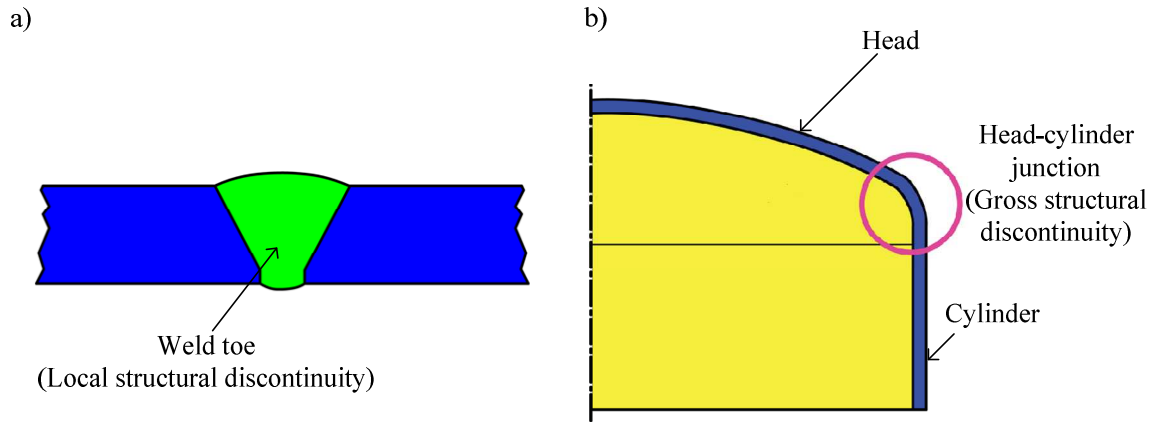


Figure B-4: Structural discontinuities a) local; b) gross (Reproduced from Wood, 2012).